2017

FUNDAMENTAL IMPROVEMENT IN THE TRIBOCHARGING SEPARATION PROCESS FOR UPGRADING COAL

Jinxiang Chen
University of Kentucky, jch282@g.uky.edu
Digital Object Identifier: https://doi.org/10.13023/ETD.2017.397

STUDENT AGREEMENT:

I represent that my thesis or dissertation and abstract are my original work. Proper attribution has been given to all outside sources. I understand that I am solely responsible for obtaining any needed copyright permissions. I have obtained needed written permission statement(s) from the owner(s) of each third-party copyrighted matter to be included in my work, allowing electronic distribution (if such use is not permitted by the fair use doctrine) which will be submitted to UKnowledge as Additional File.

I hereby grant to The University of Kentucky and its agents the irrevocable, non-exclusive, and royalty-free license to archive and make accessible my work in whole or in part in all forms of media, now or hereafter known. I agree that the document mentioned above may be made available immediately for worldwide access unless an embargo applies.

I retain all other ownership rights to the copyright of my work. I also retain the right to use in future works (such as articles or books) all or part of my work. I understand that I am free to register the copyright to my work.

REVIEW, APPROVAL AND ACCEPTANCE

The document mentioned above has been reviewed and accepted by the student's advisor, on behalf of the advisory committee, and by the Director of Graduate Studies (DGS), on behalf of the program; we verify that this is the final, approved version of the student's thesis including all changes required by the advisory committee. The undersigned agree to abide by the statements above.

Jinxiang Chen, Student

Dr. Rick Honaker, Major Professor

Dr. Zach Agioutantis, Director of Graduate Studies

FUNDAMENTAL IMPROVEMENT IN THE TRIBOCHARGING SEPARATION PROCESS FOR UPGRADING COAL

DISSERTATION

A dissertation submitted in partial fulfillment of the

requirement for the degree of Doctor of Philosophy in the

College of Engineering at the University of Kentucky

By

Jinxiang Chen

Hunan, China

Director: Dr. Rick Honaker,

Professor of Mining Engineering

Lexington, Kentucky

2017

ABSTRACT OF DISSERTATION

FUNDAMENTAL IMPROVEMENT IN THE TRIBOCHARGING SEPARATION PROCESS FOR UPGRADING COAL

Triboelectrostatic separation is a physical separation technique that is based on surface electronic property differences among minerals to achieve a separation. Minerals have different surface conductivities and electron affinities. They are charged differently in quantity and/or polarity after a tribocharging process. Particles with different surface charges move discretely under external electric field produce a separation. Electrostatic separation is a dry mineral processing method that does not require any water or chemical reagents. It can greatly simplify the processing circuit and reduce operating cost. Additionally, problems caused by water in conventional wet mineral processing such as water freezing, dewatering, water pollution and water treatment are eliminated. Electrostatic separation has great potential as a fine particle separator (i.e. < 1mm) in industrial minerals processing application, especially in arid areas where water supply is limited.

In the current study, particle tribocharging kinetics was evaluated using a model system comprised of copper, pure coal, silica and ceramic. The results of the tribocharging process were recorded and analyzed using an oscilloscope and a signal processing technique. Charge exchange, charge separation and charge relaxation corresponding to tribocharging processes were studied using the generated pulsing signals. The signals provided a method to quantify the charge penetration into the conductor bulk during tribocharging. A new method to measure the particle surface charge using the pulsing was proposed and assessed, which was extremely useful for subtle surface charge measurements which effectively eliminated environmental noise. The interactive forces at the contacting interface, relative displacement, material electronic properties and ambient relative humidity were found to impact particle surface charge. The silica surface sites are 69 times more chargeable than the coal surface, which provides a fundamental explanation for upgrading that is achievable for silica-rich coal using triboelectrostatic separation. The influences of operating and environmental parameters were quantified and compared using an environment controlled chamber. Energy consumption at the interface was found to be positively correlated with the particle charge. Relative humidity has dual effects on the particle tribocharging, excessively low or high humidity levels do not favor particle tribocharging. Finally, a semi-empirical mathematical model of particle tribocharging was developed from the basic tribocharging compression model utilizing the parametric experiment study results. The model provides a more accurate method to predict particle surface charge under exact tribocharging conditions.

A novel rotary triboelectrostatic separator (RTS) using the tribocharging mechanism was tested for upgrading fine coal. The particle size influencing the RTS tribocharging and separation process is investigated. A practical method to quantify the particle charging distribution was developed based on the direct particle charge measurement and a Gaussian distribution assumption. The smaller particles were found to have a higher average surface charge and wider surface charge distribution, which provided an opportunity to separate the high grade and the low grade coal particles. However, particles that are too small have weak particle-charger tribocharging effect that reduces particle tribocharging efficiency. The particle separation process was analyzed considering the exact experimental hydrodynamic separating conditions. Smaller particles were found to be more sensitive to the airflow that used to transport the particles as a result of the effect on residence time in the separation chamber. A method combining mathematical and statistical analysis was proposed to theoretically predict RTS separation efficiency based on the particle charging conditions and particle separation conditions. The particle horizontal displacement probability distribution was ultimately derived from this method. The model predictions indicate that a wider horizontal displacement distribution provides improved separation efficiency for the RTS unit. The theoretical analysis indicates that a particle size range between 0.105 and 0.21 mm has widest horizontal displacement distribution and thus represents an optimum particle size range which is in agreement with experimental results.

The influences of the RTS operating parameters on separation performance achieved on a pure coal-silica mixture were investigated using a parametric study. The optimum operating conditions were identified. Using the optimum conditions, a five-stage separation process was conducted using the RTS unit to obtain the necessary data for the development of an ideal performance curve. Two stages of RTS separation were found to generate good quality clean coal with acceptable recovery. Particle tribocharging tests were performed using pure coal, pure silica and the coal-silica mixture as model feed materials. The test result found that mixing the pure coal with the sand reduced the particle charge distribution of the coal while increasing the charge distribution of the pure silica particle. The finding explains the inability to produce clean coal products containing ultra-low ash contents. However, the rejection of silica to the tailings stream is very high.

The RTS upgrading of low-ash coal sample was tried using experiment design method, which revealed that feed rate was the most significant while the applied charger voltage and the injection air rate were the least significant in regards to product quality. Feed mass flow rate and the co-flow air rate have a significant interactive effect. Considering the theoretical findings, the impact of high feed rates is due to the negative effect on particle tribocharging efficiency resulting from an increase in the particle-particle surface charge relaxation. Under the optimum test conditions, an ultraclean coal was produced with an ash content of 3.85±0.08% with a combustible recovery of 62.97±1.11% using the RTS unit.

KEYWORDS: Tribocharging, Mathematical Charging Model, Size, Coal, Silica, Rotary Triboelectrostatic Separator

Jinxiang Chen

June 1st, 2017

FUNDAMENTAL IMPROVEMENT IN THE TRIBOCHARGING SEPARATION PROCESS FOR UPGRADING COAL

By

Jinxiang Chen

Dr. Rick Honaker
Director of Dissertation

Dr. Zack Agioutantis
Director of Graduate Studies

July 1st, 2017

To my mother, the epitome of kindness and wisdom,
My father, the epitome of enthusiasm and diligence,
And to those that do their part in making the world a better place.

Acknowledgements

I would like to express my most sincere gratitude to my advisor Dr. Rick Honaker for the role he played in my professional and personal development. I have learned the expertise of mineral processing directly from his fabulous teaching and through the tremendous lab environment and opportunities he facilitated. Moreover, the exploring attitude and initiative spirit he endowed me will no doubt uphold my endless motivation in the challenging future. I would also like to thank my PhD Committee members, Dr. Thomas Novak, Dr. Joseph Sottile, Dr. Dibakar Bhattacharyya, and Dr. Kozo Saito for their invaluable advice and instruction to my research work.

The mining team in our department creates terrific working environment that made much of the research work possible. I appreciate all the staffs and colleagues at the Mineral Processing Laboratory for their tremendous assistance in the past years. Our collaborators endeavored to make meaningful projects happen. I greatly thank such collaborators as CleanCarbon, Illinois Clean Coal Institute, ArcelorMittal and EnvirogenX. It would have been impossible for me to achieve progressive research outcome without their contribution.

Finally, I intend to give my utmost gratefulness to my whole family. Thank my parents for their endless support and encouragement and thank my wife Coco for her limitless love and inspiration. Because of them, I am capable to outstrip every encountered setback and strive to be a better myself.

Table of Contents

List of Tables

List of Figures

Table of Nomenclature

α: probability that charge can transfer between contacting surfaces

a: frictional coefficient

$a_{1,i}$: particle *i* vertical acceleration, m^2/s

$a_{2,i}$: particle *i* horizontal acceleration, m^2/s

Λ: dimensionless value up to 1

A: interface effective contacting area, m^2

A_1, A_2: contacting area of target 1/2, m^2

A_I: actual contacting surface area of the particle *I*, m^2

A_r: contact area of rolling particles on the plane surface, m^2

β: thermal energy, J

b: mean penetration depth, m

C: calculated capacitance of contacting surfaces, F

C_e: capacitance of a capacitor used in test, F

C_s: the capacitance made of two contacting surfaces, F

C_t: capacitance formed by the contacting insulator and metal, F

d: gap distance between contacting surfaces, m

d_l: distance between point *l* and the charge, m

D_p: diameter of the particle, m

D_i: diameter of particle *i*, m

E: electric field strength, V/m

E': Young's modulus, N/m^2

E_c: energy consumption at the interface, J

E_l: centroid of low energy consumption site, J

E_h: centroid of high energy consumption site, J

E_l: electric field strength when penetrates into copper depth *l*, V/m

f_i: interactive force during tribocharging, N

f_n: normal force at the interface, N

f_f: friction force at the interface, N

F_I: normal force at the interface, N

G: boundary conditions related matrix

G_I: gravitational force of particle *I*, N

h_i: relative humidity level, %

k: electrostatic force constant, 9×10^9 N·m^2/C^2

k_1: charging efficiency constant

k_i: particle charging efficiency

k_r: particle charge relaxation efficiency

κ: energy density, J/m^2

l: scree length, m

L: insulator depth, m

L^{-1}: inverse linear operator correlated with the geometry

m: particle mass, kg

N_i, N_j: particle population of material i/j

P_l: potential at point *l*, V

Q_1: charge on copper top surface, C

Q_t: uneutralized charge on the ceramic cylinder, C

Q_2: uneutralized charge in the copper bulk, C

S: Total surface area, m^2

S^1: influence factor for calculation of image charge effect

S_1, S_2: original spherical cap on target 1/2, m^2

S_i: total surface chargeable sites for tribocharging, C/m^2

τ: charging time constant

τ_r: charge relaxation time

u: air velocity, m/s

μ: dynamic viscosity of air, kg/m ·s

$v_{1,i}$: particle *i* falling velocity, m/s

$v_{2,i}$: particle *i* horizontal velocity, m/s

V: total potential difference between surfaces upon separation, V

V': potential difference when it is smaller than Paschen's gaseous breaddown limit, V

V_1: potential difference caused by initial charge on surfaces, V

V_c: interface contact potential, V

V_d: total effective driving force between contacting surfaces, V

V_i: interface imaging potential difference, V

V_{ij}: total effective driving force between surface *i* and surface *j*, V

V_q: potential difference resulted from exchanged charge, V

$V_{q'}$: potential difference caused by neutralized charge in charge relaxation, V

V_s: interface potential difference from surrounding charged particles, V

V_e: interface potential difference from external electric field, V

V_{ic}: potential of two materials in-contact, V

V_{oc}: potential of two materials out-of-contact, V

W: work consumed at the sliding interface, J

$x_{1,i}$: particle *i* vertical displacement, m

$x_{2,i}$: particle *i* horizontal displacement, m

$\emptyset_A, \emptyset_B$: surface work function of A/B, J

ε: dielectric constant in the gap of the contacting surface, F/m

ε_c: copper relative dielectric constant

ε_d: the ambient gas dielectric constant, F/m

ε_r: relative dielectric constant

e: elemental charge, 1.602×10^{-19} C

t_i: total charging time in test *i*, s

q: particle instantaneous surface charge, C

q_1: charge on the bounced particle after collision tribocharging, C

q_i: equilibrium charge can be obtained in test *i*, C

q_s: maximum surface charge quantity, C

η: coefficient affecting the dynamic saturation charge density

R_0: effective resistance in the gap for electron transfer, Ω

R: ceramic cylinder radius, m

R_I: equivalent radius of the particle *I*, m

R_A: contact radius smaller than the particle radius, m

σ: variance of the penetration depth, m^2

σ_0: charge density at the beginning of contact charge, C/m^2

σ_a: surface sites available for charge exchange, C/m^2

σ_c: compressive strength at the center of contact area, N/m^2

σ_e: equilibrium charge density, C/m^2

σ_s: maximum surface charge density, C/m^2

σ_i: initial accumulated charge density on the surface, C/m^2

σ_i^1: image charge density distribution on the plane, C/m^2

σ_m: Maximum saturation charge density obtainable on the surface, C/m^2

σ_u: upper limit of the compressive strength, N/m^2

σ_I: compressive strength of the particle, N/m^2

u_1: area influenced by the particle charge and image charge, m^2

δ_0: overlap in the collision, m^2

δ_o^u: unrecoverable plastic overlap at the interface, m^2

p_D: Probability that a position on the surface can lose electron

θ: inclining angle, °

ρ: surface position density can accept or lose electrons, C/m^2

ρ_i: particle *i* surface site density, C/m^2

ρ_A: surface sates density of sites accepting electron, C/m^2

ρ_D: surface states density of sites losing electron, C/m^2

z: average contacting surfaces distance, m

z_c: critical gap including the surface roughness, m^2

1. Background

Recognition of the tribocharging effect was first recorded in the 16th century by observation of a charge that was created after rubbing together the surfaces of two insulators. This phenomenon is known as the tribocharging. Triboelectrostatic separation is a physical separation method that is based on the tribocharging mechanism. Particles made of different materials have different surface compositions (element composition, chemical functional groups, lattice structure etc.) which are related to their surface electric properties. Those particles with dissimilar electric property will be charged differently through tribocharging. Tribocharging is a complex physical phenomenon that related to the material surface properties, particle size and shape, moisture content, ambient atmospheric condition and the types of comparative motion.

Triboelectric separation has been wildly studied and applied in the lab scale and the industry such as plastic waste recycling (Inculet et al., 1998), coal beneficiation (Dwari and Rao, 2007), phosphate beneficiation (Bada et al., 2013), fly ash purification (Soong, 2001), ilmenite (Trigwell et al., 2009), mica (Iuga et al., 2004) and other minerals. However, the mechanism of tribocharging has not reached a consensus. Since tribocharging among different types of materials are supposed to have different types of charge carriers responsible for the charge exchange, no tribocharging mechanism proposed to date can thoroughly explain all observed physical phenomenon.

Three tribocharging mechanisms are most commonly accepted to explain the tribocharging phenomenon, i.e.,: (1) electron transfer mechanism, (2) ion transfer mechanism and (3) material transfer mechanism. Electron transfer is generally used to explain the charge exchange between two conductors. A work function difference is the driving force for the electron transfer between two contacting conductor surfaces. The surface with higher work function value will be negatively charged while the surface with lower work function will be positively charged after the contact charging between them (Sternovsky et al., 2002). The work functions of many materials and their relative positions in the triboelectric series have been reported (Shaw, 1917; Davies, 1969). Ion and material transfer are usually used to explain the charge transfer when insulator is involved in the tribocharging process (Lungu, 2004; McCarty et al., 2007; Shinbrot et al., 2008; Pham et al., 2011; Baytekin et al., 2012). Material transfer has been used to explain the charge transfer between insulators which involves the transfer from one surface to another surface acting as the charge carrier. The breakage of the material structure is the source of charge (Kiely and Hsia, 2002; Baytekin et al., 2012). However, some tribocharging phenomenon still cannot be well explained by the existing mechanisms such as the material bipolar charging of identical material (Reischl et al., 1996; Zhao et al., 2003; Forward et al., 2009), which was found to be more closely related to the particle size rather than the particle surface property. Since there are so many factors (including the particle physical property, particle motion, and particle surface characteristics) that have been reported to affect the particle tribocharging process, the tribocharging mechanism needs more in-depth study to have a comprehensive understanding of the tribocharging and assist the electrostatic separation.

In addition to the particle charging process, the particle final charge is also controlled by the discharge process. When the charges exceed a certain level during contact charging, the discharge process might occur when these surfaces are separated (Matsuyama and Hideo, 1995; Shinjo et al., 1999; Shinbrot et al., 2008). The existence of discharge makes the particle final charge quantity more difficult to predict. Thus both the particle charging process and the discharge process need to be considered for analyzing the final particle charge.

1.1. Condenser model of tribocharging process (electron transfer mechanism)

In the condenser model, electrons are the charge carrier during the tribocharging process. Tribocharging occurs between two surfaces when they are contacted. The charges are more easily exchanged between these two surfaces if their Fermi levels difference is large. Fermi level is an index for the average energy of electrons on the material surface as shown in Figure 1.1. Work function represents the energy required to move the electron out of the material surface to become a free electron. If the material has lower Fermi level (or has higher work function), it is easier to accept electrons from the outside source (the other surface), which is also named the p-type material (with higher electron affinity). In contrast, the material that has a higher Fermi level (or has lower work function) is an n-type material (with lower electron affinity) and is easier to lose electrons (Dwari and Rao, 2006; Ciccu et al., 1993).

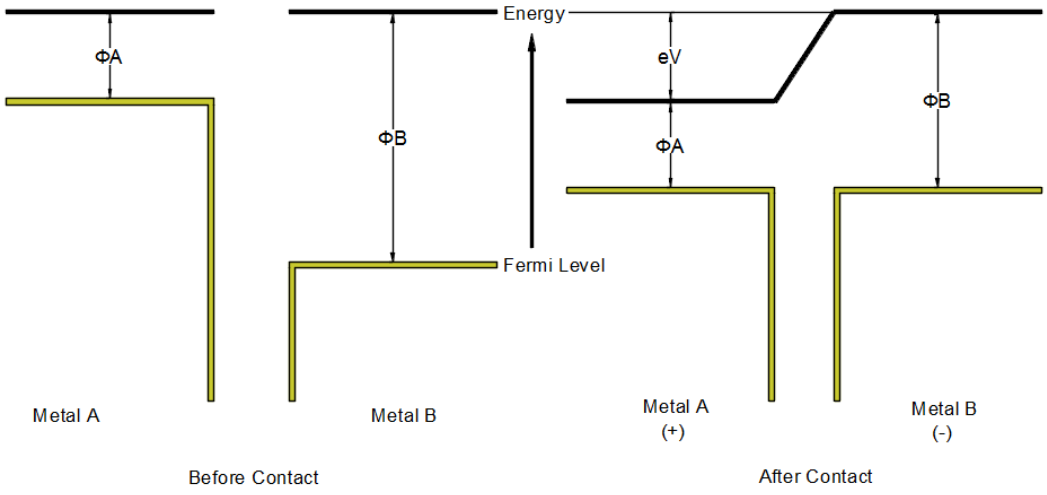

Figure 1.1. Contact potential difference of metal-metal contact and electron potential energy (Matsusaka et al., 2010).

The two surfaces involved in tribocharging can be treated as the two plates of a capacitor. With the compression of the two surfaces, the charge transfer proceeds. The exchanged charge will generate a static electric field between the two contacting surfaces that counteracts with the driving force (Fermi level difference reduces). When charge exchanged between the two surfaces reaches the threshold that the Fermi levels of the contacting surfaces are equal, the charges transfer process stops (the exchanged charges generally do not reach the threshold in one single contact). The model that describes the electron transfer process between the two contacting surfaces is known as the condenser model (Masuda and Koichi, 1978; Matsusaka et al., 2010; Pei et al., 2013; Bunchatheeravate et al., 2013). If the two surfaces have an initial surface charge before contact, the initial charge will affect the charge transfer process. The initial charge can hinder or accelerate the charge transfer efficiency depending on whether or not the electric field generated by the initial charge is identical or opposite relative to the electron transfer direction. When the two surfaces are separated after tribocharging, the transferred charges retained on the surfaces are the static charges. The condenser model describing the electron transfer process is shown in Figure 1.2.

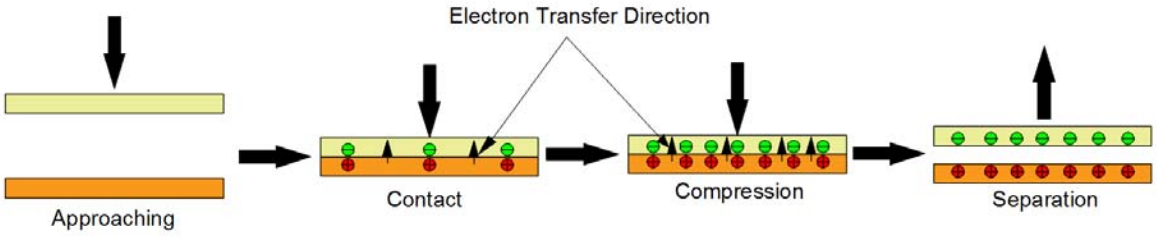

Figure 1.2. Schematic diagram of the condenser model for tribocharging.

The driving force for the electron transfer between two contacting surfaces originates from the Fermi level difference, which is known as contact potential, V_c. The contact potential can be quantified according to the following expression:

$$V_c = \frac{\emptyset_A - \emptyset_B}{e} \quad (1)$$

where e is the elementary charge and $\emptyset_A$ and $\emptyset_B$ are the work functions of contacting surface A and B, Work functions are normally used to quantify the contact potential (Matsusyama and Yamamoto, 2006; Matsusaka, 2011).

The electric field is typically provided by an outside source, which generally counteracts with the driving force for the electron transfer. The total driving force for the electron transfer is described by:

$$V_d = V_c - V_i - V_s - V_e \quad (2)$$

where the V_d is the exact potential difference providing the driving force for electron transfer, V_i the imaging potential difference, Vs the potential difference from surrounding charged particles, and V_e is the potential difference from the external electric field.

Since the contacting surfaces can be treated as two parallel capacitor plates, the effective contacting area determines the capacitance. The capacitance, C_s, of the two surfaces with effective contacting surface area (A) is given as:

$$C_s = \frac{\varepsilon A}{4\pi k d} \quad (3)$$

where d is the gap distance between the surfaces, ε is the dielectric constant inside the gap, k the electrostatic force constant (9×10^9 N·m^2/C^2).

Therefore, based on the condenser model, the maximum charge quantity q_s and the maximum surface charge density σ_s resulting from the work function difference that can accumulate on the surface are:

$$q_s = k_1 C_s V_d \quad (4)$$

$$\sigma_s = \frac{q_s}{S} \quad (5)$$

where k_1 is the charging efficiency, which is related to the resistance to the charge transfer, and S the total surface area (m^2). Because the electron transfers from one surface to the other, the gap between the two surfaces resists the electron transfer with effective resistance R_0. The schematic

diagram of the simulated electric circuit for contact charging is illustrated in Figure 1.3 (Ireland 2010).

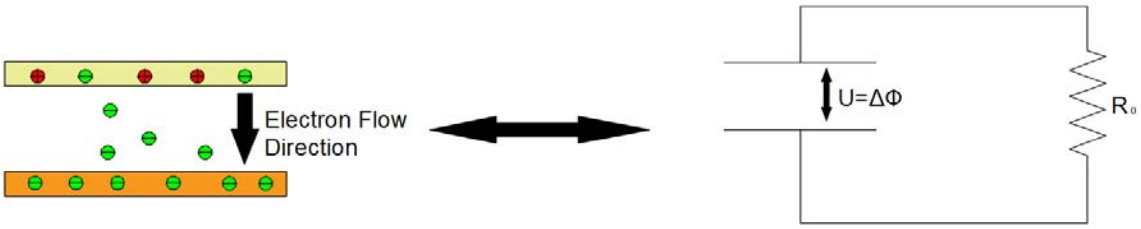

Figure 1.3. Schematic electric circuit of contact charging.

Therefore, considering the charge efficiency of the tribocharging process and the resistance of the simulated tribocharging circuit, the charge transferred to the surface for each collision can be calculated as (Zhou et al., 2013):

$$\frac{dq}{dn} = k_1 V_d - R_0 V_1 \sigma_i \tag{6}$$

where the V_1 is the potential difference caused by the initial charge on the surfaces.

After the separation of two surfaces, the exchanged charge retains on the surface. It affects the tribocharging efficiency as the initial charge on the surface in the contact charging. This initial charge generates an electric field around the solid surface hinders the charge transfer upon subsequent contacts. The charge transfers onto the surface with initial charge after each impaction is (Ireland 2010):

$$\frac{dq}{dt_i} = \frac{A}{R_0 C_s}(\sigma_m - \sigma_i) \tag{7}$$

in which σ_m is the maximum saturation charge density that can be retained on the surface, σ_i the initial accumulated charge density on the surface, and t_i is the effective contact charging time.

When the charge transfer is in the particle-surface contact, the saturation charge depends on the particle diameter and the relative dielectric constant of the gas media (Cangialosi et al., 2006). The expression for the charge transferred onto the particle in each collision can be expressed as:

$$\Delta q = \frac{\varepsilon_r \varepsilon_d A}{d}\left(V_d - \frac{2d}{\pi \varepsilon_r \varepsilon_d D_p^2} q_i\right) \tag{8}$$

where q_i is the initial charge, ε_d the ambient gas dielectric constant, ε_r the relative dielectric constant, D_p (m) is the diameter of the particle.

After every collision, the transferred charges remain on the surface. The retained charges shift the Fermi levels to the balance value of the contacting two surfaces. The charge transfer ceases when the Fermi levels of contacting surfaces are equal. The charge per unit area in this situation is the saturation charge density of the surface.

1.2. Ion transfer mechanism of tribocharging process

In the ion transfer mechanism, the charge carrier during tribocharging is the ion. This model is usually preferred when the insulator is involved in the tribocharging process. The ions are considered to exist in the surface region. The contacting surfaces will reach equilibrium status

through the interaction between ion and surface molecules. The relative stability of the ions on either of the contacting surfaces determines the ion transfer direction. The surface electric property of a material could be altered if there are external ions adhered on it (Diaz and Fenzel-Alexander, 1993). The ion transfer between contacting surfaces was observed directly by Mizes and other researchers in 1990. Bromine ions were found on an indium surface after the contact charging between doped polystyrene and indium (Figure 1.4) and the number of bromine ion was much more than five times the cetylpyridinium ion. The finding shows that bromine ions were found to transfer more from the polystyrene surface to the indium surface, which was considered to be the charge carrier that responsible for part of the transferred charge during the contact charging.

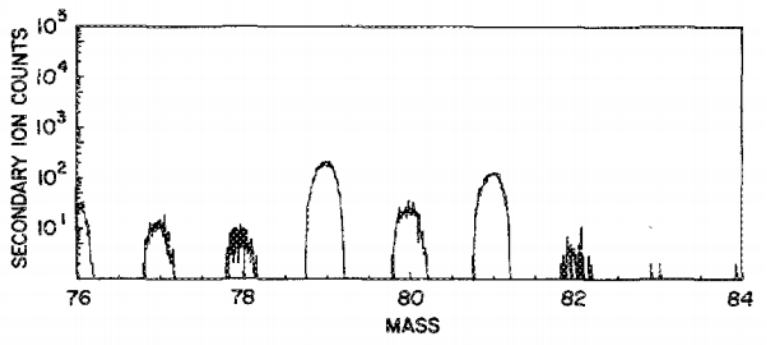

Figure 1.4. Secondary-ion counts ranging from mass 76 to mass 84. Mass 76 and 81 correspond to the atomic weight of the isotopes of bromide (Mizes et al., 1990).

The ion transfer between polymer and polymer (toner) was observed and the transferred ions are distributed uniformly on the particle surface (Law et al., 1995). The cetylpyridinium ion was transferred from the toner surface to the polymer bead surface during contact charging while the corresponding $tBST^-$ ions were not found on the polymer bead surface as shown in Figure 1.5. The results show the preference of Cs+ transfer from toner surface to the polymer surface. The cetylpyridinium ion concentration on the polymer surface correlates well with its charge density after the tribocharging process as shown in Figure 1.6. Therefore, the researchers proposed that the ion should be the dominant charge carrier in the tribocharging process.

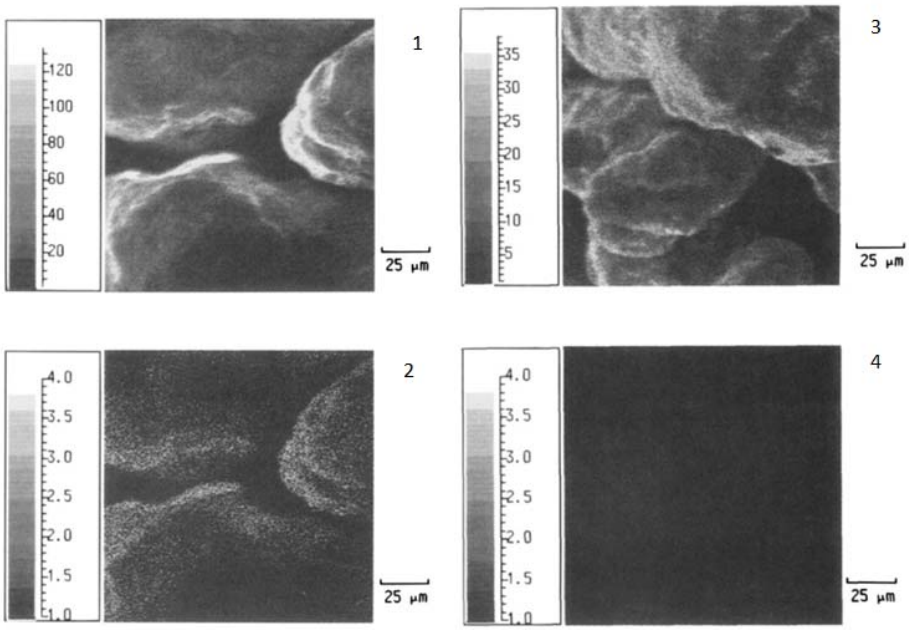

Figure 1.5. Time-of-flight secondary ion mass spectrometer image of polymer beads after tribocharging: (1) total cations; (2) cetylpyridinium ion; (3) total anions; (b) corresponding $tBSA^-$ ions of Cs^+ (Law et al., 1995).

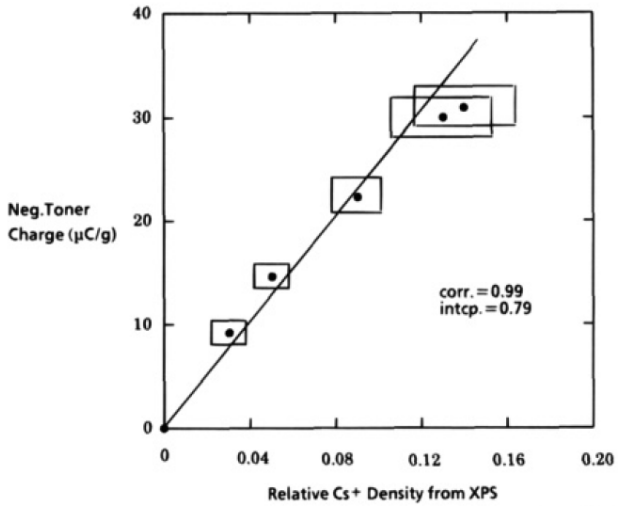

Figure 1.6. Negative charge density versus the relative cetylpyridinium ion density on the surface of polymer beads (Law et al., 1995).

1.3. Material transfer mechanism of tribocharging process

In the material transfer mechanism, patches of material transfer from one surface to another surface. The patches (from nanometers to micrometers) are considered to be charged because the bonds are broken during the material transfer, which contributes to the charge transfer through tribocharging (Lacks and Sankaran, 2011). The relative softness of contacting material

determines the direction of material transfer. In 2012, Baytekin and his research group studied the tribocharging between different polymers. They reported that during the contact charging between polystyrene (PS) and polytetrafluoroethylene (PTFE), the PTFE material deposited on the PS surface (Figure 1.7) which resulted in a negative charge of on the PS surface. In addition, little amount of PS material transferred to the PTFE material due to its positive charge. The charge distribution on the surface is not homogeneous, as indicated by the detected charge localized on the surface. As the time of contact charging process increases, the transferred materials between PS and PTFE improved which resulted in a larger charge transfer quantity. Charge polarity of the materials could change if the tribocharging time is longer than the critical time that the material transfer direction is reversed (Figure 1.8). These characteristics indicate tribocharging between many polymers (PTFE, PS, polymethyl methacrylate (PMMA), polyvinyl chloride (PVC), Cellulose acetate and Nylon) and provide evidence that material transfer was the source of charge transfer. Since deposited patches of materials on one surface after contact charging is inhomogeneous, the most persuasive proof that the transferred material acts as the charge carrier is the inhomogeneous distribution of charges on the surface that correspond to the transferred material patches. The charge distribution on the material surface is mosaic like pieces put together after the tribocharging between two polymers which has been directly observed. The charge might be caused by the transferred material patched on the surface (Baytekin et al., 2011). In their experiment, tribocharging between the polydimethylsiloxane (PDMS) and PTEF was conducted. The surface charge map was imaged by confocal roman microscopy when the PDMS was neutral, positively charged and negatively charged as shown in Figure 1.9. The high resolution x-ray photoelectron spectroscopy (XPS) spectra of the PDMS surface were employed to monitor the surface chemical modification after tribocharging. The material transfer between PDMS and PTFE after tribocharging was proved by XPS spectra of their surfaces. F 1s peak found on the PDMS surface indicates the transfer of PTEF, while Si 2p and O 1s peaks detected of the PTEF surface shows some PDMS patches. The material transfer is believed to correspond with the charge transfer.

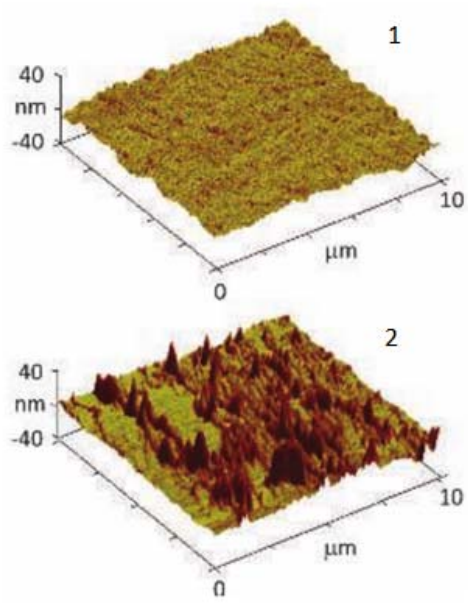

Figure 1.7. Atomic force microscopy (AFM) 3D topography from height maps shows the deposit of PTFE on the PS surface before (1) and after (2) contact charging (Baytekin et al., 2012).

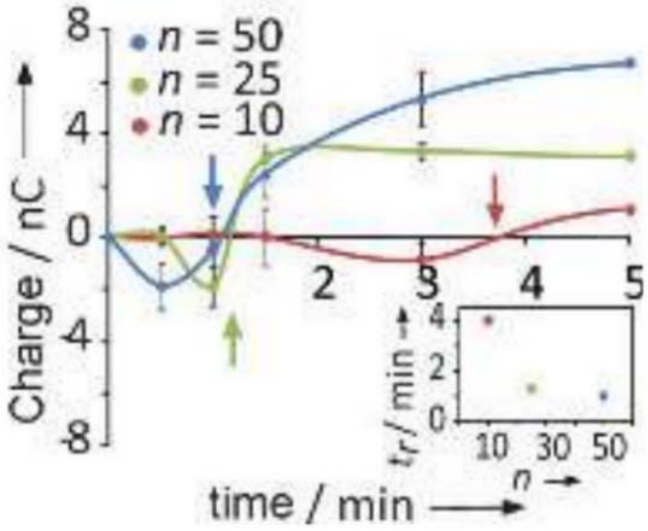

Figure 1.8. The total charge on PTFE beads after the tribocharging between the PTFE and the PS with specific time using different number of beads (n) (Baytekin et al., 2012).

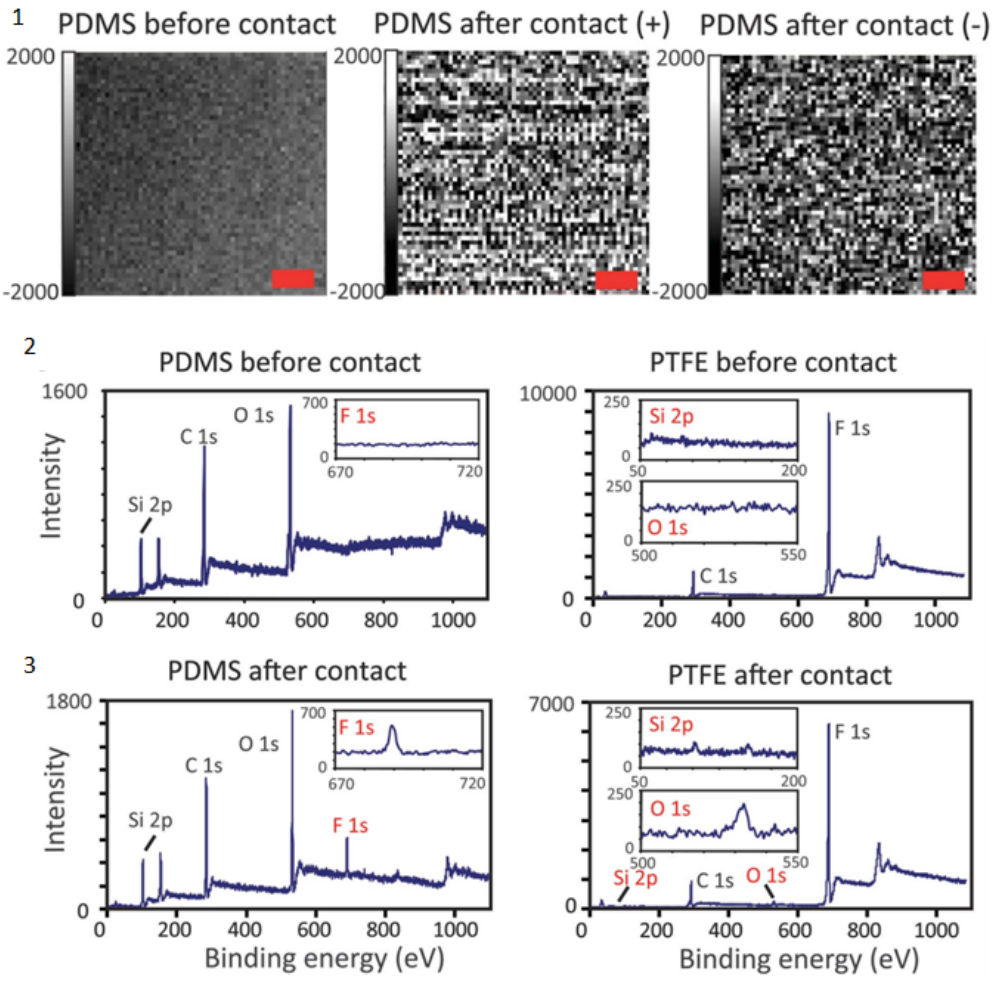

Figure 1.9. (1) Mosaic distribution of charge on PDMS surface shown by Confocal Raman Microscopy image of uncharged, positive charged and negative charged PDMS (scale bar is 2 µm). (2) High-resolution XPS spectra of PDMS and PTFE surface chemical composition before contact charging. (3) High-resolution XPS spectra of PDMS and PTFE surface chemical composition after contact charging. On PDMS surface, F 1s peak indicates the PTFE transferred onto PDMS. On PTFE surface, Si 2p and O 1s peaks indicate the PDMS transferred onto PTFE (Baytekin et al., 2011).

1.4. Charge relaxation

When contact surfaces are brought into contact, a charge is retained after tribocharging. When the surfaces are initially separated from each other after the collision, gas fills the gap between them. Based on the condenser model, the capacitance made of the two surfaces reduces with the increasing gap distance. Since the quantity of the charges residing on the surfaces is constant, the potential difference between these two surfaces rises rapidly with the increasing gap. (Matsuyama and Yamamoto 1995). Finally the potential difference between the separating surfaces initiates the gaseous breakdown when it exceeds the limit of the ambient atmosphere. The well-known Paschen's curve describes the relationship between the gap distance and the potential breakdown threshold between surfaces as shown in Figure 1.10.

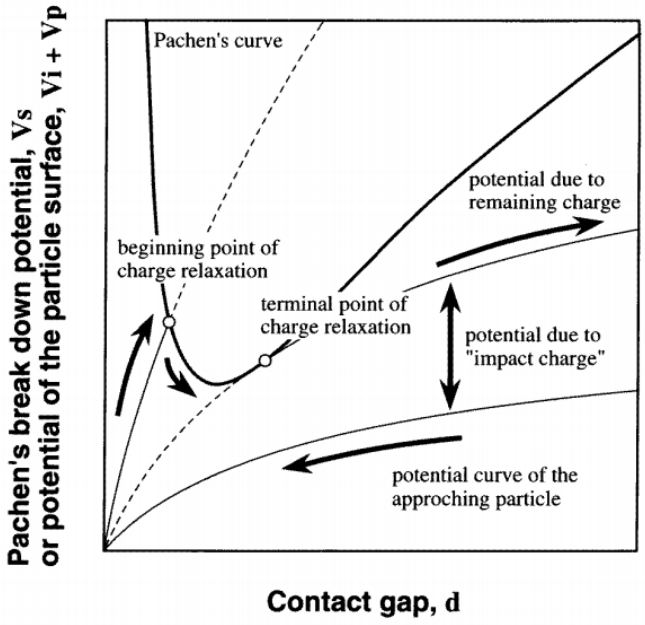

Figure 1.10. Paschen's law describing the relationship between gaseous potential break down limit and gap distance (Matsuyama and Yamamoto 1997).

The potential difference caused by the charge before contact charging is V_1. The charge exchange through contact charging between the surfaces results in the potential difference of V_q. The total potential difference between the surfaces upon separation is:

$$V = V_1 + V_q \tag{9}$$

Since the gaseous breakdown potential limit is a function of the gap distance $V(d)$. When V>V(d), the charge relaxation occurs between the surfaces. The remaining charge quantity after the charge relaxation reduces to q'. The total potential difference reduces to V' when the value is smaller than the Paschen's gaseous breakdown limit:

$$V' = V_1 + V_{q'} \tag{10}$$

Kusano (2009) observed the plasma generated in the experiment during tribocharging to explain the breakdown voltage associated with the gap distance shown in the Paschen's curve. If the gap distance is short enough, the combined space charge field causes the cathode to emit electrons that generate the plasma in the small gap which ignites the gas breakdown. Therefore, the breakdown voltage decreases with the reducing gap. However, if the gap distance is too small, the collision of the charge sharply suppresses the electron emission efficiency that increases the charge breakdown voltage. Thus, there exists a minimum voltage requirement for the discharge.

Peterson (1954) described that the influence of atmospheric pressure on the charge breakdown process. When the atmospheric pressure rises above vacuum, the charge accumulated on the particle surface will have higher than the average charge density that initiated the discharge. There exists an atmospheric pressure value that allows minimum charge on the particle to initiate the discharge. When the pressure exceeds the value, the charging rate becomes smaller. The charge distribution is more homogeneous, exchanged charges better spread into the vicinity, that only has localized discharge (discharged charge quantity is low). Thus the total charge

accumulated on the particle surface depends on the gaseous discharge which is related to the atmospheric pressure.

Put the gaseous breakdown phenomenon aside, there exists another charge decay phenomenon which is caused by the slow discharge. If the charge decay time is less than 0.1s, the discharge is classified as abrupt which is typically a result of gaseous breakdown (occurs in highly charged regions). If the charge decay time is more than 0.4s, this discharge is classified as the slow discharge normally caused by charge diffusion and neutralization (occurs in charge increasing regions). (Singh et al., 2012).

Since charge relaxation exists during the separation of the surfaces, the final maximum surface charge density is not only determined by their Fermi level difference, but also controlled by the charge relaxation.

1.5. Effect of image charge

When a particle impacts a surface and then bounces back to the space, the particle is charged and left the image charge with same quantity on the surface. The image charge dispersed to surrounding area after the particle bounced back and there is electric field generated between the charge on particle and the image charge. With the delocalization of the image charge on the surface, the influence of the electric field may impact the tribocharging of other particles. The schematic diagram of the bounced charged particles and their influence on the tribocharging of other particles is illustrated in Figure 1.11.

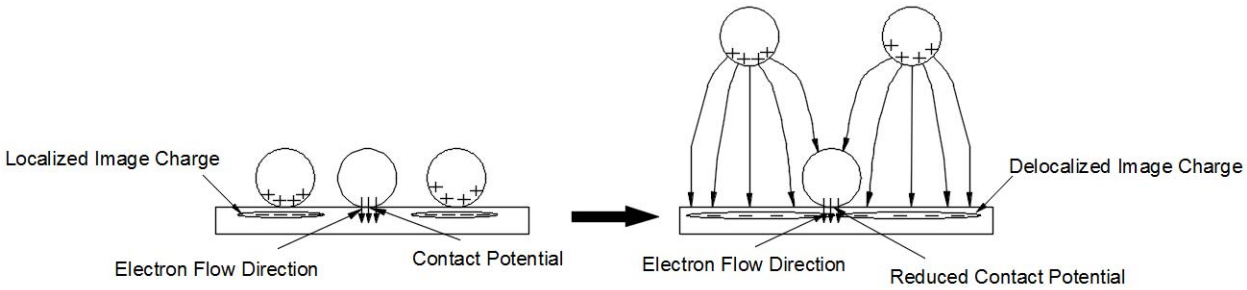

Figure 1.11. Influence of surrounding bounced charged particles on charge transfer process (Ireland 2009).

Terris et al. (1989) have observed the image charge and measured the force gradient between the point charge and the image charge using a microscope tip. The force gradient between the tip and the image charge was reported follow $-[(q_i q_t)/2\pi\varepsilon d^3)]$ where q_t the total charge on the tip, q_e the image charge. Both positive and negative image charge was produced by applying different bias voltage to the tip.

The influence of the electric field generated by the bounced charged particle and delocalized image charge on the charge transfer of other particle tribocharging processes can be calculated using the expression (Ireland 2010):

$$S^1 = \left|\frac{<\sigma_i^1>}{2\sigma_e}\right| = \frac{q_1 A \Lambda}{2\left(\frac{1}{\sigma_i - \mu_1}\right)(A\sigma_e)} \qquad (11)$$

where S^I is the influence factor, Λ is a dimensionless value up to 1, μ_1 the area affected by the electric field generated by bounced particle charged and image charge, which has maximum value of $\pi D_p^2/4$. σ_i^1 is the image charge density distribution on the plane, σ_e the equilibrium charge density, and q_1 is the charge on the bounced particles. Since the influence factor S^I was calculated up to 2.5×10^{-4}, this influence is always considered as secondary determinant of the particle charge transfer efficiency.

The image charge could also influence the tribocharging of the charged particles themselves through the interaction between the image charge and the particle surface charge. Sometimes, the influence of image charge on the tribocharging process might be a dominant factor in some tribocharging systems such as aerosol particles tribocharged with droplets (Tinsley et al., 2000). Charged aerosol particles have higher collision efficiency which is assisted by the image charge forces. The attractive force between the charged aerosol particle and its image charged droplet is strong and short range. This effect greatly enhances the tribocharging efficiency. When the precise calculation of the charged particles interaction is required, the influence of image charge needs to be considered (Horn and Douglas, et al., 1992; Tanoue et al., 2001; Matsusaka, 2011). The image potential generally used in simulation is expressed as:

$$V_e = \frac{2q_1 d}{\pi \varepsilon D_p^2} \tag{12}$$

The effect of the image charge on the particle tribocharging efficiency was also studied by Korevaar and his research group (2013) using tribocharging modeling. It was based on particles being conveyed in a square tube. The study focused on the interaction between the image charge and particle surface charge on the single particle tribocharging efficiency. Their simulation results show that the mean charge of the particles has a significant positive correlation with particle population density. If the particle population density is low, the particle mean charge is low and the interaction between the image charge and particle surface charge in the tribocharging process is negligible. If the particle population per unit volume is high, the mean charge increases accordingly. The image charge is more substantial which attracts the charged particle that is approaching the tube wall, which leads to more collisions between the particle and the wall per unit time. Therefore, the final charge of a single particle is higher under the influence of the image charge.

1.6. Influence of particle motion on the tribocharging

Contact charging of particle and surface can be classified into three types: sliding, rolling and collision. Every type of motion has different charging characteristics and results in different final charge of particles. The motion type influences the particle total contacting area, the interaction force and the energy consumption in tribocharging.

1.6.1. Sliding Tribocharging Process

When a particle is sliding on a flat surface (Figure 1.12), the charge carriers drill into the bulk material through friction at the interface. The charge carrier occupies the previous uncharged material surface during the sliding process.

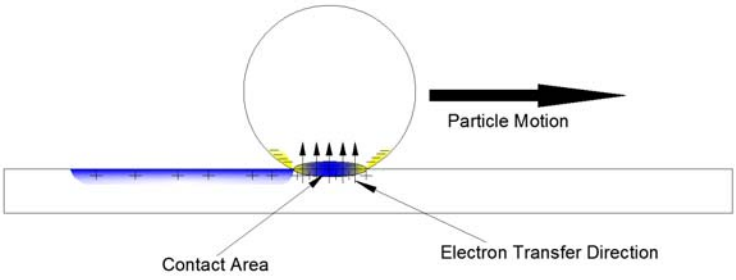

Figure 1.12. Schematic diagram of sliding contact charging between particle and surface.

The actual contact area is determined by the surface roughness, material hardness, and the compression force at the interface. The work consumed at the sliding interface (W) and the coefficient (η) could affect the dynamic saturation charge density. The charge density accumulated on the contacting face can be expressed as (Ireland, 2012):

$$\sigma_e = \sigma_s + \frac{2\eta W C_s}{A^2} \tag{13}$$

This equation indicates that more work provided at the sliding interface by the friction effect results in a higher charge density. Nakayama (1996) discovered that the material surface friction coefficient fluctuated with the sliding distance. The surface potential produced by the tribocharging has a positive correlation with the friction coefficient. Jing et al (2014) have proved this trend that the potential difference between the sliding surfaces is higher with higher sliding velocity, and has the potential to generate electric power as an outside energy source. However, the charge cannot accumulate on the contacting surface infinitely. The changing that occurs due to sliding surface contact causes the equilibrium charge to increase beyond the static contact charge which is a function of the contact area and contact pattern. When it reaches the dynamic saturation value, the discharge occurs due to the potential difference exceeding the gaseous breakdown limit (Ireland, 2008). Material surface composition generally changes with the sliding distance due to the rubbing of the surface which could result in material transfer, molecular rearrangement, and surface disruption. The original surface structure and the composition will be changed or even patched by other materials. Surface friction interaction can totally change the charging characteristics due to surface structure failure and surface oxidization. The charge transfers from high energy states to the low energy states on the non-equilibrium part of the surface (Lowell and Truscott, 1986). The work functions of the contacting surface changes with the surface composition and structure change accordingly which significantly affects the tribocharging process (Chang et al., 2007). Therefore, the charge transfer varies with the changs in surface friction contact. These processes indicate that the sliding contact charging is a complex, dynamic process.

1.6.2. Rolling Tribocharging Process

When the particle motion is a rolling action, the friction force between the contacting surfaces is rolling friction. Rolling friction has a lower friction coefficient that results in a lower friction force and lower energy consumption rate. However, the total contacting surface during rolling contact is much larger compared to the sliding contact friction. The schematic diagram of partition rolling on a plate and the charge exchange is shown in Figure 1.13. Ireland (2010) conducted experiments to study the influence of particle contact mode with the surface on the particle charging. He noticed that the rolling particles tribocharging with the surface is different relative to the sliding motion and that the simple condenser model is not feasible to describe the

associated tribocharging process. The surface tilt angle and the particle interactions are the critical factors determine the particle sliding or rolling on the surface. He proposed the following equation to express the charge accumulated on the particle that is continuously rolling on a flat surface:

$$dq = \frac{A_r\sigma_0 - q_i}{\tau} dt_i \tag{14}$$

$$q(t) = A_r\sigma_e[1 - \exp\left(-\frac{t_i}{\tau}\right)] \tag{15}$$

where A_r is the contact area of rolling particles with the surface, τ is the charging time constant,

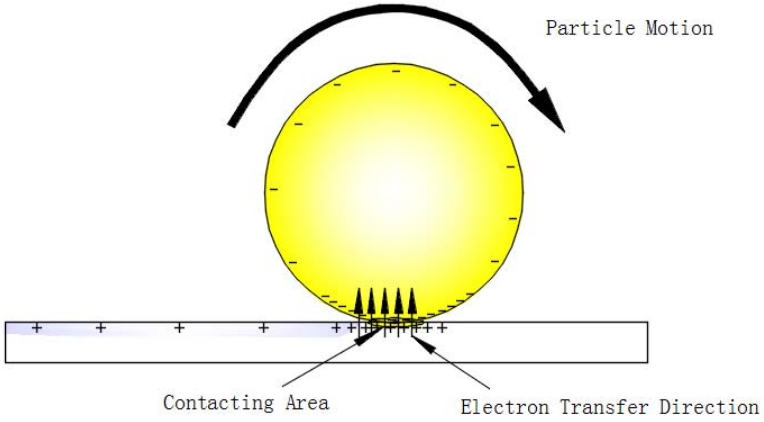

Figure 1.13. Schematic diagram of rolling contact charging between particle and surface.

The equation shows that the accumulated charge on the rolling particle is positively related to the contact area and the contact time. However, the influence of friction force on the rolling particle tribocharging has not been thoroughly evaluated. Ning et al. (2010) studied the rolling and sliding motion on the tribocharging efficiency by monitoring the generated electrostatic potential. He proved that the electrostatic potential is affected by the rolling operation parameters such as compression force, rotation speed, friction heat, and friction coefficient. In addition, there also exists the charge dissipation that is related to charge neutralization and leakage, which is in dynamic balance with the tribocharging process. Tokeshi et al. (2009) found that the rolling and sliding friction would cause almost the same saturation charge, which is not directly related with the friction. The mechanism may be controlled by the contact/separation process that drives charge relaxation. However, the expression for the detailed influence of the friction effect on the rolling particle tribocharging process is not yet known.

1.6.3. Impaction Tribocharging Process

Impaction is the motion with highest interaction force between the contacting surfaces for tribocharging. As a result of the collision between the particle and surface, the momentum transfer at the interface generates a compression force at the interface which is larger than the forces associated with particle sliding and rolling on a surface. The schematic diagram of collision tribocharging and the charge transfer is shown in Figure 1.14. The charging process can be very quick due to the strong interaction force between contacting surfaces and the high energy

consumption rate during collision. Additionally, the discharge process phenomenon is also more obvious due to the high quantity of localized charged retained on the collision surface. Previous researchers have studied the particle collision tribocharging correlated with its elastic property which affects the contacting area during collision (Thornton 1997). To quantify the charging process, assume a particle having a impact velocity of V_I collides with a surface at a 90° angle. The force balance on the particle is:

$$m\delta_o - F_I + G_I = 0 \tag{16}$$

where F_I is the normal contact force acting on the interface, δ_o is the overlap, and G_I is the gravity force of particle. Hu et al. (2012) conducted experiments to study the tribocharging of a single particle colliding with a solid plane. The experimental results showed that the charge transfer direction and quantity was related to particle size and impact velocity. Considering the elastic-plastic model proposed for the particle contact, the normal force was classified by elastic loading, plastic loading and elastic unloading as defined by:

$$F_I = \begin{cases} -1.33E'\sqrt{R_I}\delta_o & for\ elastic\ loading \\ \frac{\sigma_u^3\pi^3{R_I}^2}{12E'^2} - \pi R_I\sigma_u\delta_o & for\ plastic\ loading \\ -1.33E'\sqrt{R_I}(\delta_o - \delta_o^u)^{1.5} & for\ elastic\ unloading \end{cases} \tag{17}$$

where R_I is the equivalent radius of the particle, E' the Young's modulus, σ_u the upper limit of the compressive strength, and δ_o^u is the unrecoverable plastic overlap at the interface.

The upper limit of the compressive strength is $\sigma_u = (1 + \frac{\pi}{2})\sigma_I$, σ_I the compressive strength of the particle. The compressive strength at the center of contact area can be expressed as $\sigma_c = 3F_I/(2\pi R_A^2)$. The plastic deformation starts when the compressive stress at the center of the contact area exceeds the upper limit of the compressive strength. The actual contacting surface area of the particle (A_I) during collision considering the particle modulus can be expressed as:

$$A_I = \begin{cases} 2\pi R_I^2\left(1 - \frac{\sqrt{R_I^2 - R_A^2}}{R_I}\right) & for\ elastic\ loading \\ 2\pi R_I^2\left(\sqrt{R_I^2 - R_p^2} - \sqrt{R_I^2 - R_A^2}\right) = \pi R_p^2 & for\ elastic - plastic\ loading \end{cases} \tag{18}$$

where $R_A = \sqrt{R\delta_o}$ represents the contact radius which is smaller than the particle radius.

The actual contact surface area is not only related with the particle elastic property, but also related to the particle shape and surface roughness (Watanabe et al., 2006). The uneven surface allows the bulges of the particle to more easily touch the plate surface while the depressed portion suspended in the air during collision. The inhomogeneous contact of particle surface leads to the actual contact area variation through impact charging which could be reflected by large variations in recorded charging values during particle charging experiments.

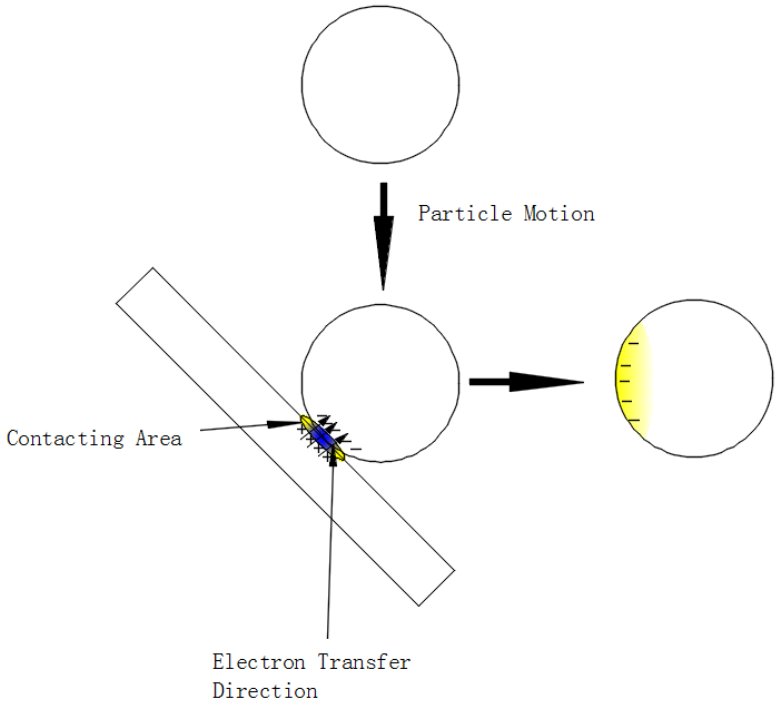

Figure 1.14. Schematic diagram of impaction contact charging between a spherical particle and material having a flat plane.

Xie et al. (2013) investigated the tribocharging of a single ball with repeated collision. The charge residing on the ball increased with each collision until it reached a point of saturation. The saturation charge is a function of the original surface areas of the two objects at the contact region before collision, which is related to the comparative velocity and the particle elastic properties. The charge transfer to the neutral particle during collision can be expressed as:

$$dq = \alpha\rho p_D(1 - p_D)(S_2 - S_1) \tag{19}$$

where α is the probability that charge can transfer between two contacting surfaces, p_D the probability that a position on the surface can lose electron, ρ the density of positions on the surface that can accept or lose electron, S_2 and S_1 represent the original spherical caps of the contacting balls.

Equation (19) indicates that a neutral particle can be tribocharged by another solid surface though collisions based on the material surface electric property as well as the material elasticity and particle size. The sign of original spherical cap area difference S_2-S_1 represents the electron transfer directions between the surfaces. Small particles are easier to charge negatively while large particles prefer to charge positively when they collides with each other. This equation can also be used to explain the bipolar charging phenomenon of the particles made of the same material, which is in accordance with the experiment observations (Ali et al., 1998; Zhao et al., 2000; Forward et al., 2009).

The influence of particle initial charge on particle impact charging with a plate was investigated using a high resolution test rig (Watanabe et al., 2007). The experiment results show that the

particle charge resulting from a single impact a plate is a function of the particle initial charge. The net charge transfer after *n* number of collisions can be quantified:

$$\sum dq = \rho p_D(1-p_D)\sum \alpha_i\{A_2\prod_{i=1}^{n}\left[1-\frac{\alpha_i p_D A_2}{A_1}\right]^{i-1} - A_1[1-\alpha(1-p_D)^{n-1}]\} \quad (20)$$

The tribocharging of fine particles through an impact event was investigated by Tanoue and other researchers in 2001. The impact velocity, contact time, and number of contacts were found to be critical factors in controlling tribocharging. They reported that the smaller particles have smaller contacting time during each collision. The contact time during the collision and the charge exchange per collision has a positive correlation with particle density, particle diameter and impact velocity. They also reported that the ambient atmospheric turbulent condition has significant influences on the small particle tribocharging efficiency. Since small particles have limited inertia, their trajectory is easily affected by the ambient air flow and thus influences the particle collision with the wall. Higher air turbulence could reduce the small particle normal collision velocity and the number of impacts per unit time with the wall thus reduces the tribocharging efficiency.

Poppe and Schrapler in 2005 investigated the correlation of the impaction energy and temperature with the particle tribocharging efficiency. The particle plastic deformation during collision converts the collision energy to the thermal energy which results in a temperature difference between the two contacting objects. The thermal diffusion initiates the negative charge carrier transfer as higher temperatures assist the transfer of negative charges. Thus the researchers believe the temperature difference is the main factor controlling the charge transfer process. The material property difference between the two colliding objects, which is normally the most important factor, was secondary to the temperature effect.

In summary, impact tribocharging is influenced by many factors related to material surface properties, impaction collision, particle physical properties, and ambient environment. However, an accurate expression that can be used to fully describe the impact tribocharging mechanism has yet to be developed.

1.7. Surface roughness and contacting area change in tribocharging process

In the sliding/rolling contact charging procedure, the exact contacting area and the tribocharging conditions between contacting surfaces are continuously changing. Because the contacting surfaces are not completely smooth, the exact contacting area in microscale varies during the sliding/rolling process. Particle mechanical properties like the Young's Modulus and Poisson's Ratio combined with the interactive mode of the contacting surfaces determine how much the deformation of the contacting discrete points and the exact total area involved in tribocharging. The schematic diagram for the tribocharging of a rough surface in microscale is shown in Figure 1.15. The contacting area changes during the sliding/rolling process affects the charge exchange of between the surfaces (Coste and Pechery, 1981; Ireland, 2008). Some parts of the contacting surface separation result in the transferred charge retained on them. When the charged surface contacts a neutral surface, there might be some charges backflow in the reverse direction if the friction energy consumed at the interface is too small to sustain their separation status. Therefore, the charge exchange is not only related to the real contacting area, but also related to the surface localized charges (Cunningham and Hood, 1970). This complex micro contacting area variation makes the charge exchange between the whole surfaces during tribocharging processes more sophisticated. However, practically the exact contacting area change in micro scale has limited effect in charge exchange. The relative moving velocity between the contacting surfaces has more

significant impact on tribocharging. Higher relative velocity results in larger charge exchange rate between the contacting surfaces. (Wahlin and Backstrom, 1974; Wang et al., 2013).

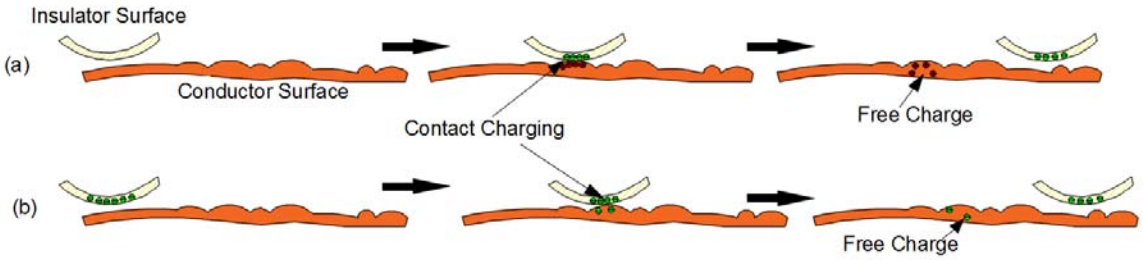

Figure 1.15. Tribocharging process of rough surface in microscale, (a) electron transfers from copper plate to ceramic cylinder surface (b) electron transfers from ceramic cylinder surface to copper plate.

1.8. The outline of this Ph.D. Research

In this Ph.D. study, the fundamental research focused on the tribocharging mechanisms. A more sensitive voltage measurement equipment, oscilloscope, was used to record the voltage signals generated in the rolling and sliding tribocharging process. Signal processing technique was applied to sort out the pulsing signals. The tribocharging kinetics was investigated to discover the electron transfer behaviors. A new method can more quickly and accurately measure the particle surface charge, especially can reliably estimate subtle surface charge, was studied and assessed. Parametric study on the particle tribocharging was conducted to assess their influence on particle surface charge. Finally, a semi-empirical model was established started from the most basic model incorporating the experimental findings. This model can more accurately predict the particle surface charge based on the exact tribocharging conditions.

Particle size that best fitting the RTS separation was a critical parameter needs to be determined. A coal sample was screened into four size fractions that were used to study the size effect. The particle size effect on the particle charging and particle separation were investigated individually. Then their effects are incorporated using mathematical speculation and statistical analysis to derive the influence of particle size on RTS separation efficiency. Fundamental analysis on the particle charge distribution and separation process was conducted to support the experiment result.

A research case study on the RTS separation of pure coal-silica model sample was conducted to evaluate the potential of using the RTS to upgrade silica-rich coal. The operating parameters in influencing the RTS separation efficiency were assessed using single factor experiment design. The optimum operating conditions are determined, which was then used in a five-stage RTS test aiming to establish the coal-silica ideal separation curve obtainable by the RTS. The particle-particle tribocharging effect was tried to be evaluated based on the RTS tribocharging test results of the pure coal, pure silica and coal-silica mixture.

Another case study was conducted on the RTS upgrading of low ash coal, which targeted the ultraclean coal production with ash content <4%. Screening experiment design method and Box-Behnken experiment design method were applied to sort out the significant individual operating parameters and determine the significant parametric interaction on the RTS separation efficiency. The fundamental analysis conclusions derived from previous study were applied here to assess the exact operating parameter influence. Finally, the optimum operating conditions were locked,

and the best quality concentrate produced by the RTS unit with the corresponding experiment error was checked.

2. Feasibility of using oscilloscope to quantify the charge exchange and related fundamentals

2.1. Introduction

Tribocharging is a type of ancient methods to impost static charge to material surface. Many previous researches had tried to discover the tribocharging mechanism based on their experiment phenomena. Since their research objectives and considered charge carriers were different, their conclusions still has not reached a consensus. This study continued the fundamental research based on previous discoveries to dig out more intrinsic information about tribocharging mechanism. How electrons behavior between contacting surfaces during the tribocharging process will be assessed to deepen the understanding of tribocharging mechanism.

The oscilloscope has been reported to try to measure the particle surface charge created through tribocharging (Poppe et al., 2005; Watanabe et al., 2007). Although their studies majorly only focused on the surface charge after the tribocharging, the research results indicated the feasibility of using the oscilloscope recorded signal to quantify the tribocharging. Since the oscilloscope has the characteristic of high sampling rate, it can readily capture the measuring object voltage potential change caused by contingent reasons. As such, it is a powerful tool in particle tribocharging study, the electron transfer between the contacting faces always combining their voltage potentials change. In current study, the oscilloscope was employed to study the tribocharging, especially focused more on the tribocharging process. Rolling and sliding tribocharging were studied since they were forms of "prolonged" tribocharging process. The electrons transfer and behavior, charges relaxation and charges retaining on the surface were intended to be disclosed more comprehensively for further advancement of understanding, control, and utilization of tribocharging.

The recorded signals by the oscilloscope for the tribocharging process were processed by signal processing technique to eliminate the environmental noise. The pulsing signals caused during the tribocharging process were matched to the phenomena occurred in this process. The pulsing signal characteristics that can be used for the particle surface charge quantification were sorted out and studied individually. A new method for surface charge measurement was proposed and assessed, which has higher tolerance for environment noise than the conventional surface charge measurement method.

2.2. Experimental

Contact charge between an insulator and a conductor was studied using a ceramic cylinder with weight of 50±1 g and a copper plate with dimension of 14 cm × 32 cm. The copper plate was inclined at 45 °. Rolling and sliding tribocharging mechanisms were both studied with different relative displacement distances. An oscilloscope was connected to the copper plate which captured the original signals created by the tribocharging process. As shown in Figure 2.1, a Faraday cage was placed below the end of the copper plate to collect the charged ceramic cylinder. An electrometer was connected to the Faraday cage to measure the total net charge of the ceramic cylinder. The ceramic cylinder was found to attain a negative charge after tribocharging, which indicated a transfer of electrons from the copper bulk to the ceramic cylinder surface during the tribocharging process. Because the raw signal includes 60 Hz natural noise (the sinusoidal component from the power source and Gaussian white noise (the ultrahigh frequent component), a notch filter using the IIT Butterworth method with order of 2 was designed to remove the noise between 57 Hz and 63 Hz. Then a lowpass filter using the IIR

Butteworth method with the order of 2 was also used to eliminate the Gaussian white noise higher than 2000 Hz. The typical de-noised signals of rolling and sliding motion (relative displacement distance is 32 cm) after eliminating the natural noise and Gaussian white noise are shown in Figure 2.2.

The experiment procedure used in this study is summarized as follows:

(1) Check the position of each component. Ensure that the inclined angle of the parallel plates is correct. Test the Faraday cage for the ability to collect the particles from the outlet of the tribocharging test equipment.
(2) Turn on the oscilloscope and connect it to the inclined copper plates. Adjust the signal magnitude of the oscilloscope to cover the largest signal peak produced during the tribocharging process. Adjust the time scale of the oscilloscope to provide enough recording time to cover the entire period of the experiment.
(3) Turn on the electrometer and connect it to the personal computer. Set it to the charge measurement mode. Set the electrometer to the zero-check status so that all the charges on the probe will be eliminated.
(4) Ground the copper plates to discharge any accumulated charge and then disconnect the grounding. Put the ceramic cylinder on a grounded metal plate for more than one minute to drain the surface charge on the tested particle.
(5) Ground the Faraday cage to drain the charge the accumulated charge. Afterwards, disconnect the grounding.
(6) Start the recording function of the oscilloscope, the potential signals from the two parallel plates will be sensed and recorded by the oscilloscope.
(7) Initiate the tribocharging between the particle and the inclined copper plate (bottom) with desired relative motion. Allow the particle to pass through the whole length of the copper plate and fall into the Faraday cage.
(8) Save the recorded waveforms obtained from the parallel copper plates to the storage media.
(9) Turn the electrometer to the charge measuring status. Connect the charge measurement probe to the Faraday cage. Measure the charge quantity of the charged particle every 0.5 second for 20 seconds.
(10) Record the measured charge quantity in the personnel computer.

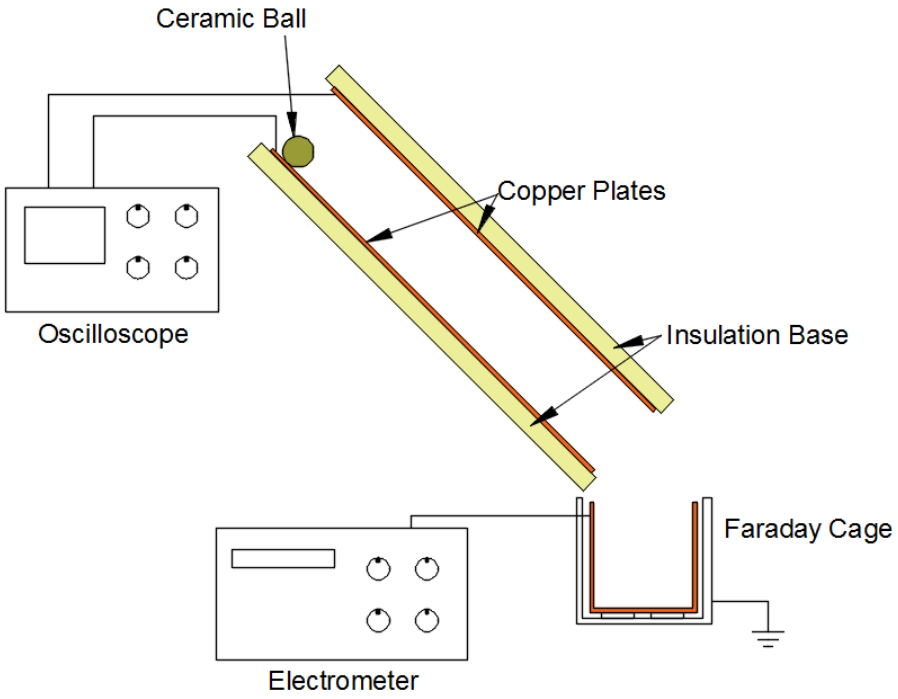

Figure 2.1. Equipment design used for conductor-insulator tribocharging.

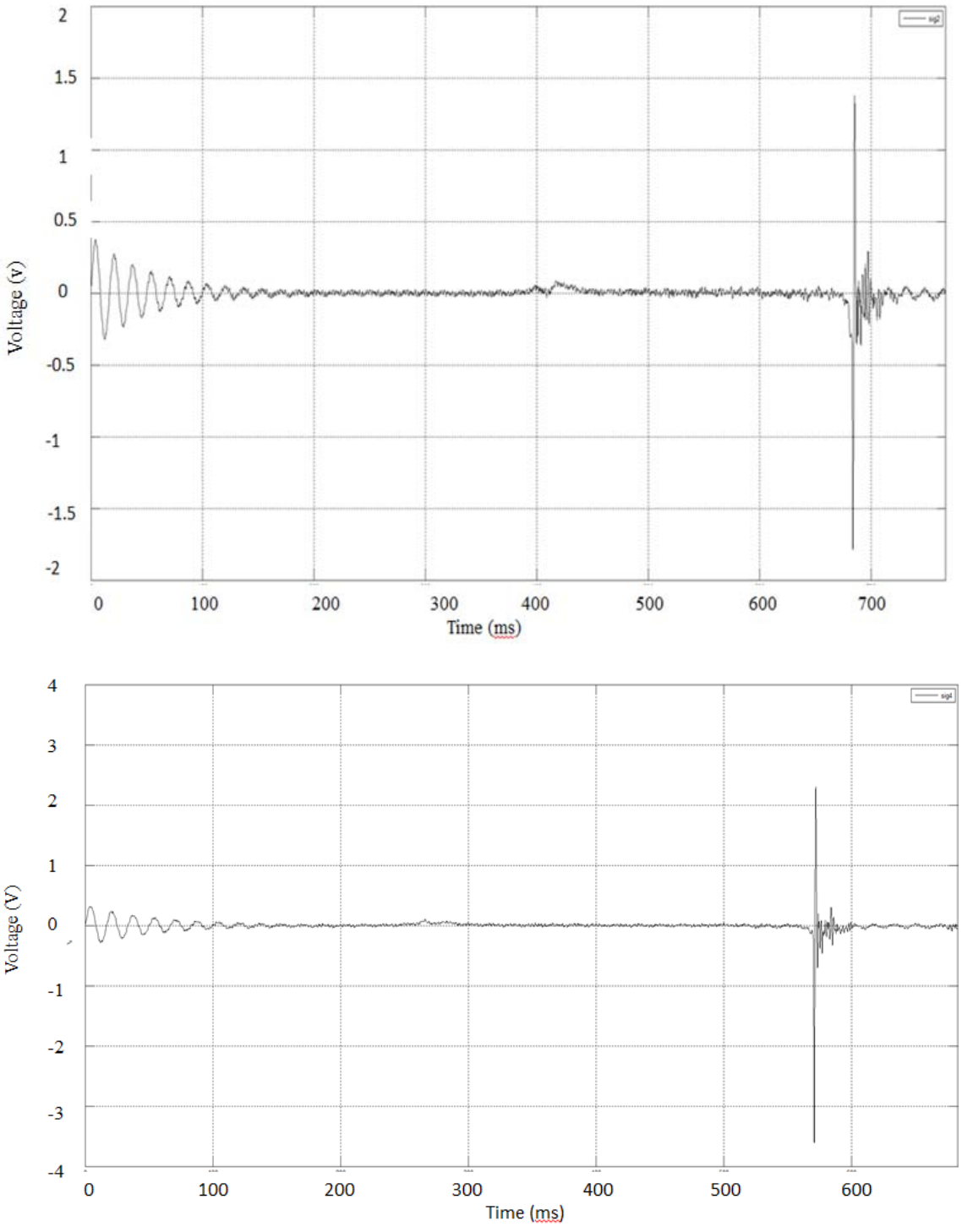

Figure 2.2. Signal of tribocharging process of ceramic cylinder (a) rolling on the copper plate and (b) sliding on the copper plate.

When the ceramic cylinder starts to roll/slide on the copper plate, the friction force is the main resistance for ball motion. The first pulsing signal is indicative of the free charges generated in the copper plate when the ball initiates movement. The charge exchange reaches the balance state (no free charge generated) after the positive pulsing signal. The occurrence of this positive free

charge is likely due to the exchanged charges that penetrate into the bulk of the copper plate. Lowell (1979) reported that the charge transfer not only exist on the surface layer of contacting surfaces, but also exist in a shallow depth below the surface layer. The charge transferred to the deep position in the copper bulk becomes free charge that results in the pulsing signal shown in Figure 2.2.

A schematic of the exchanged charge distribution in the copper plate and in the ceramic cylinder is shown in Figure 2.3. During the rolling/sliding tribocharging, the charge exchange is mainly controlled by the work function difference of the materials. Electron transfers from the surface with lower work function to the one with higher work function. The ceramic cylinder surface work function is higher than the copper surface. The charge quantity can be expressed as:

$$\frac{dq}{ds} = a(1 - e^{\frac{-as}{q_s}}) \tag{21}$$

where "*a*" is the electron accept rate of the copper surface (ceramic cylinder is negatively charger).

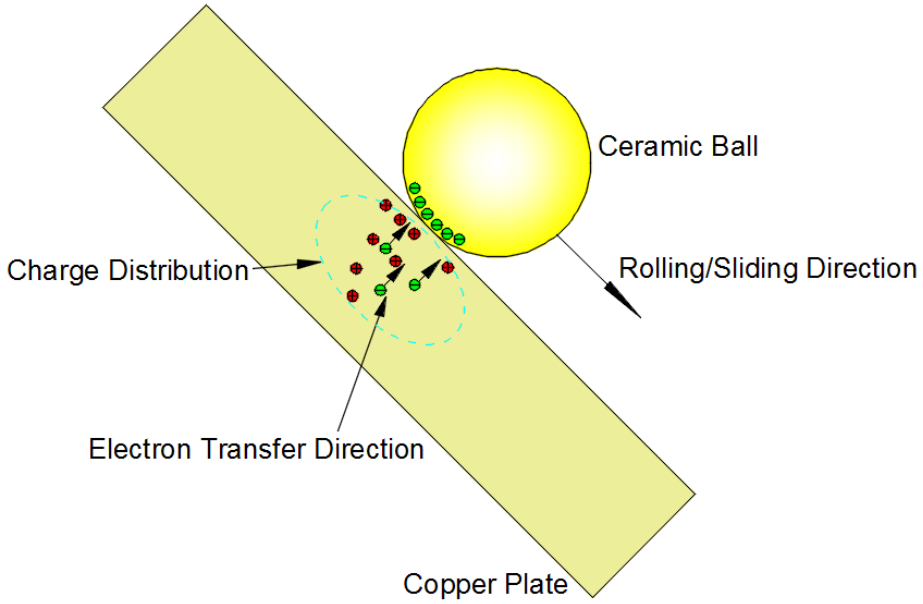

Figure 2.3. Charge transfer and charge distribution in the copper plate and the ceramic cylinder during tribocharging.

Chowdry and Westgate (1974) provided a fundamental explanation of the charge transfer and distribution inside the material based on the traps distribution in the energy gap. The screen length was proposed to estimate the penetration of charge, which equals the "effective" Debye length. The screen distance is the position inside the bulk where the charge density is 1/e of the charge density on the surface. The calculated screen lengths for insulators are very small (below 100 μm). The calculation of the screen length is:

$$l = \int_0^l dx = \int_{V_s}^{V_l} \frac{dV}{F(V)} \quad (22)$$

where V_l and V_s are the electrostatic potential inside the material at distance l and on the surface respectively. The term $F(V)$ is the electrostatic potential changing rate at distance x inside the material, which can be quantified by the first integration of Poisson's equation.

In 1984, Homewood reported a method to calculate the charge penetration into the insulator depth based on an experiment method. The two contacting materials (insulator and metal) were connected to one plate of a capacitance (C_e) respectively. One voltage meter was connected in parallel to the capacitor to measure the voltage. He found that the charge penetration depth in the insulator is related to the insulator depth (L), the capacitance formed by the contacting insulator and metal (C_t), the potential of the two materials in-contact (V_{ic}) and out-of-contact (V_{oc}). In his experiment, the penetration depth into the insulator was found up to 1.15 nm, which is similar to the atomic diameter. The derived equation for the charge penetration depth is:

$$l = L\left(\frac{V_{ic}}{V_{oc}}\right)\left(\frac{C_e + C_t}{C_t}\right) \quad (23)$$

Brennan et al. (1992) obtained a small charge penetration depth into the insulator of up to 3 nm. However, if the insulating material is coated on a metal substrate and then tribocharged with metals, the charge penetration could be much higher. In 1976, Fabish and his research group studied the charge penetration into an insulator during contact charging using different metal substrate. They showed the charge penetration into the insulator is up to 4 μm using indium as a substrate. The charge penetration can reach 4.8 μm or even deeper if gold is used as a substrate. They reported that the metals have different interaction with the insulator surface and bulk states. The charge transfer into the insulator is restricted in a shallow region around the surface while the charge transferred directly into the metal bulk should be much deeper.

Screening length is an index that assesses the extent of electric field penetration in a bulk material. The screening length is the distance between the bulk surface and the position inside the bulk where the absolute potential is $1/e$ of the surface absolute potential. The screening length of metal depends on its dielectric constant. The voltage drop rate inside the metal is smaller which results in larger screening length. Mead et al (1966) studied the penetration of the electric field and found that the screening length in the metal is related to the surface charge and surface state. An opposite charge accumulated at the interface could reduce the field penetration depth. However, the exact penetration depth for copper has not been reported in literature. The charges transferred deeper into the bulk are more probable to become free charges during tribocharging.

As indicated by the experimental results obtained from the use of the extracted oscilloscope signals, rolling and sliding contacts produce similar signals structure. First is the initial positive pulsing signal at the beginning of the ceramic cylinder movement, which is due to the free positive charges generated at the beginning of the tribocharging process that "flows" to the oscilloscope. Because the copper has much larger screening length (related to the conductivity of the material) than the ceramic cylinder, the transferred electrons to the ceramic cylinder stay within several nanometers below the surface. However, the positive "holes" in the copper plate after the electrons transfer distributed more widely below the copper plate surface than the ceramic cylinder. Near surface "holes" can be considered to "neutralize" the transferred electrons on the ceramic cylinder surface. However, the net "un-neutralized" charges on the ceramic surface generate and electric field surrounding it that penetrates the copper bulk. The electric field exerts an electronic force on the "holes" in the copper bulk that drives it with the moving contacting surfaces. When this electronic force is not strong enough to drive the "holes", they become the free charge that is detected by the oscilloscope.

To calculate the electric field penetration, the first step is to estimate the charge distribution in the copper plate during tribocharging. All the net electrons in the ceramic cylinder are considered to be on the surface with the quantity equal to the net "holes" in the coper plate. The exchanged charge distribution in the copper plate should obey the Gaussian law (Chowdry and Westgate, 1974; Saunders et al., 1992). Nicolai et al. (2011) proved that, using a model based on the Gaussian trap distribution within the energy band, the trap energy and the distribution width to simulate the charge transportation into the bulk is very accurate for many materials. Assuming that the probability of an exchanged charge in the metal bulk at distance L below the surface is P, the charge distribution probability function can be written as:

$$P(L) = 2\frac{1}{\sqrt{2\pi\sigma^2}}e^{-\frac{(L-b)^2}{2\sigma^2}} \tag{24}$$

where b is the mean penetration depth, σ is the variance (width of distribution) which is a function of the material property and contact charging condition.

Assume the total transferred charge quantity to the copper is Q_t. If the net charge (Q_1) from the copper top surface l=0 to a specific distance $l=l_1$ below the copper surface neutralizes the opposite charges on the ceramic cylinder surface in equal quantity. The "un-neutralized" charge (Q_t) on the ceramic cylinder surface equals the charge distributed inside the copper bulk. The relations can be described by:

$$\begin{cases} Q_1 = 2Q_t\int_0^{l_1} dlP(l) \\ Q_2 = Q_t - Q_1 \end{cases} \tag{25}$$

The "unnutralized" charges in the interface create electric field that penetrates into the copper plate. The field strength diminishes with increasing depth. The copper dielectric constant is about $\varepsilon_c = 6.1$. According to the classic theory of electrostatics, the electric field generated by a point charge surrounds it. The electric field strength (E_l) at one point inside the copper plate is related to the copper relative dielectric constant (ε_c) and the distance between the point and the charge (d_l). Therefore, the electric field strength and the potential (P_l) at this point can be expressed as:

$$E_l = \frac{e}{4\pi\varepsilon_0\varepsilon_c l^2};\ P_l = \frac{e}{4\pi\varepsilon_0\varepsilon_c l} \tag{26}$$

which assumes that the "un-neutralized" charge is homogeneously distributed on the contacting surface. The potential at any point inside the copper plate is calculated by the summation of the potential of all charges (Zhao and Comber, 2000). If the charge density of the "unneutralized" charge at the contacting surface (S) is σ_s, the electric field (E_s) caused by the charge distributed on the surface at the observation point is:

$$E_s = \int\frac{\sigma_s+\sigma_e}{4\pi\varepsilon_0\varepsilon_c l^2}ds \tag{27}$$

where σ_e is the equivalent surface charge density at the interfaces, which is calculated by:

$$\sigma_e = L^{-1}G \tag{28}$$

L^{-1} is the inverse linear operator which correlates to the geometry, G a boundary conditions related matrix. Zhao and Comber (2000) recommended using the weighted residual method to solve σ_e.

The electric field provides the driving force for the exchanged charge moving inside the copper plate. If the electric force on the charge is larger than the resistance to allow it moves inside the

copper plate, the electric field strength at this point is considered to be "effective". If the deepest penetration point where the electric field strength is "effective" is l_2, the electric field is generated by the "un-neutralized" charge in a limited area (S_e) directly above the point. The schematic diagram of charge exchange, charge distribution, and charge capture is shown in Figure 2.4.

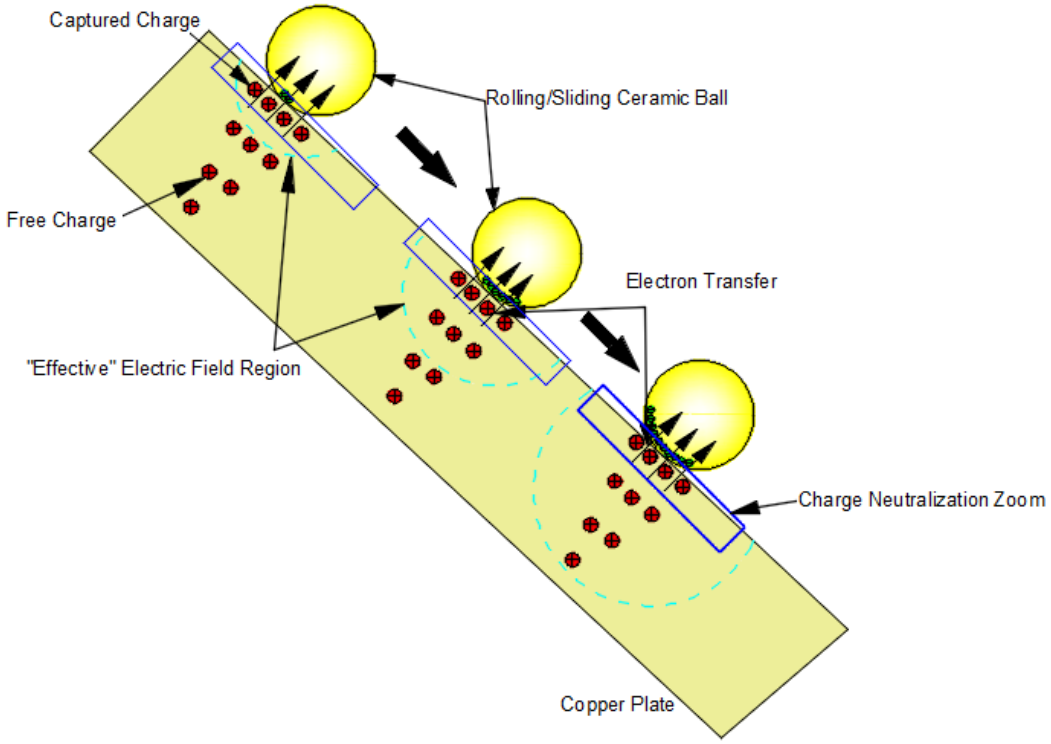

Figure 2.4. Schematic diagram of free charge generated during rolling/sliding tribocharging process.

Therefore, at the beginning of tribocharging process, "un-neutralized" charge accumulates on the ceramic cylinder surface and the charge in the deep copper bulk becomes free charge. The pulsing signal in the rolling process has a larger voltage and longer time than the signal in the sliding process (Figure 2.2) most likely due to its larger total contacting area. Some negative charges are retained on the rolling ball surface after it separates from the copper surface. After the charge exchange between the contacting surfaces reaches a balanced state, there are no free charges left in the copper plate to be generated. This can be reflected by the signal in that there are no pulsing signals detected until the ceramic cylinder leaves the copper plate. However, the charge exchange between the ceramic cylinder and the copper plate still exists. The charge exchange is related to the energy consumption at the interface (Nakayama, 1996; Dragan et al., 2011; Buda et al., 2013). The exchanged charge between the contacting surfaces reaches a maximum value which corresponds to the work function difference and the energy consumption. Total exchanged charge will retain on either part of the contacting surfaces.

After the initial positive pulsing signal, there were no pulsing signals generated until a strong negative pulsing signal (Figure 2.2). This finding indicates that the exchanged charges between the contacting surfaces were all attracted at the interface. In other words, no free charges were generated during this period. The electric field produced by the net charges on the ceramic cylinder surface was strong enough to capture all the generated "holes".

The strong negative pulsing signal in Figure 2.2 occurred when the ceramic cylinder started to leave the copper plate. The accumulated charges at the interface began separating. The free electrons in the copper plate were repelled by the negative charge on the ceramic cylinder and move to the infinite end during this time period. After the negative pulsing signal, a strong positive signal was recorded which was likely caused by the charge relaxation between the two surfaces. The majority of the remaining positive charges previously attracted to the copper surface become free charge. With the ceramic cylinder movement, the distance between the copper plate surface and the ceramic cylinder surface increases. This action causes an increase in the voltage drop within the gap. Charge relaxation occurred if the voltage drop exceeded the limit based on Paschen's law. A strong interaction between the separated charges disappeared. This critical distance equals the distance of the capacitance disappearance.

During the charge separation process, the charge balance at the contacting surface during tribocharging is broken. The interaction between the charges on the ceramic cylinder surface and the charges inside the copper plate produced the strong negative pulsing signal shown in Figure 2.2. The charges interactions during the separation of the ceramic cylinder from the copper plate are shown in Figure 2.5. When the surfaces begin to separate, the negative charge on the ceramic cylinder will attract positive charges towards the copper plate surface while the free electrons will be repelled to the infinite end. When the gap after separation is small, the copper plate surface and the ceramic cylinder surface form a capacitor. The voltage drop within the gap rises with gap distance, which continuously repels the free electrons inside the copper bulk to the infinite end. This explains the source of the strong negative voltage signal.

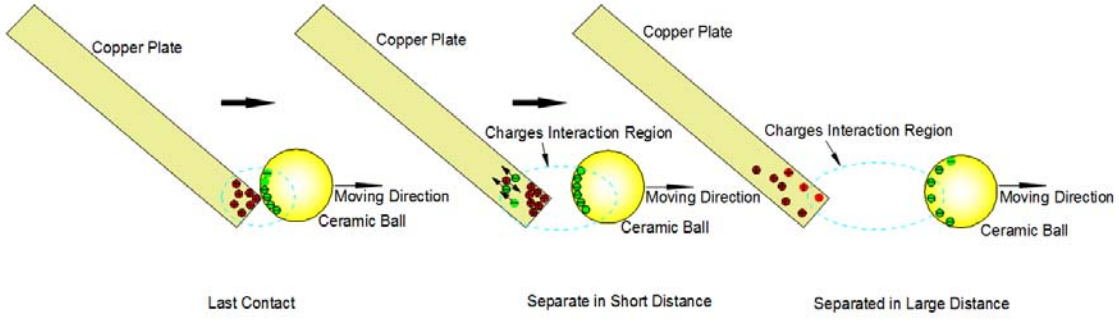

Figure 2.5. Charges separation and interaction during the separation of ceramic cylinder from the copper plate.

Because the capacitance reduces with increasing of the gap distance, the voltage drop builds up inside the gap. When the gap distance reaches a critical value, a charge breakdown might may occur if the voltage drop between the two plates exceeds the limit defined by Paschen's law (Matsusaka, 2011). Himle and Wallash (2002) measured the air breakdown voltage through tribocharging and found values ranging from 1.6 V to 20V. The gas dielectric strength was directly related to the charge breakdown voltage (Soh, et al., 2014). If the last contacting surfaces are smaller, the capacitance composed of these two surfaces area is smaller. This will cause the voltage drop within the gap to rise more quickly, which makes the charge breakdown easier and quicker. Since the charge breakdown results in the charge quantities on the two surfaces of the capacitor to abruptly reduce, the strong interaction between the separated charges disappears. This mechanism could be the reason that tribocharging by impaction has the shortest negative voltage time period while the rolling movement has the largest. Therefore, this gap distance also equals the threshold for the vanishing of the capacitor. As such, the positive charges on the copper plate are no longer held on the copper surface and the majority becomes immediately free charges. The free positive charges are detected by the oscilloscope through the generation of a

strong positive signal. A larger positive signal should represent a higher final charge quantity transferred onto the ceramic cylinder surface. The threshold value for the disappearance of the capacitance could be estimated by the ceramic cylinder motion and the time period of the negative signal.

2.3. Quantitative correlation between the particle surface charge and oscilloscope signals

The experimental result analyses based on the oscilloscope signal shows that the positive pulsing signal has direct correlation with the particle surface charge. There are three indexes from the positive pulsing signal that can be used to establish this correlation. The first index is the peak value (maximum voltage) of the positive pulsing signal. The second one is the mean value (mean voltage value of the whole time period) of the positive pulsing signal while the last one is the total area (voltage ·time) covered by the positive pulsing signal. When the ceramic cylinder rolls or slides on the copper plate at different distances, the total surface charge of the ceramic cylinder are measured by the electrometer, while the signals of the tribocharging process are recorded by the oscilloscope. Experiment results are shown in Table 2.1 and correlated between the particle surface charge and the signal characteristics by through linear regression in Figure 2.6.

Table 2.1. Experiment data of conductor-insulator tribocharging.

Tribocharging Mode								
Relative Displacement, cm	Rolling				Sliding			
	Total Surface charge, nC	Peak Voltage, mV	Mean Voltage, mV	Total Area, mV ·ms	Total Surface charge, nC	Peak Voltage, mV	Mean Voltage, mV	Total Area, mV ·ms
8	-0.318	1023	540	711	-0.2334	1510	833	868
16	-0.345	1437	728	822	-0.32943	1715	1012	965
24	-0.378	1577	921	961	-0.54232	2001	1213	1121
32	-0.494	1799	1088	1132	-0.88433	2460	1411	1479

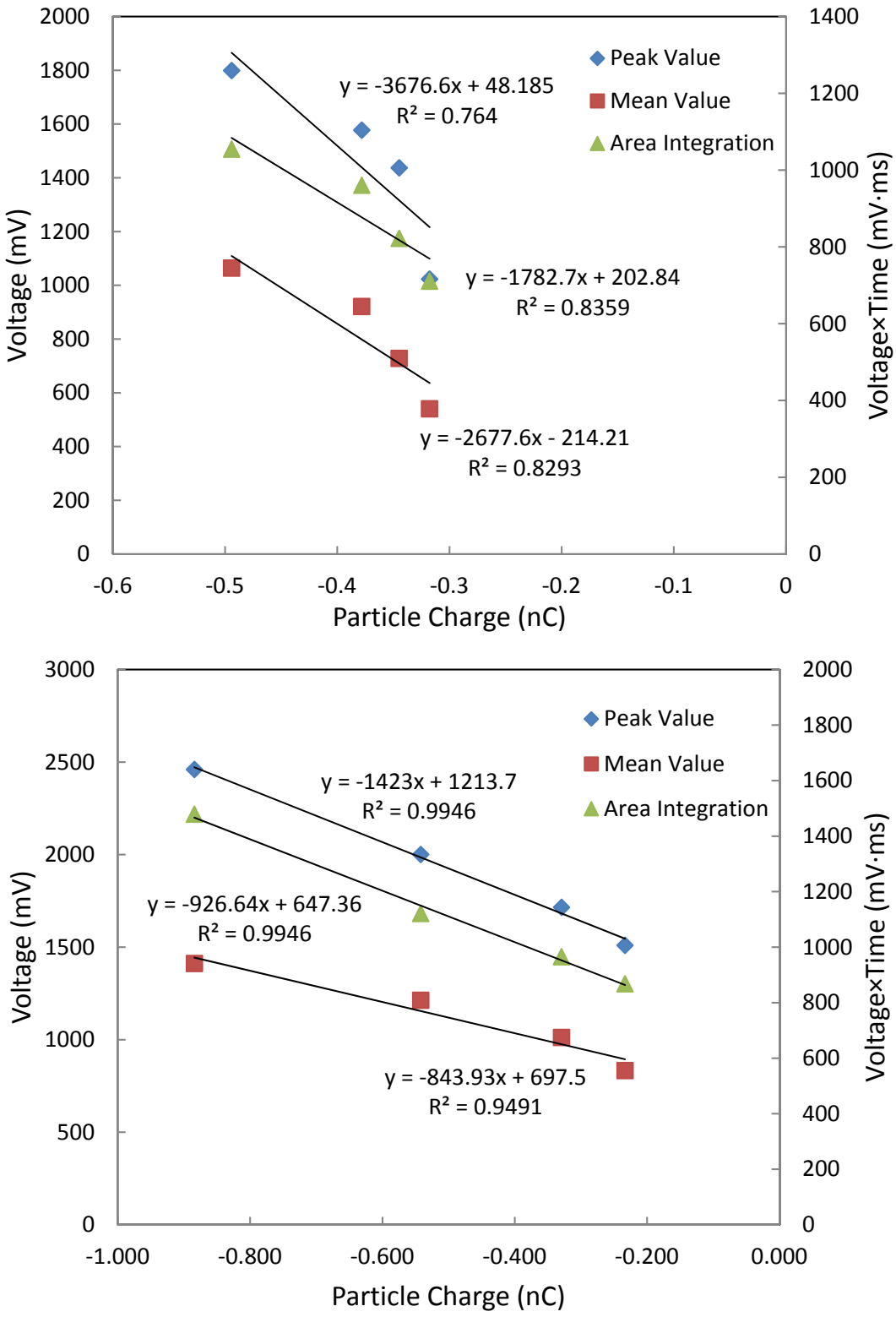

Figure 2.6. Correlation between the particle final charge and the oscilloscope signal characteristics for (a) rolling tribocharging and (b) sliding tribocharging.

There are two reasons for using the oscilloscope signal to quantify particle final charge instead of using the electrometer. First, the oscilloscope can quickly and accurately respond to the voltage which assists with analyzing the charge exchange during the tribocharging process. The electrometer is not capable of achieving this task. Secondly, when the particle total charge is too low, it is very unreliable to use the electrometer to measure it directly, though theoretically it is feasible. The oscilloscope provides a better alternative to filter the environmental noise which results in a more stable experiment result. Therefore, using the oscilloscope signal to quantify the particle surface charge as an alternative is necessary.

The experiment results in Table 2.1 shows that the rolling tribocharging has a narrower particle surface charge range with different relative displacement than the sliding tribocharging. When the relative displacement is low, the ceramic cylinder has higher surface charge with the rolling motion. With an increase of the relative displacement, the ceramic cylinder surface charge quantity increases faster with the sliding motion. This finding is because, at the shortest relative displacement, the total contact area involved in the rolling motion is larger than the sliding motion, which contributes the most to the particle final charge quantity. With an increase in relative displacement, the interactive effect (frictional effect) at the interface becomes more dominant which causes the particle surface charge quantity generated from the sliding contact to rise much faster than the rolling contact. As such, the surface contacting area is more significant in influencing the particle tribocharging at the beginning of movement. Afterwards, the interactive effect (energy consumption rate) becomes more significant in increasing the particle's final charge.

Considering a ceramic cylinder radius R and average distance between the contacting surfaces z, the calculated capacitance (Terris et al., 1989; Matsusaka and Masuda, 2003) generated by the contacting surfaces is:

$$C = 4\pi\epsilon_0 R sinh\alpha \sum_{n=1}^{\infty} (sinhn\alpha)^{-1} \tag{29}$$

$$A_r = 4\pi z_c R sinh\alpha \sum_{n=1}^{\infty} (sinhn\alpha)^{-1} \tag{30}$$

where $\alpha = cosh^{-1}(\frac{H}{R})$ and $H = R + z$, z_c is the critical gap including the surfaces roughness.

As for the particle charging, it is correlated with the contact area A_r, charging time constant τ, contact potential V_c and the charging efficiency k_i, as expressed by:

$$\frac{dq}{d\tau} = k_i C V_c \tag{31}$$

If the charge relaxation (related to charge relaxation efficiency k_r and charge relaxation time τ_r) during the separation of surfaces is taken into account, the particle charging process can be modified to be:

$$\frac{dq}{d\tau} = k_i C V - k_r q \tau_r \tag{32}$$

Since the same ceramic cylinder was used for both rolling and sliding contact tests, the capacitances composed of the ceramic cylinder surface and the copper surface are identical. The contribution of the total contacting surface area to the particle final charge is caused by the changing V_c. The rolling motion has a larger total contact area during the tribocharging process. When the new surface touches the copper surface, the V_c is increased since the fresh surface is uncharged. A ceramic surface previously contacted could bring out some electrons that transfer

into the deepest positions. The surface area that influences the particle rolling charging rate was also proven by Peterson (1954).

Energy consumption is another critical factor influencing the final particle charge. The surfaces' Fermi levels difference determines the maximum particle static surface charge density, σ_0, generated through contact. The interactive force at the contacting surfaces could affect the probability of electron transfer. In other words, some sites in the bulks have enough Fermi level differences to support the electron transfer but the probability of a charge transfer under this condition is not 100%. Energy consumed at the interface could facilitate the initiation of a charge transfer between the surface sites which have enough electrostatic potential difference. The particle dynamic saturation charge density, σ_s, was introduced to describe the influence of energy consumption E_c(Ireland, 2012):

$$\sigma_s = \sqrt{\frac{1}{2}\sigma_0^2 + \frac{\eta E_c C}{A^2}} \tag{33}$$

For the same materials in the tribocharging process, surface states density of sites losing electrons (donor, ρ_D) and accepting electrons (acceptor, ρ_A) are identical. The energy consumption at the interface during the tribocharging process influences the charge transfer efficiency ($f(E)$) of a donor from one surface to an acceptor in the other surface. The charge transfer expression involves the surface state densities in the contacting surfaces ($\rho_{D1}, \rho_{A1}, \rho_{D2}, \rho_{A2}$) and the charge transfer efficiency ($f_1(E), f_2(E)$) is expressed as (Matsusaka et al., 2010):

$$\nabla q = \int_{\langle E_l \rangle}^{\langle E_h \rangle} \min[\rho_{D2}(E), \rho_{A1}(E)]\, f_2(E)[1 - f_1(E)]dE - \int_{\langle E_l \rangle}^{\langle E_h \rangle} \min[\rho_{D1}(E), \rho_{A2}(E)]\, f_1(E)[1 - f_2(E)]dE \tag{34}$$

where $\langle E_l \rangle$ and $\langle E_h \rangle$ are the centroids of low energy consumption and high energy consumption sites respectively, within the energy consumption distribution at the interface.

Obviously, if surface 1 is positively charged after contact, it must have $\rho_{D1} > \rho_{A1}$ and $\rho_{D1} f_1(E) > \rho_{D2} f_2(E)$. The sliding frictional coefficient is much larger than rolling frictional coefficient, which generally can be ten times larger. With the increasing of the sliding viscosity, the sliding frictional coefficient rises correspondingly. It infers that the energy consumption caused by the sliding friction becomes higher than the rolling friction with an elevation of the relative moving velocity. As such, the charge transfer efficiency of the sliding contact is higher after the critical relative displacement, which leads to a higher particle final.

The linear regression analysis was used to correlate the ceramic cylinder final charge with the indexes extracted from the oscilloscope signal. The results show that the area integration better correlated with the final surface charge with rolling and sliding contacts as indicated by R^2 values of 0.8359 and 0.9946 respectively. As such the area of the pulsing signals could be best used as an alternative to quantify the particle final charge or the total charge transfer during the tribocharging process.

2.4. Summary

In this study, a pioneering method was developed to study the particle tribocharging process using an oscilloscope and the signal process technique. The pulsing signals generated from the particle tribocharging process convey information about the charge exchange between contacting surfaces. When the contacting surfaces start their relative movement, there is a charge transfer from one surface to the other. The exchanged charges stay on the shallow surface of the ceramic cylinder while injected deeply into the copper bulk, which is correlated with particle physical idiosyncrasies. Some free charges in the copper bulk will escape is they are not captured by the net accumulated charges at the interface. This result provides a feasible potential to quantify the charge penetration depth into conductor bulk during tribocharging. When the contacting surfaces start separation, the separated charges attract each other and the separating surfaces resemble a capacitor. Air molecules within the gap can be ionized which elevates the likelihood of discharge. Charge relaxation can occur if the voltage drop breaches the Paschen's Law limit. All the tribocharging processes can be detected and quantified by the pulsing signals recorded by the oscilloscope. The last strong pulsing signal was found to be related to the residual charge after the tribocharging process. This study portrays some key tribocharging characteristics

A new charge quantification method was developed by correlating the particle surface charge with the pulsing signal characteristics. Since the last strong pulsing signal is qualitatively directly correlated with the particle surface residual charge after contact charging, such signal properties as the peak voltage, mean voltage and integrate area are used to directly measure particle surface charge. The linear correlation results of both rolling and sliding contacts show that signal area can best describe the particle surface charge, which will be used in the next section for particle charge quantification. The merit of using this method rather than the traditional charge measurement using an electrometer is that it can quickly sense the charge exchanges and accurately gauge the quantity of the exchanged charge. The environmental noise was effectively prevented from affecting the particle charge measurement, which is a significant advancement over the traditional method if the particle surface charge is weak. As a result, this study provides a reliable alternative to estimate the particle surface charge, which is especially useful for weak surface charge measurement.

3. Parametric study on particle tribocharging

3.1. Introduction

The compression model provides a basic insight into the tribocharging mechanism. The electrons play the role of charge carrier during the tribocharging process. Particle physical property and surface electronic properties determines the electron transfer direction and quantity. However, this model oversimplified the tribocharging reality. There are many factors, especially operating parameters, have been reported to have significant impact in particle tribocharging. To better explain the influences of operating conditions, a new model extended from the basic compression model is necessary to better fit the tribocharging reality. As such, the particle surface charge can be more precisely predicted.

Environmental moisture is a critical factor influencing particle surface electronic properties and particle tribocharging. Particle surface moisture increases with prolonged exposure to the environment. Absorbed water may chemically react with the surface material or facilitate reactions between air components and the surface material. The newly created surface groups have different surface properties which modify the original surface electronic properties (Trigwell et al., 2003; Masuda et al., 2004). Additionally, water film formed on the material surface can hide a portion or even all of the original surface deteriorating the surface contact, create particle surface contamination, and change the surface acidity (Eilbeck et al., 2000; Wiles et al., 2004; McCarty et al., 2008; Choi et al., 2017). The ambient moisture was reported to have both positive and negative effect in increasing the particle tribocharging efficiency (Rowley, and Mackin, 2003; Thomas et al., 2008). Particle discharge is also caused by the presence of atmospheric moisture. Since a layer of water film formed on the particle surface negatively affects charge retention the term “leak away” is often used to describe the impact. Additionally, atmosphere moisture changes the atmosphere conductivity, which makes particle discharge easier to happen. However, a few researchers have previously reported contradictory results. In study conducted by Lacks and Sankaran (2011), a thin water layer on particle surfaces was reported to mitigate charge leakage. As a result, extremely low or moderate-to-high moisture levels may be detrimental to the tribocharging process.

There are some other factors has also been reported to be significant in influencing particle tribocharging. The energy consumption at the interface is directly correlated with the electron transfer between contacting surfaces. The energy consumption is controlled by the interactive force (Ireland, 2012), friction coefficient (tribocharging type) (Park et al, 2004) and tribocharging time (relative displacement) (Matsusaka, 2011). In this study, these operating parameters were strictly controlled to investigate their patterns and quantities impacting the particle tribocharging. Finally a semi-empirical model based on this study was established to depict the parametric influences on particle tribocharging and predict particle surface charge.

3.2. Experimental

To study the operating parameters influencing the particle tribocharging, an environmental chamber is used to strictly control the atmosphere condition inside the chamber. The configuration of the environmental chamber and apparatus is shown in Figure 3.1. A humidity meter was used to monitor the environment relative humidity. A dehumidifier and a humidifier were designed to adjust the relative humidity of the atmosphere inside the chamber, which controlled the relative humidity to within 1% of the target value. A copper plate with an adjustable degree of inclination degree was placed used inside the chamber as the surface for charging particles of different types. The normal force at the contacting interface was evaluated based on the copper plate inclining angle. Particles rolled or slid on the copper plate and were

finally collected in a box below the discharge end of the plate. The copper plate was connected to the oscilloscope outside the chamber. The oscilloscope recorded the charging process. The procedure of the particle tribocharging test under a controlled environment is detailed below:

(1) Determine if the relative humidity of the air inside the environmental chamber is at the desired level and stable.
(2) Place the dry testing material inside the environmental chamber for a whole day to ensure the material surface water content is balanced.
(3) Polish and clean the copper surface, place it inside the chamber at a desired inclining angle for a whole day.
(4) Check the function of each component. Check the inclined angle of the parallel plates. Check the connection of the copper plate to the oscilloscope.
(5) Turn on the oscilloscope. Adjust the signal magnitude of the oscilloscope so that it can cover the strongest pulsing signal peak produced during the tribocharging process. Adjust the time scale of the oscilloscope to allow sufficient time for recording the whole tribocharging process;
(6) Ground the copper plate to discharge any accumulated charge and then disconnect the grounding. Put the test particles on a grounded metal plate for more than one minute to drain the surface charge;
(7) Start the recording function of the oscilloscope;
(8) Initiate the tribocharging test by sliding/rolling particles on inclined copper plate through mechanical activation;
(9) Save the recorded waveforms obtained from the copper plates to storage media.

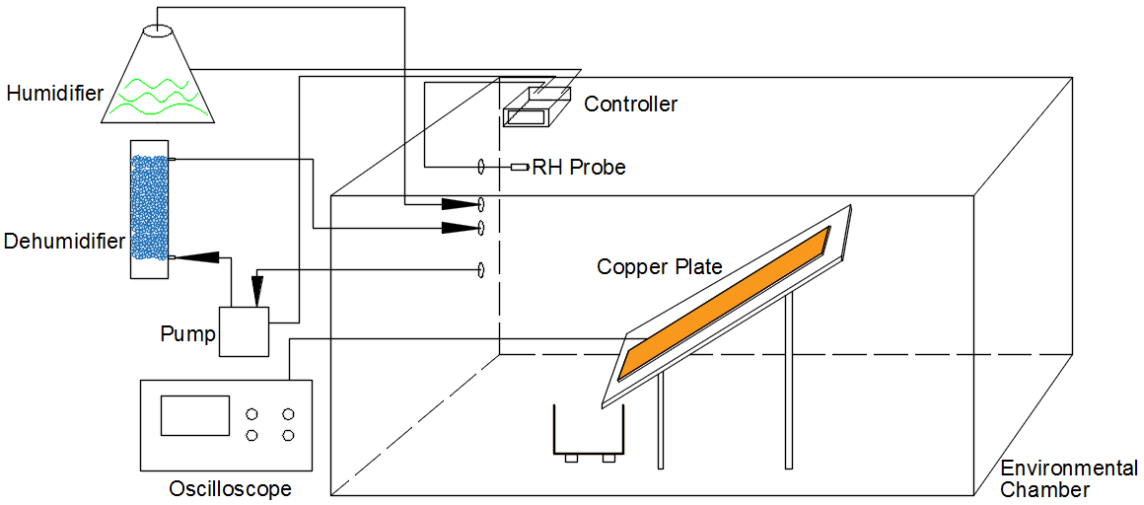

Figure 3.1. Schematic diagram of the environmental chamber humidity control system used for the particle tribocharging test.

The relative humidity of the atmosphere inside the chamber can be adjusted from 1% to 85%, which allowed an evaluation of its influence. The relative humidity must keep stable for a whole day before the particle tribocharging test to ensure that the surface water content on the particle is at equilibrium. The temperature was controlled at 25℃±3℃ based on recorded values during the time period that all tests were conducted. The total length of the copper plate was 32 cm. The

copper plate inclined angle was adjusted to values of 25°or 40°, which provided the ability to assess the impact of the normal force. The raw signals of the particle tribocharging test were transferred to a personal computer and analyzed using Matlab software (MathWorks) to assist in evaluating the particle tribocharging characteristics.

The raw signals contain major disturbances from natural noise at a frequency of around 60 Hz as well as high frequencies due to Gaussian White noise. A notch filter using IIR Butterworth method with an order of 2 was utilized to first remove the signals between 57 Hz and 63 Hz from the raw signals. Next, a lowpass filter using IIR Butterworth method with order of 2 was designed to filter the higher than 2000 Hz signals from the raw signals. Based on the conclusions presented in Chapter 2, the cumulative area of the last pulsing signal (e.g. the strong positive pulsing signal for the tested ceramic cylinder) was used to evaluate the particle total surface charge quantity and polarity. Hence the total areas of the pulsing signals from different tests were used to compare the particle tribocharging efficiency under different operating conditions.

3.3. Tribocharging by rolling action

In this set of tribocharging tests, ceramic cylinders were used as the standard testing material to contact charge with the copper plate under a specific humidity and inclined angle. The effects of normal forces at the interface on the particle tribocharging can be evaluated. Different humidity levels and particle relative displacements were adjusted to study their influence on particle charge. The experimental results obtained by rolling action as a function of particle relative displacement (i.e., distance moved along the plate) are shown in Table 3.1. The ceramic cylinder has weight of 50±1 g (diameter: 18 mm, length: 13 mm). After processing the oscilloscope signals obtained from the tribocharging test, the total areas of the last strong positive pulsing signals were presented to evaluate the total particle surface charge quantities and do the comparison.

Table 3.1. Surface charges generated by rolling action on a copper plate over a range of relative humidity and displacement values at two plate inclination settings.

Inclined Angle		25°				40°			
		Signal Area, ms*mv				Signal Area, ms*mv			
Relative Displacement, cm		8	16	24	32	8	16	24	32
Relative Humidity	1%	5.058	8.639	9.890	11.306	4.688	5.542	6.573	7.629
	5%	5.938	9.712	10.846	10.015	4.975	6.066	8.337	8.250
	10%	5.940	9.659	10.621	11.381	5.863	6.205	8.555	8.757
	15%	6.313	11.802	14.623	15.283	6.292	6.425	8.885	8.941
	20%	8.871	13.094	19.451	20.824	7.615	7.831	9.152	9.727
	25%	5.706	7.781	10.005	13.561	4.881	4.910	5.718	5.851
	38%	5.481	6.784	7.041	7.396	3.542	3.868	4.457	4.504
	50%	1.572	2.017	2.032	3.369	1.358	1.872	1.899	2.079
	65%	1.402	1.545	1.601	2.542	1.282	1.481	1.534	1.590
	75%	0.000	0.049	0.801	1.068	0.000	0.000	0.000	1.068
	85%	0.000	0.000	0.000	0.000	0.000	0.000	0.000	0.000

The influences of relative humidity level, copper plate inclining angle and particle displacement were significant on the ceramic cylinder particle charging. It is clean from Figure 3.2 (a) and (b) that the total charge on a particle accumulates as the particle rolls down the plate with the highest charge occurring at the discharge of the plate. One explanation is that every chargeable site on the ceramic cylinder surface has higher probability to be charged with the increasing displacement. According to the previous published researches, the available chargeable sites on the particle surface cannot reach saturation in one or few contacts between the two contacting materials. Increasing the numbers of interaction (or prolong the time of interaction) between contacting surfaces can enhance the average surface charge densities (Matsusaka et al., 2010; Pei et al., 2015). Additionally, with the increasing of the particle sliding distance, the ceramic cylinder velocity is rising when leaving the copper plate. The higher relative moving velocity elevates the instantaneous energy consumption rate at the interface that enhances the particle tribocharging efficiency (Miloudi et al., 2011; Zelmat et al., 2013). By comparing Figure 3.2 (a) and (b), it is proven that a lower plate inclination is preferred for particle charging

Based on the experiment results, the statistical relationship between the particle total charge and the relative displacement is depicted in Figure 3.3. This plot contains all the data with different copper plate inclining angles. The experiment result is in accordance with previous discoveries.

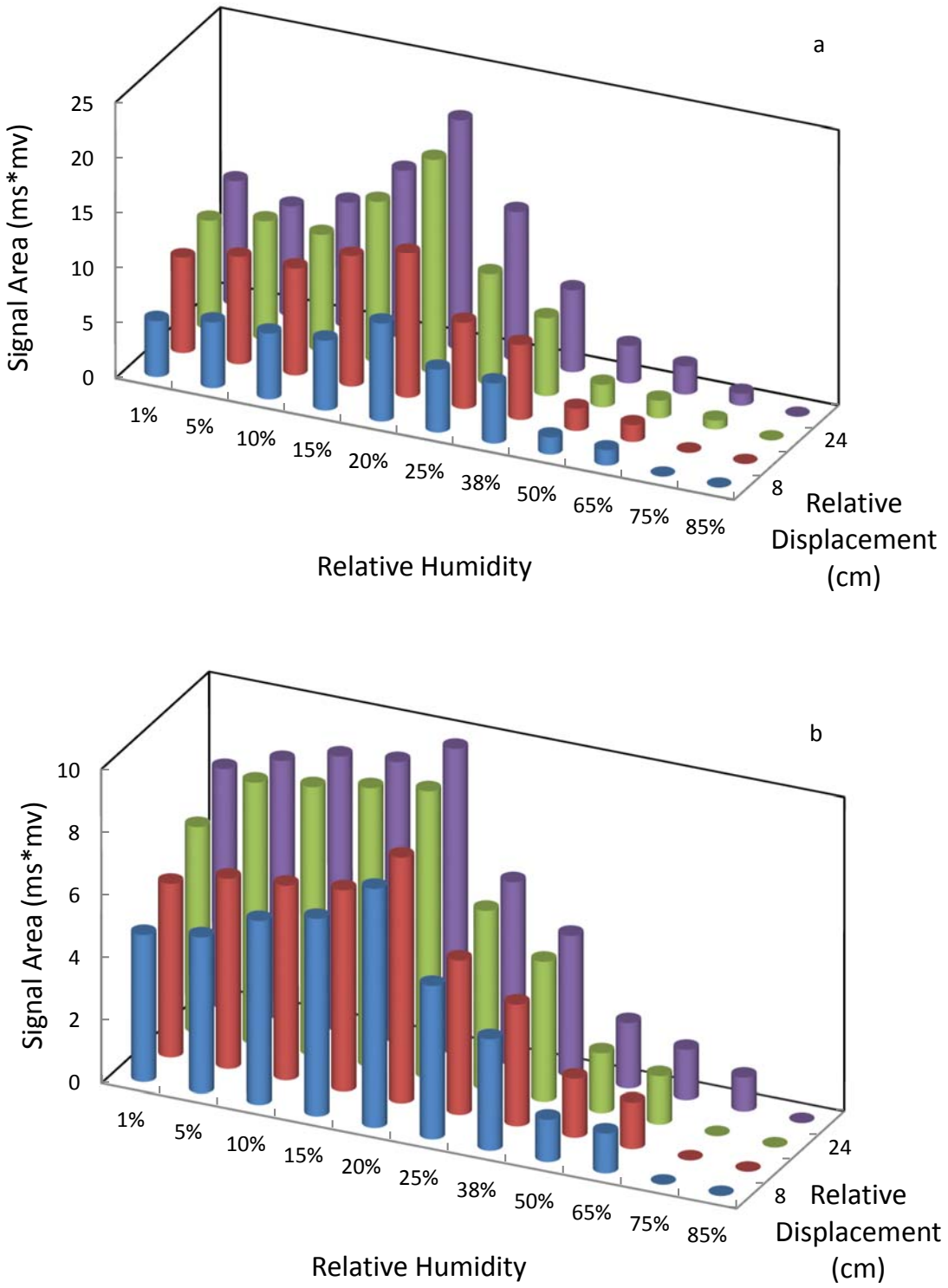

Figure 3.2. Effect of relative humidity and particle displacement on particle charge generated by rolling a ceramic ball on a copper plate at inclination angles of (a) 25 ° and (b) 40 °.

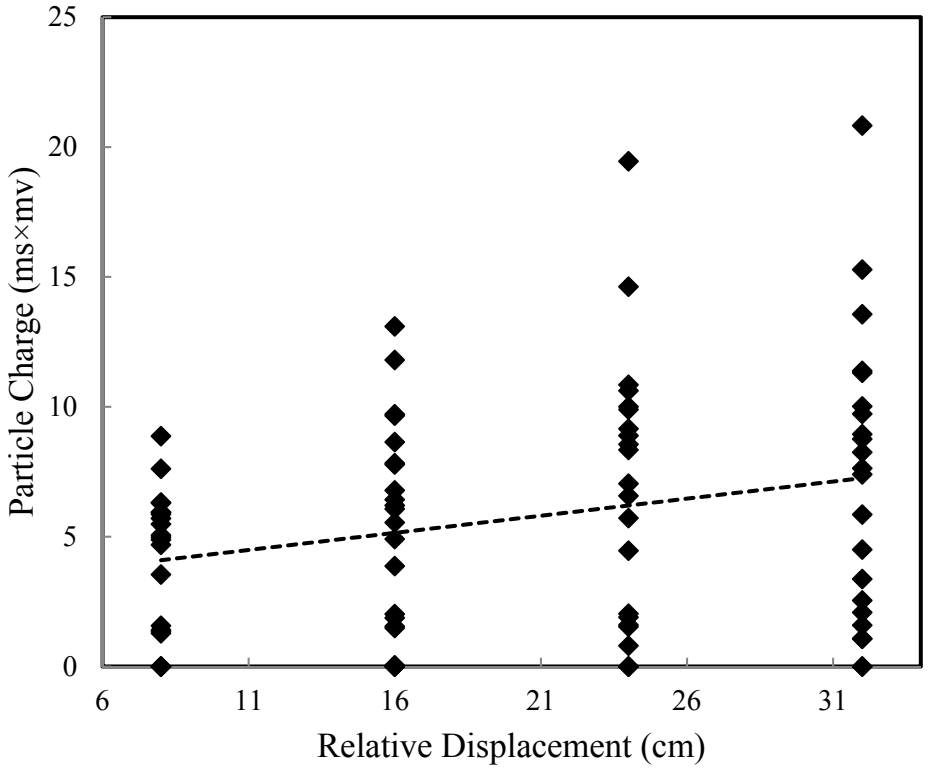

Figure 3.3. Experiment result of statistically correlation between particle surface charge and relative displacement.

The inclination angle of the copper plate controls the proportion of the particle gravitational force that is normal to the copper surface (F_n). As such, the frictional force between the ceramic cylinder and the copper plate, under the same frictional coefficient (α), during the tribocharging is a function of the copper plate inclination angle. A larger inclination angle (θ) provides smaller rolling frictional force as indicated by the following expression:

$$F_n = \alpha G_I cos\theta \tag{35}$$

The statistical relation between the ceramic cylinder surface charge and plate inclination is shown in Figure 3.4. Since a larger inclination provides a smaller normal interactive force, the total charge accumulated on the ceramic ball is significantly smaller. A similar finding was also reported in two previous publications (Poppe and Schrapler, 2005; Watanabe et al., 2007). It is clear that charge exchange efficiency can be promoted by a higher interactive effect at the contacting surfaces which can be achieved in a rolling action by decreasing the inclination of the copper plate.

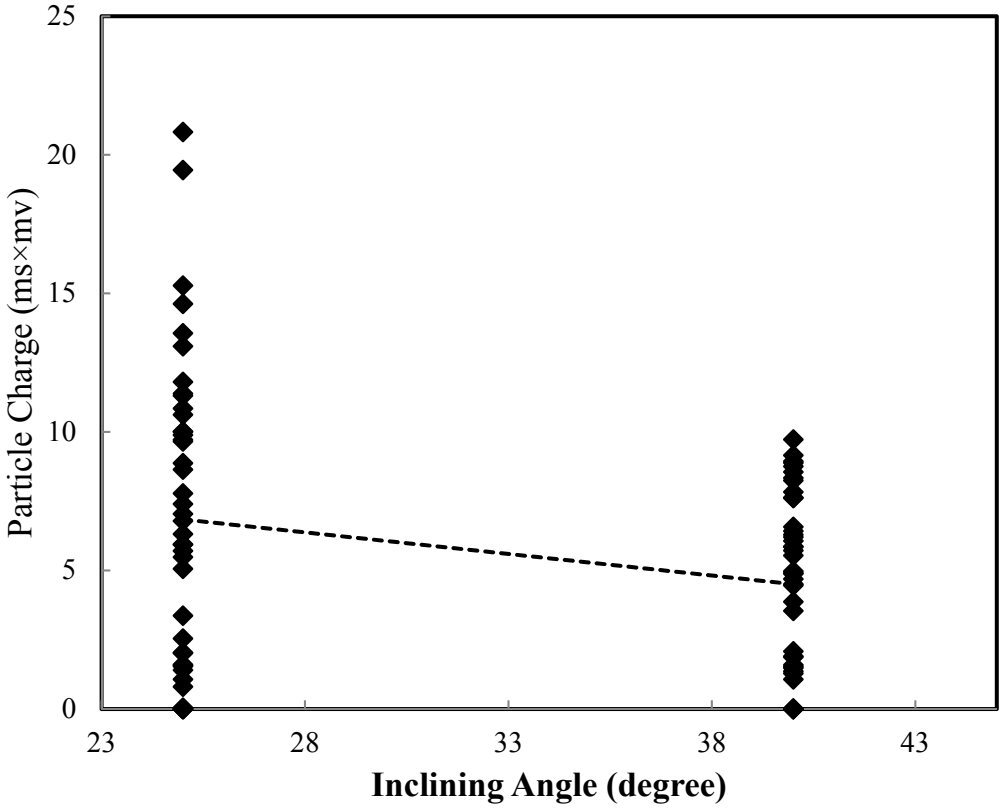

Figure 3.4. Statistical relation between the ceramic cylinder surface charge and the copper plate inclining angle.

As the experimental data indicates, humidity is another significant factor in influencing particle tribocharging efficiency. In this test series, a statistical correlation of the humidity influence on particle surface charge quantity was obtained as shown in Figure 3.5. Particle surface charge initially increased with the relative humidity level from a critical low value (1%) to maximum surface charge under a relative humidity in the range of 15-20%. This beneficial effect of high environmental humidity to the particle tribocharging efficiency is due to a thin layer of water film formed on the particle surface. The adsorbed water film provides several functions that affect particle tribocharging. On one hand, the adsorbed water may modify the particle surface electronic properties by activating the mobile charges on the surface and enhance the charge transfer rate (Pence et al., 1994; Wiles et al., 2004). On the other hand, the adsorbed water film may interrupt the discharge process, which can ultimately determine the particle final charge (Matsuyama and Yamamoto, 1997). Additionally, the thin water film and the moisture in the air improves the dielectric constant within the gap of the contacting surfaces, which enhances the capacitance generated by the contacting surfaces and resists the exchanged charge flowing back during the surfaces separation process (McCarty et al., 2007). A higher amount exchange charge can be stored on the surfaces when the relative humidity is elevated above the critical level. As such, a critical relative humidity value exists which maintains the exchanged charges. With a continued increase in relative humidity above the optimum level, particle surface charge quantity decreases due to the total quantity of water absorbed on the particle surface. The thickness of the water film at the surface increases surface conductivity which facilitates exchanged charge dissipation by discharge to the copper plate or the surrounding air (Bunker et al., 2007; Park et al.,

2008; McCarty et al., 2008). In this case, the total particle tribocharging efficiency is deteriorated. When the relative humidity is raised above 70%, the ceramic cylinder barely retained any charges after the tribocharging process. The critical relative humidity level for achieving the maximum particle tribocharging efficiency (i.e., the humidity level needed to obtain the maximum particle charge quantity) depends on the particle surface physical properties. The relative humidity effects obtained from the study agrees well with those reported by other researchers (Lungu, 2004; Schella et al., 2017).

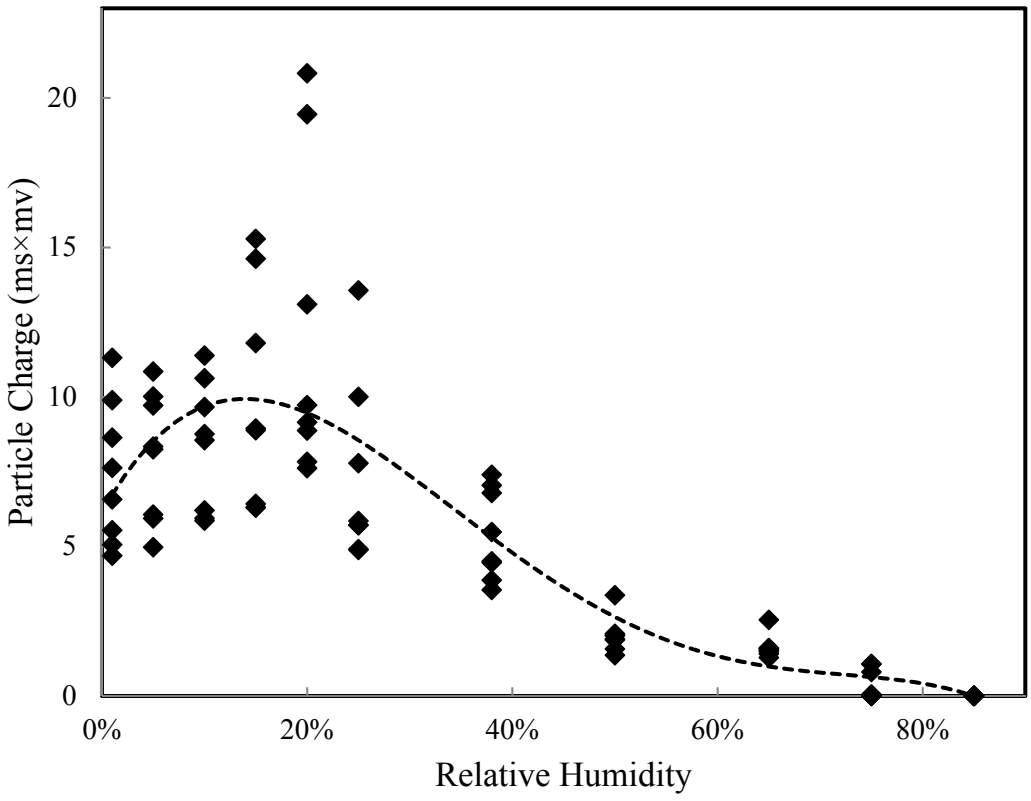

Figure 3.5. Statistical correlation between particle surface charge achieved under rolling action and relative humidity.

3.4. Comparison of tribocharging by rolling versus sliding actions

In this series of tests charging by rolling and sliding actions were compared using a copper plate inclined at 40 °. Humidity level and the particle displacement were controlled to evaluate the particle surface charge differences generated by the two contact actions. The exact contacting area is correlated with the elasticities of contacting objects (Ishigaki et al., 1979). For tribocharging by rolling action, the particle total surface area involved in the contact charging was about 708 mm^2 while the sliding contact area was about 6 mm^2, which was estimated based on a contact surface equal to a radial distance defined by 3 radial degrees. Because the same ceramic cylinder was used in the two series of test, the sliding resistance force is estimated to be about 200 times larger than the rolling resistance force. This ratio assumption is based on the correlation of rolling resistance coefficients and sliding resistance coefficients for rich variety of two hard material pairs. The detailed experimental results of obtained from tribocharging a ceramic cylinder by rolling and sliding on a copper plate are provided in Table 3.2. Relative displacement and humidity levels were controlled to assess and compare their influences on particle surface charge using the two surface contact methods.

The data in Table 3.2 was plotted to show a comparison of the rolling and sliding contact actions as shown in Figure 3.6 (a) and (b). Both relative displacement and humidity had a significant influence on the ceramic cylinder surface charge for both contacting types. The general influential patterns of their influences from both rolling and sliding tribocharging are similar. Since the copper inclined angles are identical for all tests, the difference of their influential patterns was due to the difference of total surface areas involved in the tribocharging and the different friction forces at the interface.

Table 3.2. Experiment of ceramic cylinder tribocharging with the copper plate with different tribocharging style under the inclined angle of 40 °.

Tribocharging Type		Tribocharging by Rolling				Tribocharging By Sliding			
Inclined Angle		40°							
		Signal Area, ms*mv							
Relative Displacement, cm		8	16	24	32	8	16	24	32
Relative Humidity	1%	4.688	5.542	6.573	7.629	4.871	5.568	6.363	7.545
	5%	4.975	6.066	8.337	8.250	6.685	8.066	8.403	8.802
	10%	5.863	6.205	8.555	8.757	7.799	9.162	9.270	9.402
	15%	6.292	6.425	8.885	8.941	8.568	9.571	9.956	10.351
	20%	7.615	7.831	9.152	9.727	6.556	7.394	8.587	9.147
	25%	4.881	4.910	5.718	5.851	5.815	5.984	6.514	6.734
	38%	3.542	3.868	4.457	4.504	3.609	3.945	4.986	5.672
	50%	1.358	1.872	1.899	2.079	1.775	2.318	2.340	2.487
	65%	1.282	1.481	1.534	1.590	1.329	2.159	2.438	2.642
	75%	0.000	0.000	0.000	1.068	0.000	0.702	0.878	1.341
	85%	0.000	0.000	0.000	0.000	0.000	0.000	0.000	0.000

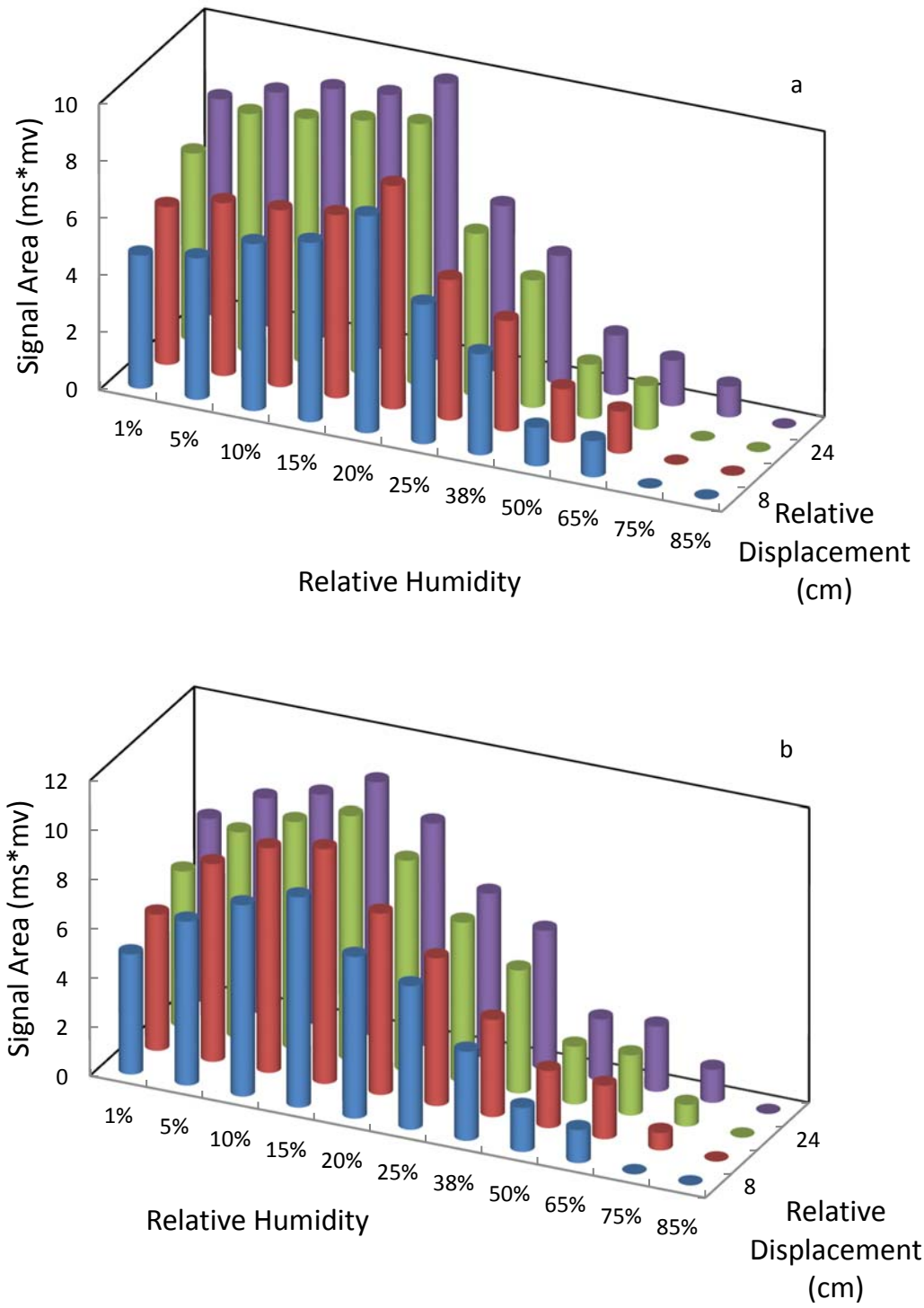

Figure 3.6. Particle surface charge quantity under different relative humidity levels and varying relative displacements after tribocharging with the copper plate (at 40 ° inclined angle) using contact methods involving: (a) rolling and (b) sliding.

Statistical plots were generated to assess the effects of relative displacements (Figure 3.7) and relative humidity (Figure 3.8). Particle surface charge was enhanced with an increase in relative displacement for both tribocharging modes. However, the slope of the trend line for the rolling tribocharging (about 0.073) was steeper than the sliding tribocharging (about 0.064). The ceramic surface provides limited density of available sites for charge exchange. As such, a larger surface area renders more positions for charge to transfer and lodge. Hence, a higher total capacity for charge exchange is realized using the rolling contact which ultimately provides continuous quicker charge accumulation with an increase in relative displacement (Mazumder et al., 1994). If the friction coefficients are assumed to remain constant during the tribocharging process and the surface property change caused by scraping can be ignored, the total sliding friction force is about 200 times larger than the rolling friction force. The experimental results show that the particle charge quantity provided sliding contact is larger than rolling contact under any identical operating conditions (humidity level and relative distance). The findings indicate that the tribocharging efficiency for using sliding tribocharging contact is higher than the rolling contact. This finding agrees well with those reported in previous publications (Bunker et al., 2007; Wu et al., 2013). As a result, the total surface area and tribocharging mode affects different aspects of the particle tribocharging process. In addition, the effect of the interactive force at the interface is more significant than the effect of total surface area involved in tribocharging process given that the sliding contact had higher particle charge with smaller tribocharging contacting surface area.

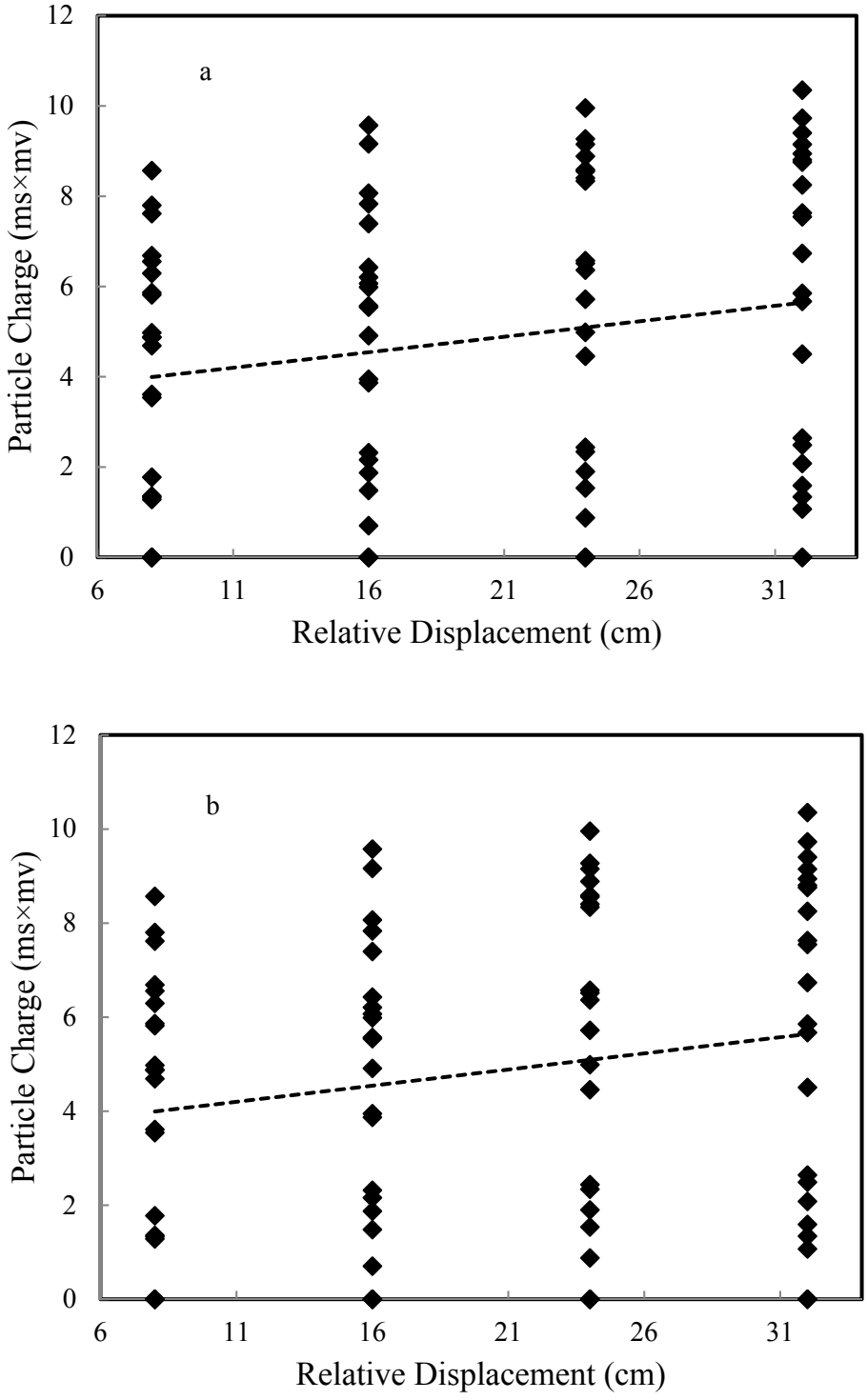

Figure 3.7. Statistical representation of the relative displacement influence on the ceramic cylinder (a) rolling tribocharging and (b) sliding tribocharging.

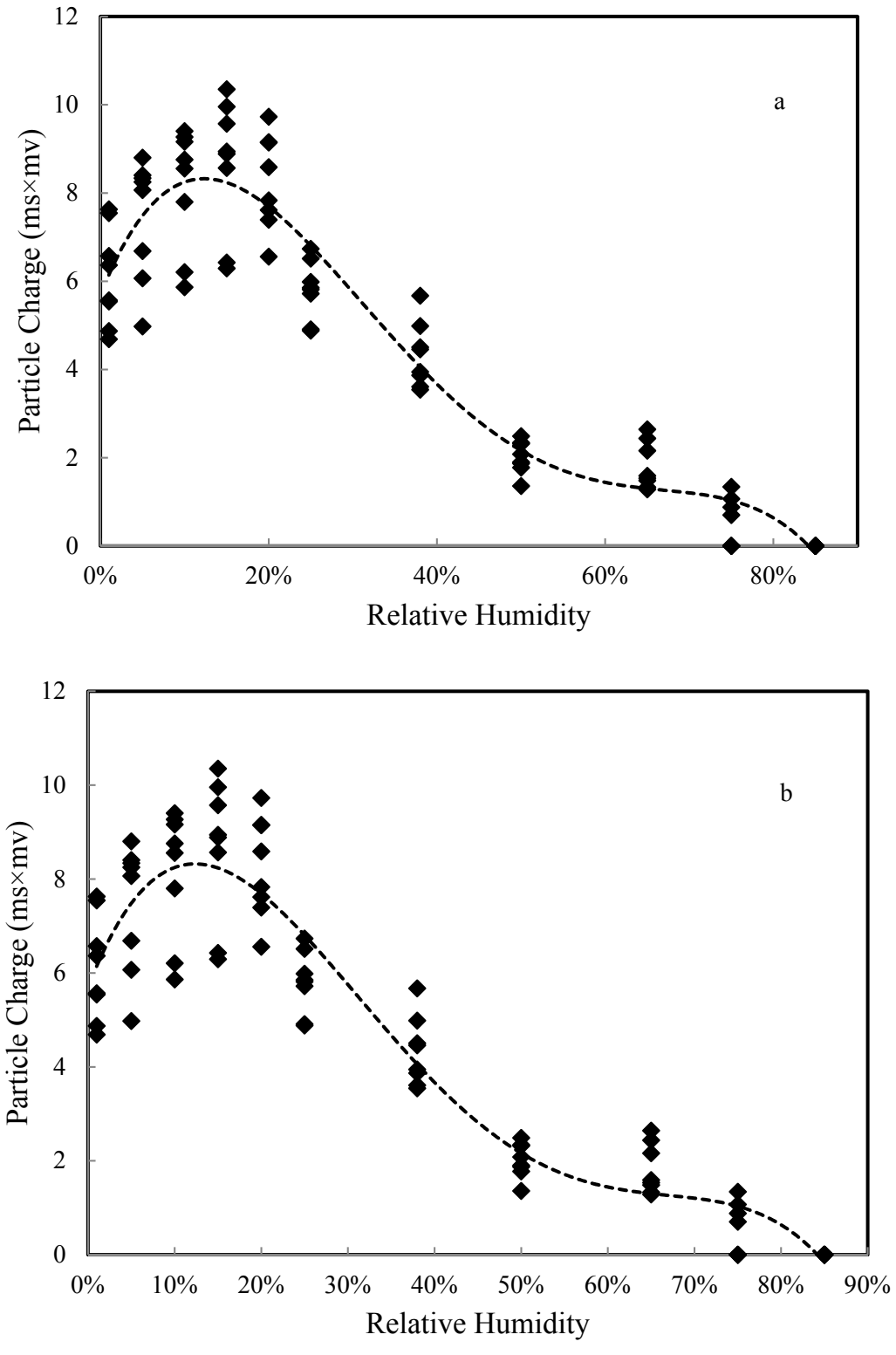

Figure 3.8. Statistical representation of the relative humidity influence on the ceramic cylinder (a) rolling tribocharging and (b) sliding tribocharging.

The relative humidity variation had a similar impact on the particle charge using both the rolling and sliding contact mechanisms. The experimental results shows that, when the relative humidity level rises from a value of zero, the ceramic cylinder surface charge increases until reaching a maximum charge at a given humidity value. This finding suggests that the presence of water molecules has a positive effect on the charge transfer efficiency. The particle surface charge quantity, reflecting the particle tribocharging efficiency, reaches the maximum at a relative humidity of 20% when contacting the surfaces by rolling action. The maximum particle charge achieved when sliding the ceramic cylinder on the copper plate was obtained at 15% humidity. Tribocharging by sliding facilitates the ceramic cylinder reaching charge saturation. Combining the fact that the peak charge quantities of sliding tribocharging are larger than the ones of rolling tribocharging under all respective relative displacements, the findings support that the sliding tribocharging is realized quicker and the ultimate particle charge is higher than rolling tribocharging.

However, the negative effect of the water coverage on the contacting surfaces is deemed to have more severe negative effect on both types of tribocharging when humidity values are above a critical value. The surface charge drops dramatically with the increasing humidity levels beyond the critical humidity level. This finding provides further evidence that the formation of a thick water film on the ceramic cylinder surface escalates the discharge process. As a result, the total charge quantity drop in the high humidity region is larger than the total charge quantity accumulation in the low humidity region. As a result, for the ceramic cylinder tribocharging, the environmental humidity level needs to be controlled to maintain the humidity value at or near the optimum level.

3.5. Coal chunk and silica chunk sliding tribocharging with 40°inclined copper plate under different relative humidity level

Silica is a major contaminant mineral in coal. The surface electronic properties of the coal component and the silica are significantly different which provides the potential to apply electrostatic separation for coal beneficiation. Since the published measured work functions for coal, silica and copper are 5.42 eV, 4.6 eV and 5.11 eV respectively, the coal is charged negatively while the silica is charged positively after contact charging with the copper plate. In a series of tests, coal and silica were studied based on their material surface electronic property differences with a focus on optimizing the process for fine coal cleaning A coal chunk measuring868 mm^2 and weighing15 g and a silica chunk having a cross-sectional area of 135 mm^2 and weighing 7 g with high purities were used to study the contact charge against a copper plate inclined angle of 40 ° under various controlled humidity levels. The surfaces of the two chunks were polished using an 800 mesh polishing wheel to ensure nearly equal surfaces roughness. The cumulative area under the last pulsing signals recorded by the oscilloscope was used to measure the particle charge quantity, which is shown in Table 3.3. Figure 3.9 shows the particle charge distributions of the coal and silica chunks after contact charging with the copper plate over a range of relative displacement and humidity values.

Table 3.3. Experiment result of coal chunk and silica chunk contact charge with the copper plate.

Sliding Tribocharging with copper plate inclining at 40°									
Material		Coal Chunk				Silica Chunk			
Relative Displacement, cm		8	16	24	32	8	16	24	32
Relative Humidity	1%	-4.693	-5.379	-6.284	-6.875	31.628	38.047	47.009	50.324
	5%	-4.833	-7.699	-7.750	-9.905	33.357	39.217	49.491	53.885
	10%	-9.378	-10.136	-10.226	-10.876	33.859	40.796	49.629	53.764
	15%	-7.507	-10.016	-10.209	-11.869	34.538	41.430	51.525	59.572
	20%	-6.512	-8.291	-9.500	-10.526	29.661	36.674	42.100	44.994
	25%	-6.449	-6.926	-8.355	-8.596	25.906	34.638	41.165	43.987
	38%	-2.967	-3.022	-4.580	-4.953	22.154	25.803	32.567	33.741
	50%	-2.045	-2.198	-2.650	-2.729	14.248	16.819	17.604	18.070
	65%	0.000	0.000	-1.508	-1.818	1.800	2.385	3.656	4.625
	75%	0.000	0.000	0.000	0.000	0.000	1.798	1.993	2.131
	85%	0.000	0.000	0.000	0.000	0.000	0.000	0.000	0.000

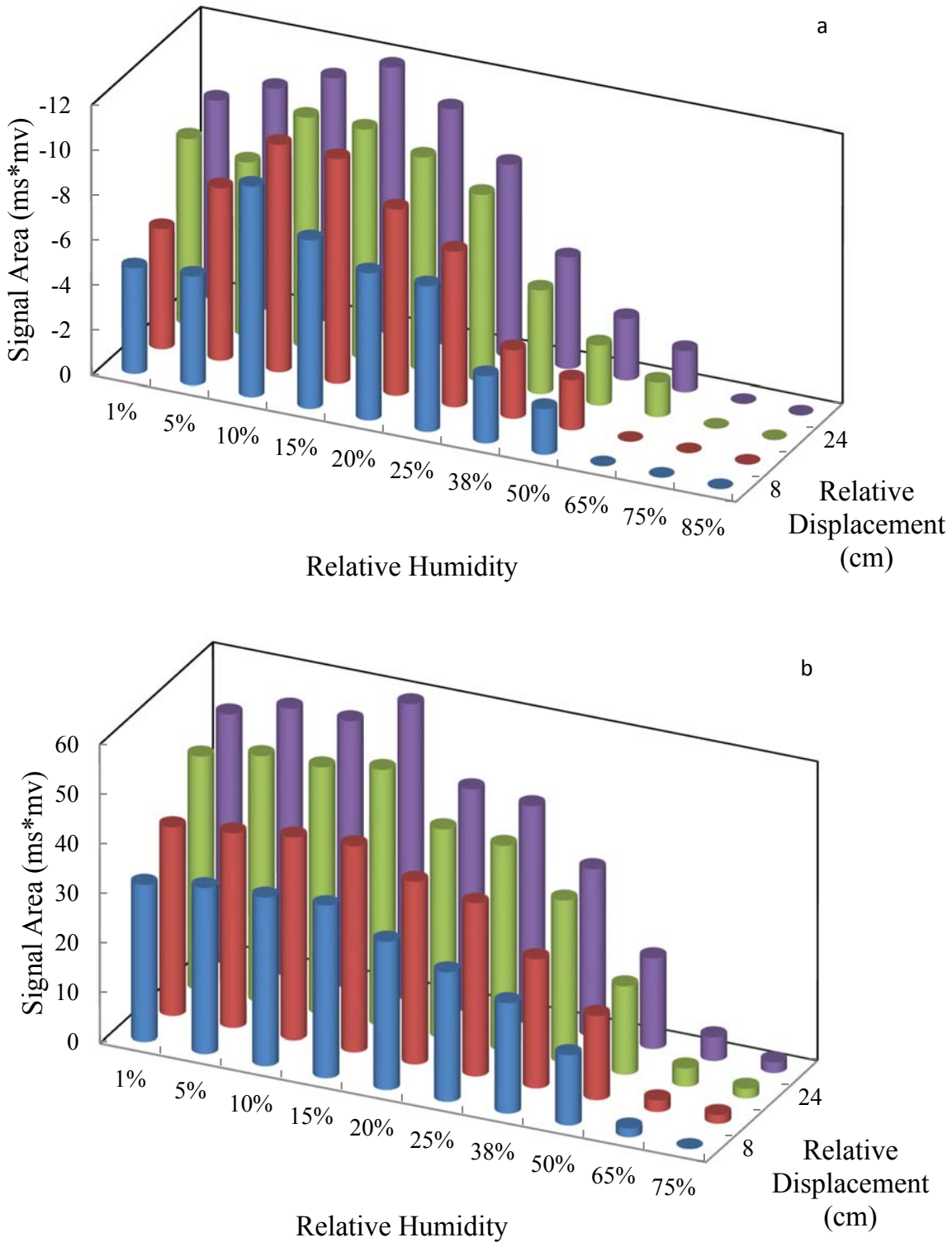

Figure 3.9. Particle charge distribution with different relative displacement under controlled ambient relative humidity level of (a) coal chunk sliding tribocharging and (b) silica chunk sliding tribocharging.

Though the coal chunk total surface area and mass are both larger than the silica chunk, the total charge quantity of silica is obviously larger than the coal under almost all the experiment conditions. The finding indicates that the silica has much higher tribocharging efficiency than the coal. The coal is charged negatively and the silica is charged positively after tribocharging with the copper plate, which is in accordance with their relative work function values. However, the charge quantity is not linearly proportional to their work function differences (ΔW). It specifies the work functions of materials can accurately predict the electron transfer direction, but they are not good indicators for charge quantity prediction. Because the relative charge transfer quantity is not closely correlated much with the work functions values, the surface site available for charge transfer and charge retention should be more correlated with particle charge. The statistical correlations of particle charges to materials are shown in Figure 3.10. As indicated by larger deviations in the silica charge distribution relative to coal, the influences of the relative displacement and the relative humidity on silica tribocharging is more significant. The reason should lie in the more surface chargeable sites of silica, which are easier to be activated or deactivated by the variations in operating conditions.

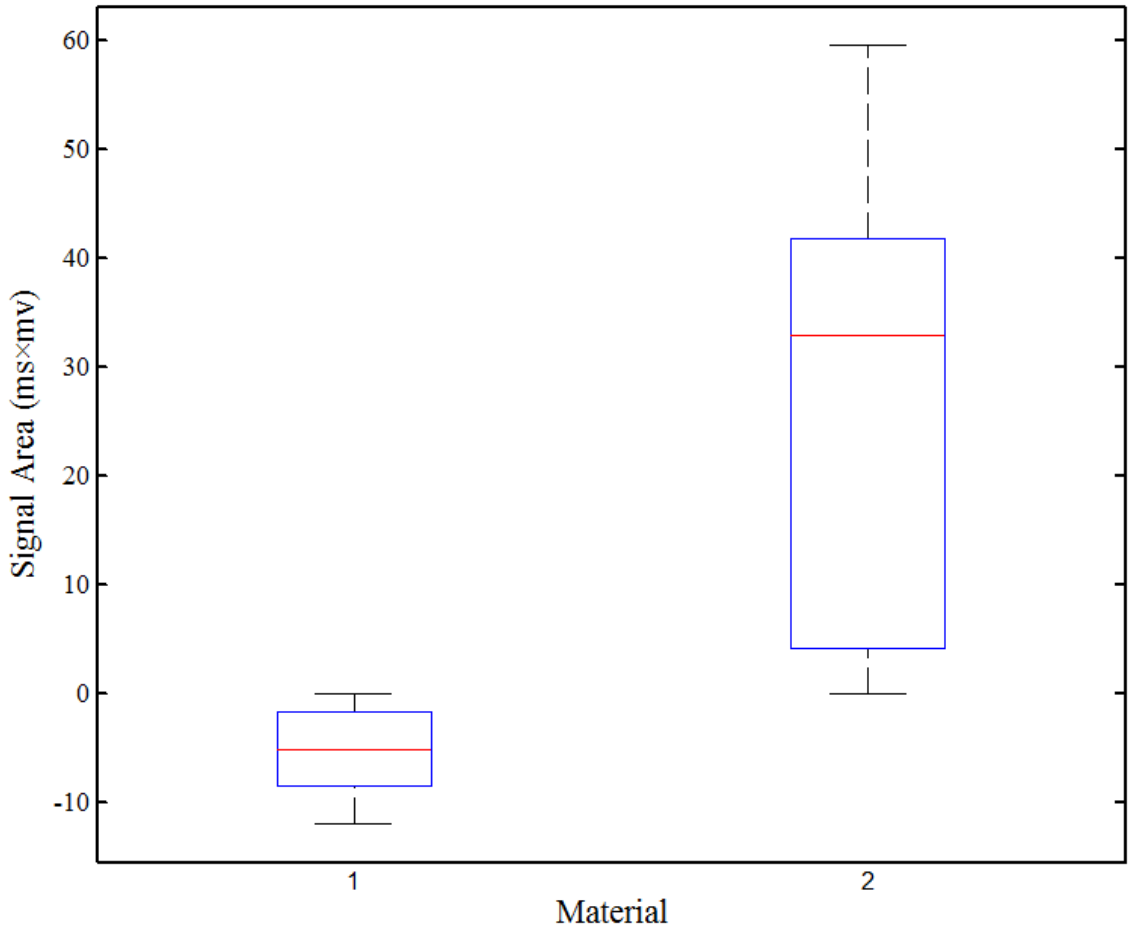

Figure 3.10. Statistical representation of particle charge quantity for coal chunk (1) and silica chunk (2) contact charge with the copper plate.

The relative humidity influences on the coal and silica tribocharging are similar, as shown in Figure 3.11. At the low humidity region, the charge quantities of the coal and silica both increase with humidity level. The adsorbed water islands or thin water film on the solid surfaces may create a bridging effect that enhances the charge transfer efficiency (Law et al., 1998). The statistical result of the humidity influence shows the coal chunk has the maximum charge at the relative humidity of 10%, while the silica the maximum charge at 15% relative humidity. In addition, the *t* test on the humidity influence on the coal and silica tribocharging shows that the humidity level is a significant factor for both materials. However, the coal material is more sensitive to the humidity level. At high humidity values, a thick water film at the solid surface facilitates charge relaxation or even blocks the charge transfer which a significant decrease in particle surface charges. This negative effect is more significant on the silica surface upon contact through sliding tribocharging since its charge quantity drops much quicker with the increasing relative humidity level. As such, the humidity level should be controlled around 15% to best activate the material surface sites for tribocharging.

The relative displacement positively relates the surface charge of the coal and silica as shown in Figure 3.12. The solid charge quantity increases much faster than the coal, which is reflected from the slopes of the trend lines. Statistical correlation between the chunk charge quantity and the relative displacement shows the coal has an average charge increase rate of 0.099 ms*mv/cm, while the silica chunk has average increasing rate of 0.537 ms*mv/cm. Because the surface roughness of the coal and silica chunks was similar and coal has more mass, the energy consumption rate of the coal chunk is higher than the silica chunk when sliding on the same copper plate. The experiment results prove that the silica surface has more sites available, compared with coal, for charge exchange, which are easier to be activated by the increasing energy consumption at the interface. The surface sites available for charge exchange under natural atmosphere environment could be expressed in terms of material surface electronic properties proposed by Ireland in 2012. The energy consumption at the interface is considered as a factor influencing the surface site density:

$$\frac{1}{2}\frac{\sigma_s^2}{\kappa} = \frac{1}{2}\frac{\sigma_0^2}{\kappa} + \eta\frac{W}{A} \tag{36}$$

where σ_0 is the saturated surface charge density during static contact, A the interface area, σ_s the dynamic saturation charge density, W the work done by sliding friction at the interface, κ the energy density for static contact.

Based on the sliding tribocharging test experiment result using the coal and the silica, the surface chargeable site densities of the two materials can be estimated. Since the contacting surfaces were polished by 800 polishing wheel, the sliding friction coefficients for coal and silica were considered similar. Thus assume that the energy consumed is proportional to the chunk mass. Assign $\eta = \frac{1}{2}$, which means half of the total consumed energy is used to increasing the dynamic saturation charge density. Considering all the chargeable sites were activated under the optimum operating conditions for both the materials, taking the total surface areas of coal chunk and silica chunk into account, the relationship of the maximum available surface sites for charge transfer between coal (σ_{coal}) and silica (σ_{silica}) under static status is estimated to be:

$$\frac{\sigma_{silica}}{\sigma_{coal}} = \sqrt{\frac{\sigma_s^2 - \frac{{W_s}^2}{{A_s}^2}}{\sigma_c^2 - \frac{{W_c}^2}{{A_c}^2}}} \approx \sqrt{\frac{(\frac{6.232}{0.135})^2 - \left(\frac{6.054}{135}\right)^2}{(\frac{0.58}{0.868})^2 - \left(\frac{12.97}{868}\right)^2}} = 69 \tag{37}$$

The available surface site density for tribocharging ratio shows that silica surface has much higher surface site density available for tribocharging. Starting from this result, in a coal and silica composite particle, even there is a small portion of the concomitant silica mineral exposed on the coal particle surface, it could significantly impact the total surface charge of this particle. These fundamental provides the theoretical support for the triboelectrostatic beneficiation of silica bearing coal.

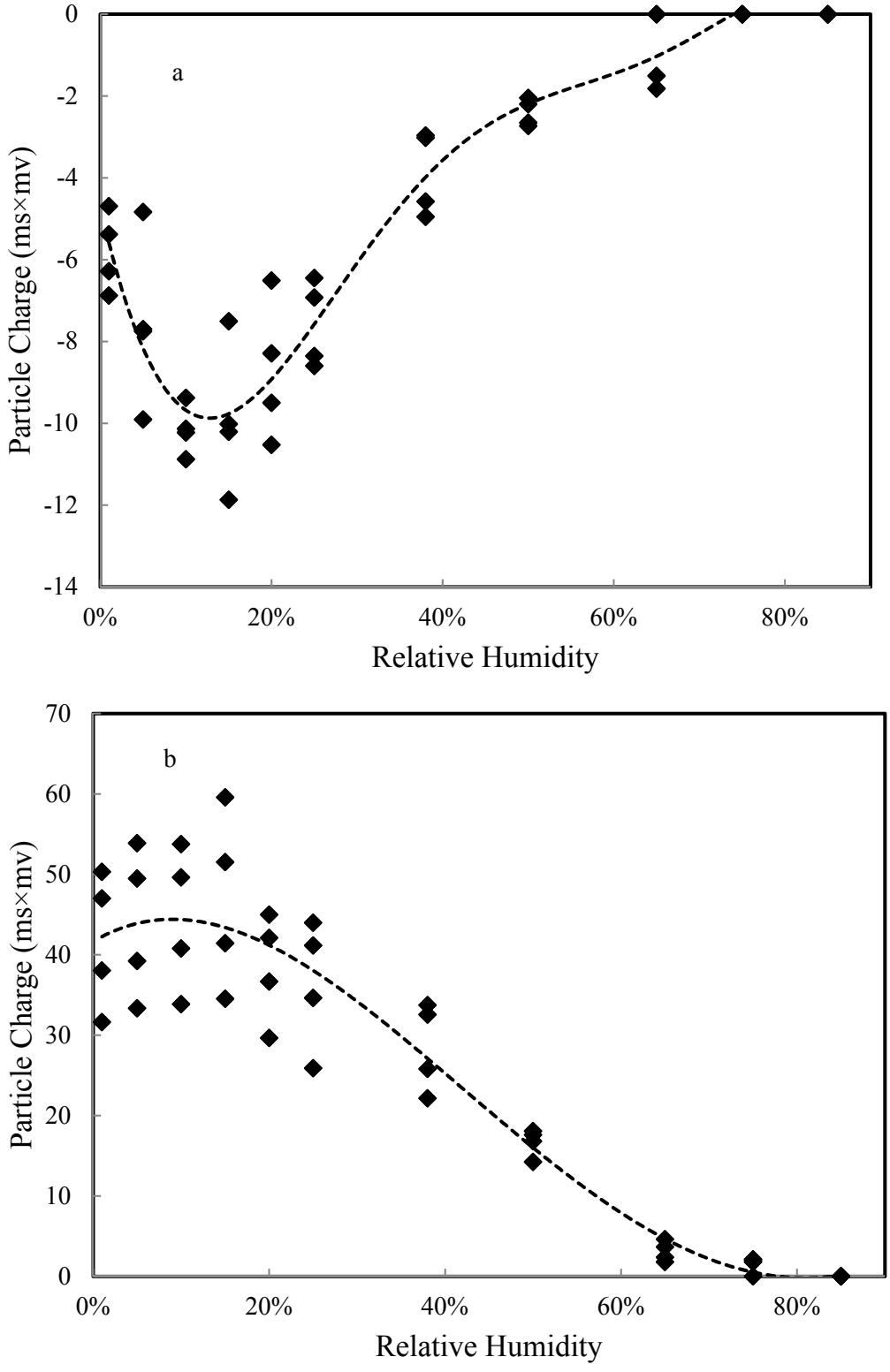

Figure 3.11. Statistical of the humidity influence on (a) coal chunk and (2) silica chunk sliding tribocharging.

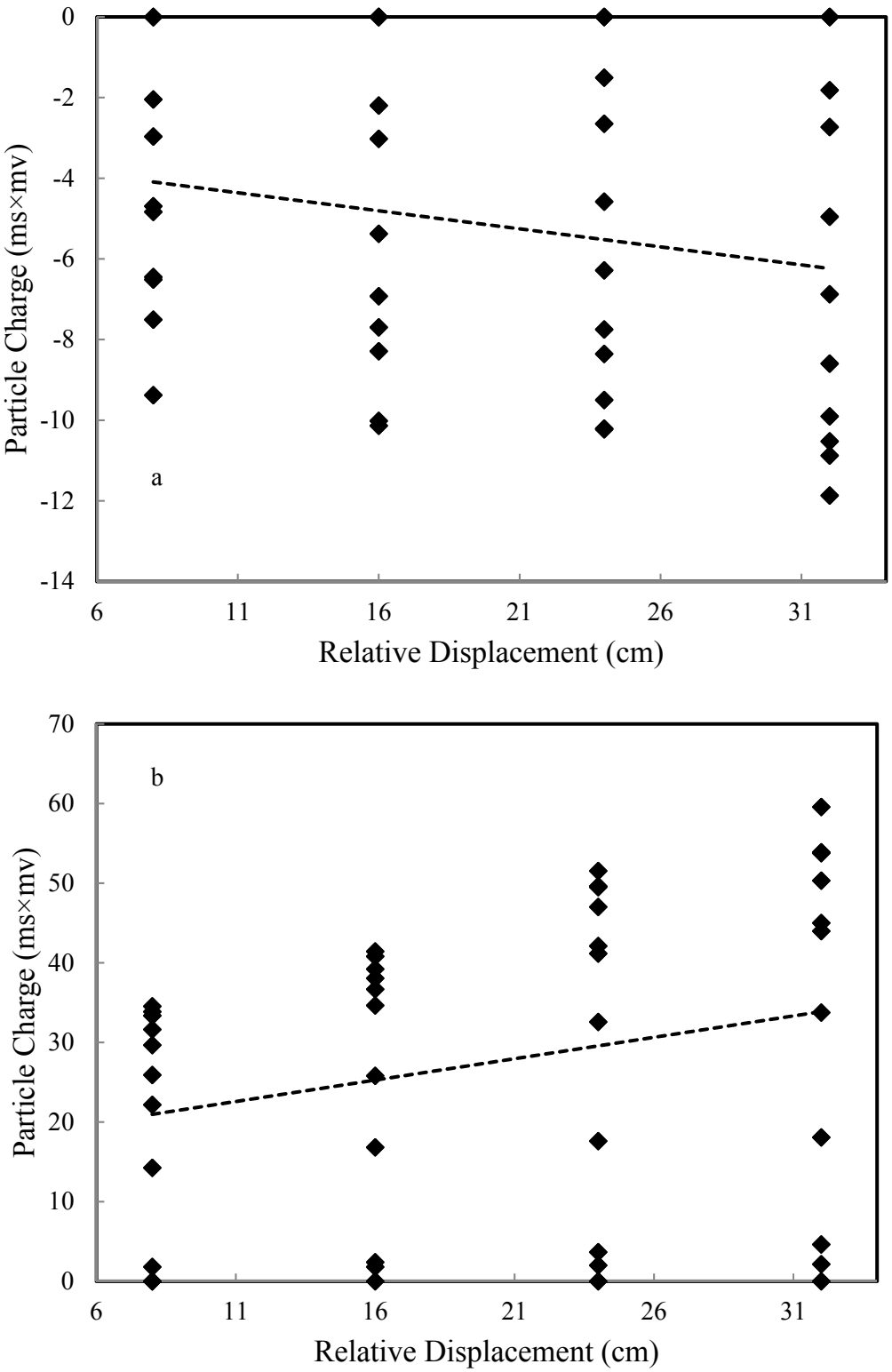

Figure 3.12. Statistical representation of the relative displacement influence on (a) coal chunk and (b) silica chunk sliding tribocharging.

3.6. Theoretical Model Speculation

To implement the particle tribocharging theory utilizing the new findings, the starting point was the basic assumption of this study, i.e., the condenser model. Since the electron is the only charge media considered in the whole study, the theory involved in the condenser model is used as the foundation. Next, the discoveries and conclusions from this study based on the ceramic cylinder-copper plate tribocharging are used to supplement the basic theoretic model, which is managed to evolve into a semi-empirical model. The general equation derived from the theory of the condenser model for the particle tribocharging process is (Matsuyama and Yamamoto, 1995; 1997):

$$q = \frac{\pi \varepsilon_0 V_e D_p^2}{2d} \tag{38}$$

The particle tribocharging efficiency has been discovered that not only controlled by the physical properties of the contacting surfaces, but also influenced by the outside factors (Matsusaka et al., 2010; Buda et al., 2013). The particle surface electronic property is correlated with the surface sites density (ρ_i) available for charging and the capacity to retain charges. Additionally, the environmental condition (relative humidity level, h_i) and the interactive force (f_i) during the charging event correlate well to the particle tribocharging efficiency ($f(E)$). The relative displacement (l_i) and the total surface area (A_i) are related to the probability ($P(E)$) or the proportion of the available charging sites on the surface that involved in tribocharging. Since the influences of the factors on the particle tribocharging are not linear, the modified equation for the particle charge is expressed as:

$$q_i = \frac{\pi \varepsilon_0 V_{ij} D_i^2 \rho_i}{2d} f(E) P(A_i) = \frac{\pi \varepsilon_0 V_{ij} D_i^2 f_i(h) f_i(f_n) f_i(f_f) f_i(l)}{2d} P(S_i) \tag{39}$$

$$S_i = A_i \rho_i \tag{40}$$

where $f_i(h), f_i(f_n), f_i(f_f)$ and $f_i(l)$ are the functions corresponding to the effects of relative humidity, normal force, friction force, and relative displacement respectively that need to be determined from the specific set of experiment data for the derivation of semi-empirical expression. The $P(S_i)$ is a probability distribution function of the charged sites related to the total charging sites involved in the tribocharging process. This probability distribution is integrated with the particle physical property and the operating conditions.

The exact expression for each function could vary according to the changes of the material pairs involved in the tribocharging process. If the physical property and the surface electronic properties are different, their sensitivity to the operating factors and the ambient environmental conditions will change. In this study the ceramic-copper was used as the standard material in the tribocharging process dynamic study, hence the derivation process for the functions that reconciles the particle final charge is conducted based on the ceramic-copper tribocharging result. It can be easily expand to other pairs of materials using similar procedure.

To improve the function evaluation accuracy and seek the intrinsic idiosyncrasies of the functions reconciled to the basic theoretical tribocharging expression, it is necessary to avoid the introduction of additional assumptions and estimated values related to the theoretical components that are not treated as independent variables to calculate the absolute particle charge. One method used here was to resort to isolate the relative charge density changes caused by the functions alone, with the assumption that those influential functions are power functions. The merit of the application of power functions is that it can effectively eliminate all the other uncorrelated constant effects when calculating relative charge variation. The effect of the target function was

isolated and fitted with the charge variation. After determine the effect of every function on the particle surface charge change for a whole set of experiments, the least square method is adopted to regress the power function that best fit the surface charge variation. The relative displacement influential function was pursued first as an example.

When the relative contact distance is i and j, their influence in the particle tribocharging can be expressed below as:

$$\frac{q_i}{q_j} = \frac{f(l_i)}{f(l_j)} \tag{41}$$

Assume the function is exponential (l^{α}), the above equation equals:

$$\frac{q_i}{q_j} = (l_i/l_j)^{\alpha} \tag{42}$$

Next, the charge density ratios were calculated according to the relative displacement differences for the whole set of date. Those charge ratio changes are considered to be solely affected by the relative displacement variation. Apply the least square method to regress the power equation based on the calculated charge ratios, and the best fit α is 0.3903.

$$f_i(l) = l^{0.3903} \tag{43}$$

Apply this procedure to solve other functions. The other functions can be described as:

$$\begin{cases} f_i(f_n) = f_n^{\beta} \\ f_i(f_f) = f_f^{\mu} \\ f_i(h) = h^{\gamma} \end{cases} \tag{44}$$

By applying the same method described previously, the interactive force regression was derived as:

$$f_i(f_n) = f_n^{4.6405} \tag{45}$$

The friction force quantity at the interface regressive function can be described by:

$$f_i(f_f) = f_f^{0.0283} \tag{46}$$

Since the relative humidity had dual effects on particle tribocharging, the humidity regression result is:

$$\begin{cases} h^{0.1182} & h \leq 15\% \\ h^{-1.653} & h > 15\% \end{cases} \tag{47}$$

The function of the surface is a probability distribution function. It explains the proportion of the available surface sites for tribocharging and charge retention after the tribocharging process. Actually the surface tribocharging efficiency is generally realized by combining the surface charge capacity and the charging probability distribution. It is influenced by both the material surface electronic properties and such operating factors as the environmental humidity, normal force, and friction force. Due to the complexity of the charging efficiency function, it cannot be solely quantified by the simple theoretical particle tribocharging expressions. The quantification of the probability of the tribocharging efficient distribution function needs to be integrated with the material pairs and the operating conditions for total particle charging efficiency calculation.

The procedures for estimating the probability distribution of the particle tribocharging efficiency use the scenario analysis base on the specific experiment conditions.

$$P(S_i) = \begin{cases} 0-25\%, & \omega_1 \\ 25-50\%, & \omega_2 \\ 50-75\%, & \omega_3 \\ 75-100\%, & \omega_4 \end{cases} \tag{48}$$

The probability distribution of tribocharging efficiency has the constrain of $\sum \omega_i = 1$. The segment of the probability distribution can be further expanded if it is necessary. Since it is an experimental specific function, it can be practically evaluated through experiment methods combining the charge measurement and charge quantity distribution simulation method. When the particle charge distribution is derived, the probability of tribocharging efficiency distribution function can be derived. This part will be explained in detail and applied in a subsequent case study using above described procedure. Combining the theoretic compression model and the regression analysis results based on the parametric study, the new semi-empirical mathematical expression of the particle tribocharging is developed below:

$$q_i = \begin{cases} \dfrac{\pi\varepsilon_0 V_{ij} D_i^2 \rho_i P(S_i) l^{0.3903} f_n^{4.6405} f_f^{0.0283} h^{0.1182}}{2d}, & h \le 15\% \\ \dfrac{\pi\varepsilon_0 V_{ij} D_i^2 \rho_i P(S_i) l^{0.3903} f_n^{4.6405} f_f^{0.0283}}{2dh^{1.653}}, & h > 15\% \end{cases} \tag{49}$$

3.7. Summary

In this study, particle tribocharging was studied in a controlled environmental chamber under specific operating conditions. Several operating parameters were investigated to quantify their influence on the particle tribocharging process. A pulsing signal recorded by an oscilloscope was used for charge quantification.

Particle charge was found to cumulate with continued contact as indicated by the consistent charge increases that were recorded as the overall length and time of contact (i.e., relative displacement and copper plate inclination were controlling factors) was extended with a copper plate. This trend was consistently obtained for a ceramic cylinder and chunk specimens of coal and silica. The amount and rate of charge accumulation as well as polarity varied for the three materials. Polarity was predictable based on work functions of the particle types and copper plate. However, the total particle charge and rate of accumulation did not correlate well with the relative differences between the work function.

Varying the plate inclination and studying two different contacting actions (i.e., roller and sliding contacts) provided an assessment of the role played by the normal interactive and friction forces. Both forces were found to be positively correlated with the particle final charge. It indicates the energy consumption at the interface favors the electron transfer process.

The total charge generated on a particle as a result of rolling or sliding contact with a copper plate was found to be maximized at a given level of humidity that was dependent on particle type. Maximum particle charges were general achieved under relative humidity values in the range of 15% to 20%. The humidity level has dual effects on the particle charge. When the relative humidity was low, the increasing humidity leads to the adsorption of water molecules on the particle surface and formation of a thin water film. The thin water layer facilitates the charge exchange process and resists the leakage of the exchanged charges. However, with the continuing increase of the relative humidity beyond a critical value, the water film thickness accumulates thereby elevating surface. The presence of an excessive amount of water prompts dissipation and leakage of the exchanged charges. As such, particle charge was negatively correlated with high relative humidity values.

Particle surface charging was examined using purified specimens of coal and silica. The experimental result showed that their surface sites differently to the tribocharging process which explains why effective separations and coal upgrading can be achieved. The magnitudes of the parametric effects were also different although the correlations with particle charge followed a similar trend. Silica was found to have much higher tribocharging efficiency than the coal. The silica surface chargeable sites were estimated to be about 69 times more than the coal surface, which provides a theoretical basis for the triboelectrostatic beneficiation of silica rich coal. Additionally, the surface chargeable sites on the silica surface were easier to be activated or deactivated by the operating parameters.

A semi-empirical model was developed from the basic compression model utilizing basic assumptions and the regressions obtained from the experiment results of the parametric studies. The factors of relative displacement, relative humidity, normal force, and the friction force were incorporated into the original theoretical expression that resulted in a semi empirical model for particle tribocharging. It provides a more accurate alternative to predict particle surface charge corresponding to actual operating conditions. The particle tribocharging efficiency distribution is strongly related to the material electronic properties and the experimental specifics. It can be evaluated after analyzing the particle charging experiment data under specific tribocharging

conditions and materials. In a subsequent study, the particle charge distribution were studied in detail and applied in research cases.

4. Particle size effect in RTS particle tribocharging and separation processes

4.1. Introduction

Particle size is a basic physical property of a material that has a critical influence on the separation performance of most unit operations and the triboelectric process is no different. For particle charging, an important fact is that particle size is inversely correlated with particle surface area and the number of chargeable sites. The available sites on the particle surface are the basis for particle exchange (Mazumder et al., 1994). Additionally, the particle size is proportional to the particle mass, which impacts the particle charge density and its movement under specific hydrodynamic environments during separation. As such, the particle size is a critical factor in controlling the particle tribocharging and hence the particle separation process.

Previous particle tribocharging tests discovered that increasing the interactive force between contacting surfaces could benefit the charge transfer. However, the exact effect of the interactive force on particle tribocharging efficiency varies significantly due to the material pairs and exact operating conditions existing during the tribocharging process. Previous researchers have claimed that particle size has a correlation with the particle surface electronic property, which could be more significant in affecting particle tribocharging (Trigwell et al., 2003; Mukherjee et al., 2016). In the particle separation process, different designed electrostatic separators have various methods in tackling the charged particle separation issue (Iuga et al., 2001; Wu et al., 2008; Tilmatine et al., 2009). However, the turbulent air condition that exists inside the separation process is often ignored. In fact the separation environment can be a key component in achieving effective particle separation as it is impossible to achieve good separation without strict and accurate control of the separation process. As a result, the particle charging and the particle separation sub-processes need to be considered as an integral system to comprehensively understand the corresponding electrostatic separation.

In this study, a coal sample having a particle size below 0.3 mm was screened into different particle size fractions and then fed material independently into the rotary triboelectrostatic separator (RTS) beneficiation process to investigate the particle size effect. A particle tribocharging experiment methodology was adopted to determine the particle charge density distribution after the RTS separation. Utilizing the experimental data, a mathematical model was employed to assist in understanding the effects on particle tribocharging and quantify the particle tribocharging efficiency distribution. In the particle separation process, the dynamic ambient air applies a drag force on the falling particles with varying effects caused by the inhomogeneous particle size. Fundamental mathematical calculations were used to quantify the influence of flowing air velocity on the particle separation. Relationships describing the particle size impacts on the particle tribocharging and the separation sub-process were integrated together to derive the overall influence on the RTS separation efficiency.

4.2. The RTS particle tribocharging test based on different sizes feed coal

In the present study, a representative coal sample collected from the product stream of an operating mine was crushed to a top particle size of 0.3 mm. The ash content of the sample was 25.34%. The crushed coal was sieved into four size fractions (0.3-0.21 mm, 0.21-0.105 mm, 0.105-0.063 mm and -0.063 mm). The material collected in each particle size fraction was fed independently to the RTS unit to study the influence of particle size. A two-stage statistical design method was used to determine the optimum operating conditions for the composite coal RTS beneficiation (detailed procedure was described in Section 6). The identical operating operation condition producing the highest quality concentrate from the composite coal was used for all the tests. The RTS tribocharging efficiency distribution was studied by utilizing the results from both the experiments and the mathematical simulations. The RTS with three modified Faraday cages inserted below the separation chamber was used for direct particle collection and product charge measurement after the RTS separation. The configuration of the equipment is shown in Figure 4.1. The rotary charger had an octagon shape with a surface covered with pure copper (>99.9%). The experiment procedure involved the following steps:

(1) Store the feed material in a drying oven overnight before the test to reduce the coal surface moisture content to below 2% by weight.
(2) Check all components of the RTS to ensure that the unit is working properly. Make sure that the RTS is insulated and no short circuit exists inside the system.
(3) Turn on the vacuum system to initiate air flow through the unit. Measure the volumetric airflow rate in the three product streams. Adjust the air valve to ensure that the volumetric flow rates are equal.
(4) Adjust the operating conditions to the optimum conditions for the composite raw coal which include a solids feed rate of 20 kg/h, charger rotation speed of 4000 rpm, applied charger voltage of -5 kV, injection air rate of 1.9 m/s. The voltage supplied to the separation chamber is +25 kV.
(5) Maintain the same operating condition settings to treat all coal samples.
(6) Place the feed coal sample inside the vibrating feeder.
(7) Ground the Faraday cages to drain the static charges, Then, disconnect the grounding.
(8) Turn on the experiment system except the vibrating feeder. After ensuring that the system is working normally (after 30 seconds), turn on the vibrating feeder.
(9) After all particles have passed through the separation chamber and collected by the Faraday cages, turn off the RTS system.
(10) Adjust the electrometer to charge measuring mode. After the RTS separation test, connect the probe to a Faraday cage and measure the total product charge quantity every 0.5 second continuously for 20 seconds. Record the data to a personal computer. Repeat this step until all the product charge quantities are measured.
(11) Connect the individual products from the Faraday cages. Measure the weights of all the products respectively using an electric balance.
(12) Calculate the particle charge density as $Charge\ Density, nC/g = \frac{Total\ Product\ Charge\ Quantity, nC}{Total\ Product\ Weight, g}$.
(13) Repeated the RTS particle tribocharging test three times and calculate the average charge density for each test condition.

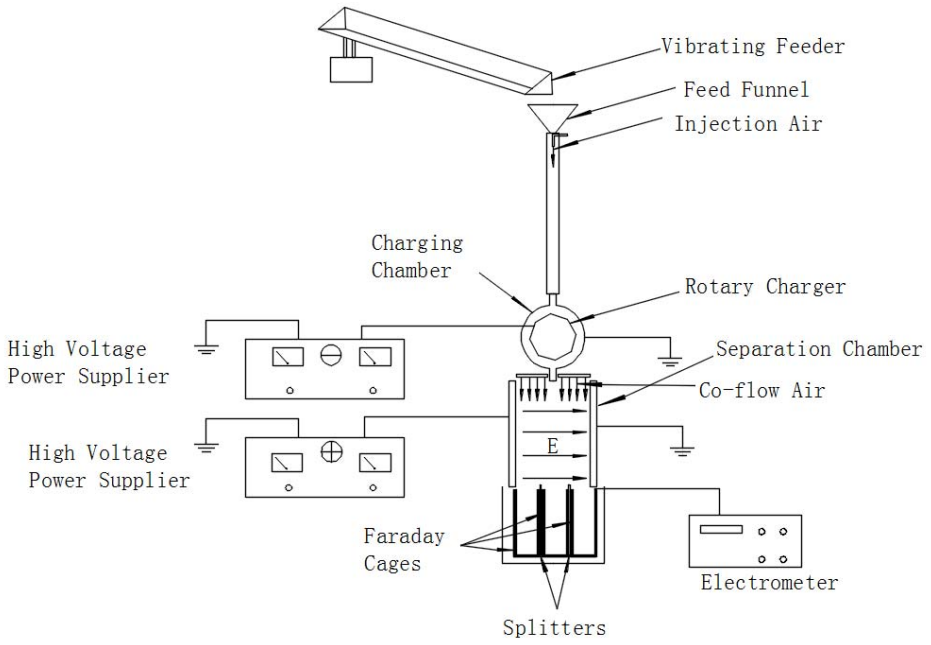

Figure 4.1. Experiment set up of rotary triboelectrostatic separator for particle tribocharging test with electrostatic separation.

During the process, particles were either charged by contact with the rotary charger or by contact with other particles. After tribocharging, all charged particles exited the charging chamber and then exposed to a strong external electric field of up to 488 kV/m. The charged particles moved towards the opposite electrode (i.e., cathode or anode plate) under the influence fo the Coulomb force. The particles traveled vertically through the separation chamber due to gravitation, and separated into positively charged particles, weakly charged particles or negatively charged particles. Since the concomitant minerals and the coal organic component have different surface electronic properties, the charged organic components theoretically should report to a stream opposite to the concomitants after tribocharging. High ash particles have a higher probability to be charged differently than the low ash particles. As a result, the process has the ability to split the raw feed coal into low ash product (concentrate), middling, and high ash product (tailing).

Different size particles have varying surface electronic properties due to surface compositions and the corresponding surface electronic properties of the components. Highly liberated fine particles are theoretically purer than large particles which process complex surface charges due to their mixed surface compositions. Considering that interactive forces can be influenced by particle mass, the particles with different size distributions under the same operating conditions must own different tribocharging efficiencies and hence different particle charge distributions. The best charge distribution was obtained by the largest surface charge density difference between the pure and impure particles. In other words, if the particle charge density distribution is wider for a group of particles, the pure and impure particles are more likely to obtain a broader surface charge difference which yields better separation performance.

Since the RTS operating conditions were identical when treating the various particle size fractions, the product charge distribution variation is reflective of the particle size difference. After completing the RTS separation, the charge measurements and the weights were used to

calculate the product charge density. The experimental data obtained from the treatment of each particle size fraction after the tribocharging are provided in Table 4.1.

Table 4.1. Particle tribocharging test result of different feed size ranges.

Particle Size Fraction, mm	Product	Charge Density, nC/g	Weight, %
-0.3	Negatively Charged	-2.68	28.67
	Weakly Charged	-0.03	33.67
	Positively Charged	0.29	37.66
0.3×0.21	Negatively Charged	-2.39	15.07
	Weakly Charged	0.48	21.01
	Positively Charged	0.85	63.92
0.21×0.105	Negatively Charged	-4.61	22.42
	Weakly Charged	-0.74	21.16
	Positively Charged	0.31	56.42
0.105×0.063	Negatively Charged	-5.58	45.28
	Weakly Charged	-2.12	21.01
	Positively Charged	1.55	33.71
-0.063	Negatively Charged	-5.96	51.57
	Weakly Charged	-3.41	23.63
	Positively Charged	7.24	24.80

Because the particle size is small and the coal specific gravity is low, the particle population involved in each test was substantial using a feed weight of 100 g. As such, a reasonable assumption based on the probability theory was that the particle charge distribution among the whole feed obeyed the Gaussian distribution. Therefore, the measured product charge density was considered to be the centroid of the particle charge density distributions within every product. The product charge density differences show the deviation of the particle charge density distribution. The total particle charge distribution was simulated by fitting the Gaussian distribution parameters to the specific experimental results. Matlab was used to assist simulating the Gaussian distribution. The calculated mean charge densities and deviations of charge density results are presented in Table 4.2. The plot of cumulative charge density distribution curves of different size feed coal samples after tribocharging are shown in Figure 4.2. The charge density distribution simulation results were compared against the result of the composite feed coal as a benchmark, which can reasonably reflect the characteristics of different components in the raw feed coal sample relative to the composite coal. The repeated charge distribution tests on the composite coal show the mean charge is $\sigma = -0.41 \pm 0.26$ nC and the standard deviation is $\delta = 1.35 \pm 0.07$ nC/g.

Table 4.2. Particle charge Gaussian distribution simulation result of different feed size coal.

Particle Size Fraction, mm	Product ID	Charge Density, nC/g	Weight, %	Average Charge Density (σ), nC/g	Standard Deviation (δ), nC/g
-0.3	Negatively Charged	-2.68	28.67	-0.67	1.29
	Weakly Charged	-0.03	33.67		
	Positively Charged	0.29	37.66		
0.3×0.21	Negatively Charged	-2.39	15.07	0.29	1.14
	Weakly Charged	0.48	21.01		
	Positively Charged	0.85	63.92		
0.21×0.105	Negatively Charged	-4.61	22.42	-1.01	1.98
	Weakly Charged	-0.74	21.16		
	Positively Charged	0.31	56.42		
0.105×0.063	Negatively Charged	-5.58	45.28	-2.43	3.16
	Weakly Charged	-2.12	21.01		
	Positively Charged	1.55	33.71		
-0.063	Negatively Charged	-5.96	51.57	-2.09	5.47
	Weakly Charged	-3.41	23.63		
	Positively Charged	7.24	24.80		

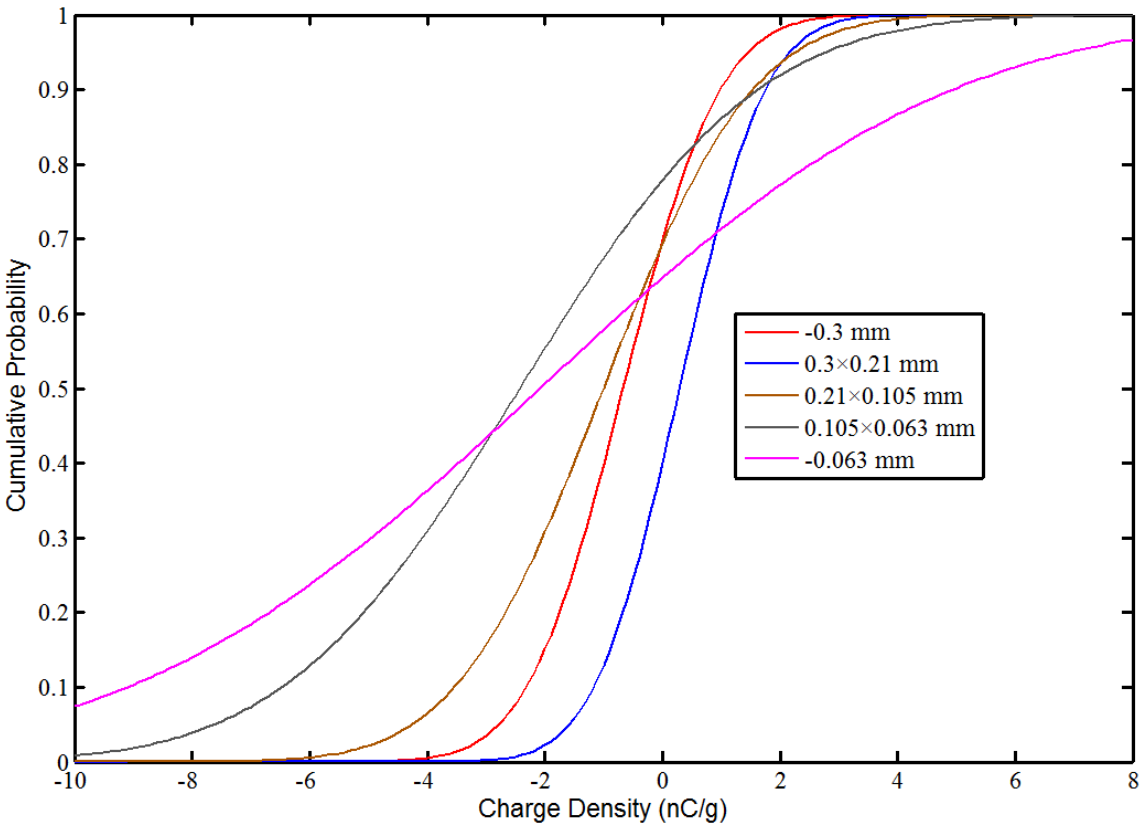

Figure 4.2. Cumulative charge density distribution of the first stage separation under the optimum operating conditions.

The mean charges as a function of particle size show a value approaching a stronger negative charge when the particle size decreases from 0.3 mm to 0.063 mm and then reverses when the particle size drops below 0.063 mm. Since the coal work function is 5.4 eV (Michaelson, 1977) and copper is 4.65 eV (Trigwell et al., 2007), the coal component obtained a negative charge after contact charging with the copper charger.

Analysis of the particle size effects can be provided from a theoretical perspective. When particle size decreases, more coal surface area was created for tribocharging. A previous analysis explained the correlation between a single particle charge and its diameter using the following expression (assuming that the surface components of the particle were identical after liberation):

$$\frac{dq_i}{dq_j} = \frac{k_i C_i V_i}{k_j C_j V_j} \propto \frac{d_i}{d_j} \tag{50}$$

However, a relationship between the total number particles with particle diameter under with the same total volume is:

$$\frac{N_i}{N_j} = \frac{\frac{1}{6}\pi d_j^3}{\frac{1}{6}\pi d_i^3} \propto \left(\frac{d_j}{d_i}\right)^3 \tag{51}$$

As such, the surface charge of a specific volume of material is the individual particle surface charge times the particle population. Therefore, the total available quantity of surface charge is inversely correlated to the square of particle diameter. This explains for the correlation between the product negative charge quantity and particle size. However, the smaller particle size fraction

realized a weaker particle-charger collision effect. The tribocharging efficiency of an individual particle theoretically declines with a decrease in particle size. As such, particles become more negatively charged with decreasing particle size but with a reducing increment. For the more liberated particles having a particle size smaller than 0.063 mm, the total average particle charge density rebounded only slightly due to the limited particle-charger tribocharging efficiency. The reduced charging efficiency was not countered by the significantly higher particle population.

The particles charging conditions could be reflected in the deviation of the product charge density distribution. This distribution was originally caused by the surface electronic property difference of the components under identical tribocharging conditions. Coal was preferentially charged negatively while the mineral matter was charged positively. A higher probability for the positively charged mineral matter and negatively charged organic material led to a larger deviation of the total particle charge density distribution. As such, larger standard deviation of the particle charge density distribution infers that the organic material and the mineral matter obtained the larger difference in surface charge densities.

4.3. The RTS separation test based on differently sized feed coal

To establish the correlation between the particle charge distribution generated by the RTS unit and coal beneficiation efficiency, the original rotary triboelectrostatic separator was used as shown in Figure 4.3. The operating conditions used in the RTS separation tests were identical to the RTS particle size-by-size tribocharging tests to ensure a means for comparing results. Samples collected at the end of each test were analyzed for ash content. The experiment procedures are described as below:

(1) Store the feed material in a drying oven before the test to reduce the coal surface moisture content to below 2% by weight.
(2) Check all components of the RTS to ensure that the unit is working properly. Make sure that the RTS is insulated and no short circuit exists inside the system.
(3) Turn on the vacuum system to initiate air flow through the unit. Measure the volumetric airflow rate in the three product streams. Adjust the air valve to ensure that the volumetric flow rates are equal.
(4) Adjust the operating conditions to the optimum conditions for the composite raw coal which include a solids feed rate of 20 kg/h, charger rotation speed of 4000 rpm, applied charger voltage of -5 kV, injection air rate of 1.9 m/s. The voltage supplied to the separation chamber is +25 kV.
(5) Maintain the same operating condition settings to treat all coal samples.
(6) Place the feed coal sample inside the vibrating feeder. Next, turn on the feeder.
(7) After all the particles have passed through the separation chamber and collected by the products collection bins, turn off the RTS unit.
(8) Take out all the products from the collection bins. Weight all the products and store them in separately marked bags.
(9) Analyze all samples for ash content using the standard ASTM procedure.
(10) Repeated the RTS separation test on the composite coal for four times.

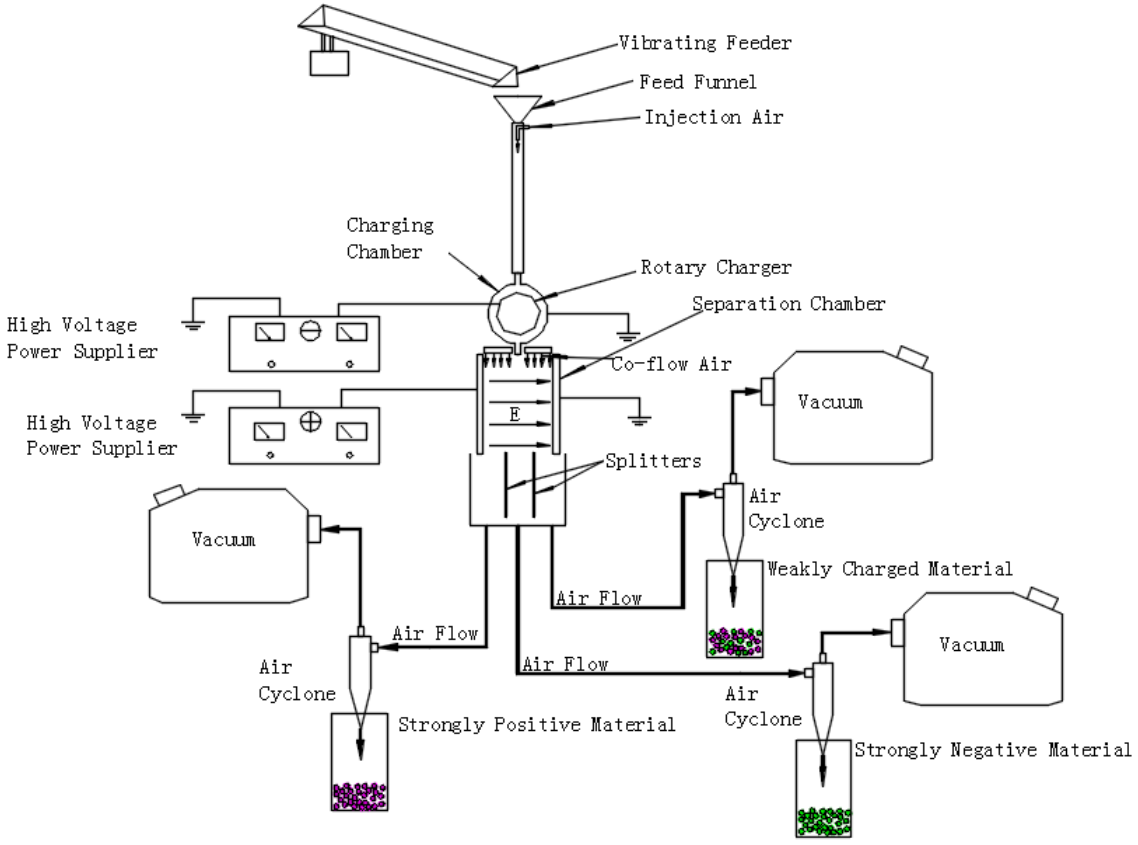

Figure 4.3. Experimental set up of the RTS apparatus for the particle rotary triboelectrostatic separation test.

The RTS separation test results obtained from the treatment of different size fractions are shown in Table 4.3. The calculated response variable values including cumulative ash, cumulative combustible recovery and ash rejection index based on the experiment data are presented in Table 4.4. The relationships between combustible recovery ash rejection as a function of particle size are plotted in Figure 4.4. The repeated tests on the composite coal indicated the following mean values and confidence intervals: ash content = $13.35 \pm 0.89\%$, recovery = $34.77 \pm 1.21\%$ and the ash rejection = $47.34 \pm 3.53\%$.

Table 4.3. RTS particle separation test results obtained when treating individual particle size fractions.

Product	Sample Size, mm									
	-0.3		0.3×0.21		0.21×0.105		0.105×0.063		-0.063	
	Ind. Ash, %	Ind. Wt, %	Ind. Ash, %	Ind. Wt, %	Ind. Ash, %	Ind. Wt, %	Ind. Ash, %	Ind. Wt, %	Ind. Ash, %	Ind. Wt, %
Concentrate	12.78	29.1	23.50	62.5	8.32	30.7	8.33	42.5	14.50	46.1
Middling	24.45	30.3	27.44	23.9	17.26	26.0	25.86	29.9	31.34	28.2
Tailing	35.04	40.5	40.12	13.6	34.52	43.3	54.42	27.7	59.26	25.7
Feed Ash Content, %	25.34		26.71		21.99		26.31		30.77	

Table 4.4. Separation response variable values obtained when treating individual particle size fractions using the RTS particle separator.

Particle Size Fraction, mm	Response Variable	Product		
		Concentrate	Middling	Tailing
-0.3	Cumulative Ash, %	12.78	18.73	25.34
	Cumulative Ash Rejection, %	49.6	26.1	0.0
	Cumulative Combustible Recovery, %	34.0	64.7	100.0
0.3×0.21	Cumulative Ash, %	23.5	24.59	26.71
	Cumulative Ash Rejection, %	12.0	7.9	0.0
	Cumulative Combustible Recovery, %	65.3	88.9	100.0
0.21×0.105	Cumulative Ash, %	8.32	12.42	21.99
	Cumulative Ash Rejection, %	62.2	43.5	0.0
	Cumulative Combustible Recovery, %	36.1	63.7	100.0
0.105×0.063	Cumulative Ash, %	8.33	15.56	26.31
	Cumulative Ash Rejection, %	68.4	40.9	0.0
	Cumulative Combustible Recovery, %	52.9	82.9	100.0
-0.063	Cumulative Ash, %	14.5	20.89	30.77
	Cumulative Ash Rejection, %	52.9	32.1	0.0
	Cumulative Combustible Recovery, %	56.9	84.9	100.0

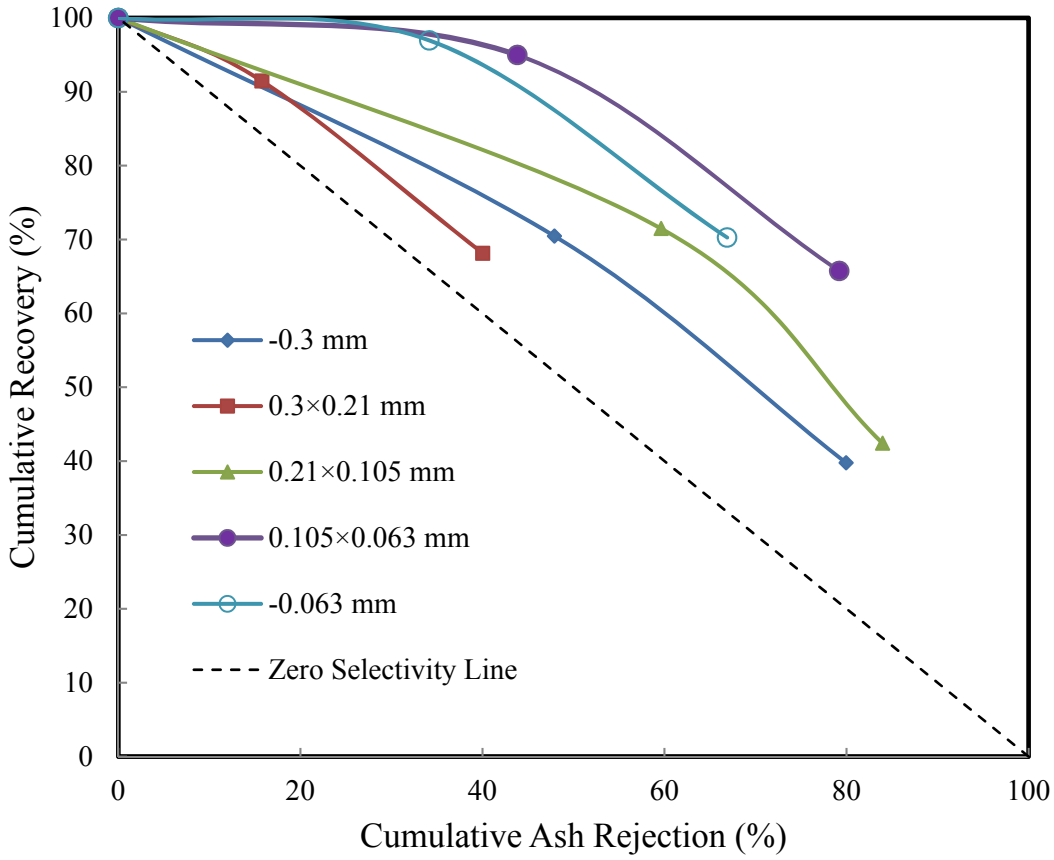

Figure 4.4. Combustible recovery relationships with product ash content as a function of the particle size fraction.

Ash rejection (=100-mass recovery × product ash content/feed ash content) was used to represent the degree of quality upgrading. Because the raw coal was classified into four size ranges, the composite ash contents of these samples were different. Ash rejection index normalizes the ash content parameter thereby allowing comparisons to be made between the separation performances achieved on each particle size fraction.

The experimental results show that the coarsest particle size fraction of 0.3×0.21 mm has the lowest separation efficiency as indicated by the close proximity of the data points to the non-sensitivity line. The concentrate ash content did not upgrade obviously, even though the recovery of concentrate was high. There could be two explanations for the experimental results. The first is the incomplete liberation of the organic material from the mineral matters, although liberation is generally not an issue for the particle size fraction in this study (Masuda et al., 1983). The second reason may be that the pure coal particle and the impure particles were not completely charged which impacts the ability to separate the particles. The percentage of the total surface area of a particle involved in the tribocharging process decreased with increasing particle diameter. This fact could result in an incomplete charge of the larger particles. Additionally, combining the fact that large particles have a complex surface composition, the mosaic charge phenomenon on a big particle surface was more significant (Baytekin et al., 2011). The mosaic surface charge is a mixing of negative and positive charges patched on the particle surface. Significant mosaic surface charge phenomenon could have negatively affected the correlation between the particle surface charge and particle purity, hence resulting in an ineffective separation.

With a decrease in particle size, ash rejection rose and then reached a peak for the 0.063-0.105 mm size fraction. This trend was most likely a result of improved particle tribocharging efficiency. The total percentage of an individual particle surface involved in the tribocharging process increased (assume all the particles had an equal probability of collision in the charging chamber). As such, the pure coal particles were more negatively charged and the impure coal particles were more positively charged. Better separation efficiency was achieved with a decrease in particle size.

For the material finer than 0.063 mm, the ash rejection index declined a little indicating a drop in the RTS coal separation efficiency. The first reason for this result may be a drop in tribocharging efficiency, which is reflected in the particle charge density distribution result. Moreover, the ultrafine particles were more easily affected by the ambient hydrodynamic conditions in the separation chamber. Particle misplacement probability increases with a decrease in particle size due to airflow turbulence in the separation process. To establish the correlation between the concentrate ash rejection and the particle charge distribution standard deviation, a second order polynomial regression was used to fit the experiment data as shown in Figure 4.5.

The depicted relationship between the particle charge density distribution standard deviation and ash rejection provides a visual picture of the particle charge range needed to maximize ash rejection (this red zone was specified by the minimum concentrate ash rejection index of 65%). When the particles charge distribution was lower than the minimum value, there was an insufficient amount of surface charge to allow the required amount of horizontal displacement. The pure and impure coal particles can be properly separated with an acceptable particle displacement difference. Additionally, the excessive surface charge associated with the impure coal particles did not negatively affect the separation process.

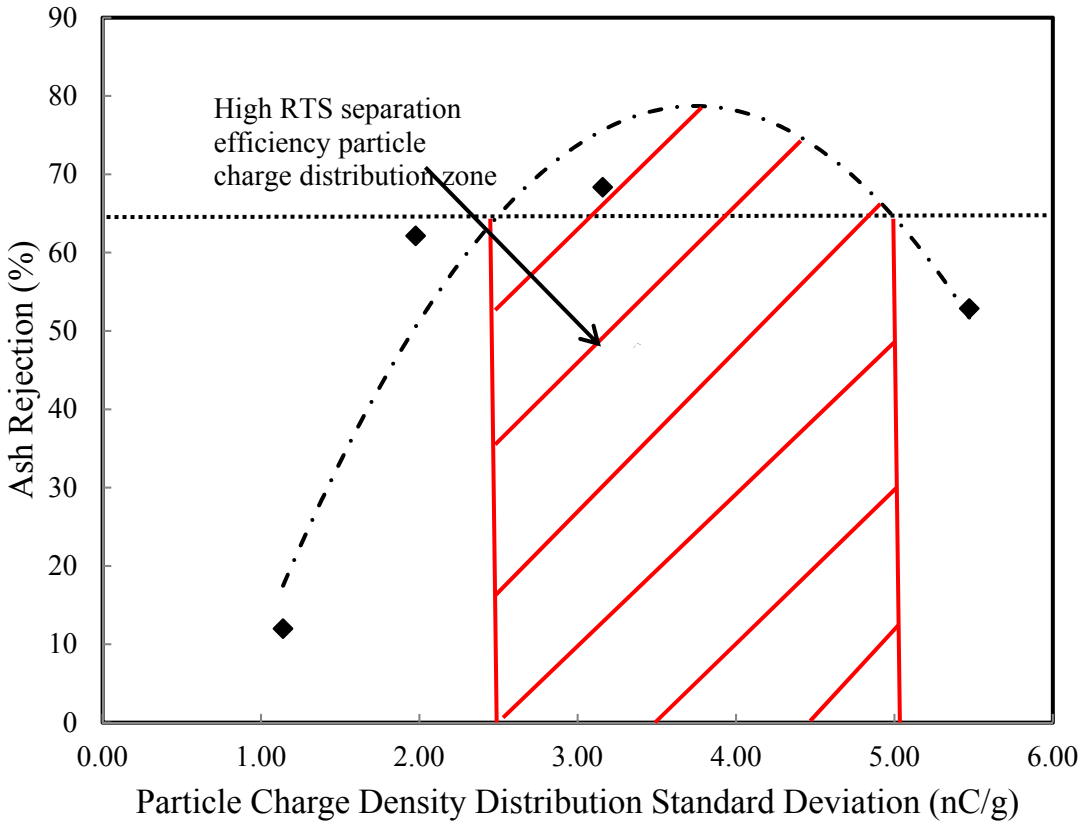

Figure 4.5. Correlation between the particle charge density distribution standard deviation and the concentrate ash rejection.

4.4. Dynamic analysis of particle separation process based on different sizes feed coal

Besides the particle charge distribution being influenced by the feed particle size range, the particle size also impacts the particle separation process. The airflow used to convey the particles in the system through the separation zone and the collection bins create environmental hydrodynamic conditions in the separation chamber that impact the performance achieved as a function of particle size. The non-laminar conditions in the separation chamber are reflected in the relative high Reynolds numbers used to model the process. The downward vertical air flow accelerates the downward particle movement and reduces the particle residence time in the separation process which decreases the particle horizontal movement distance as shown in Figure 4.6.

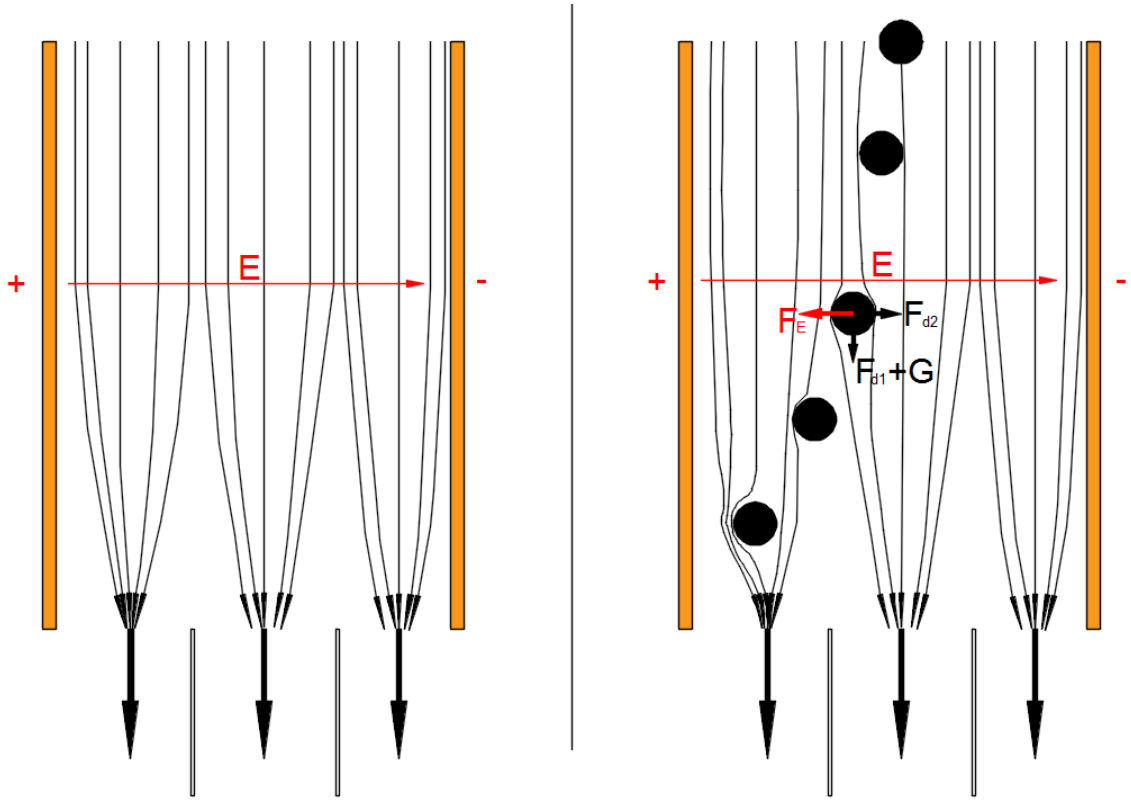

Figure 4.6. Schematic diagram of the hydrodynamic condition before and after the particles separation process.

Based on a force balance of around a charged particle in the separation chamber, the primary drag force (F_{d1}) acting on the particle from the airflow accelerates the particle falling rate, while the secondary drag force (F_{d2}) on the particle resistes particle movement towards the opposite electrode. The drag force associated with the particle movement (v_1 is vertical velocity and v_2 is horizontal velocity) and the airflow condition (u_1 is the vertical velocity and u_2 is the horizontal velocity) can be described by:

$$F_{d1} \propto (u_1 - v_1)^2 \rightarrow 0 \; when \; v_1 = u_1 \tag{52}$$

$$F_{d2} \propto (v_2 - u_2)^2 \rightarrow F_E \; when \; v_2 - u_2 = \sqrt{\frac{4\sigma_i E d_i}{3C_d}} \tag{53}$$

where σ_i is the particle charge density, d_i the particle diameter, E the electric field strength and C_d the drag coefficient.

It can be seen that the particle size influence of separation was both due to particle residence time in the separation process and horizontal displacement. These two factors together determined the trajectory of the charged particles in the separation chamber.

In the separation chamber, the downward flowing air exerts a downward drag force on the particles in the same direction as the gravitational force. Considering these two effects, the total vertical acceleration ($a_{1,i}$) can be quantified using the expression:

$$a_{1,i} = \frac{\rho_i (u - v_{1,i})^2 C_d A_i}{2m_i} + g \tag{54}$$

where A_i is the cross-sectional area of the particle, m_i is the particle mass, g is the gravitational acceleration rate. The instantaneous particle falling velocity ($v_{1,i}$) and the cumulative particle vertical displacement corresponding to the residence time t can be quantified by:

$$v_{1,i} = \int a_{1,i} t \, dt \tag{55}$$

$$x_{1,i} = \int \left(v_{1,i} t + \frac{a_{1,i} t^2}{2} \right) dt \tag{56}$$

Since the total designed vertical separation distance was 185 mm, the downward airflow velocity was measured as 4m/s. Based on the hydronic diameter of the chamber (D) and vertical air velocity, the Reynolds number was calculated using:

$$Re = \frac{\rho_{air} u D}{\mu} \propto C_d \tag{57}$$

Using the geological average particle size of each size fraction to represent the average size of total particle population, the corresponding particle residence time and terminal velocity after passing through the separation chamber were calculated as presented in Table 4.5. The drag coefficient number assumes semi-sphere aggregate particle shape.

Table 4.5. Mathematical calculation of particles residence time and falling velocity in the separation chamber.

Average Particle Size, mm	Falling Time, s	Falling Velocity, m/s	C_d	Reynolds Number
0.0025	0.0608	3.8123	0.42	20000
0.0813	0.1372	2.3984	0.42	20000
0.1485	0.1541	2.2215	0.42	20000
0.251	0.1665	2.111	0.42	20000

Smaller particles were easier to be influenced by the downward flowing air because the drag force contributed more to its vertical acceleration. As shown in Figure 4.7, the smaller particle had shorter residence time in the separation chamber. For larger particles, the residence time increased with a decreasing air rate.

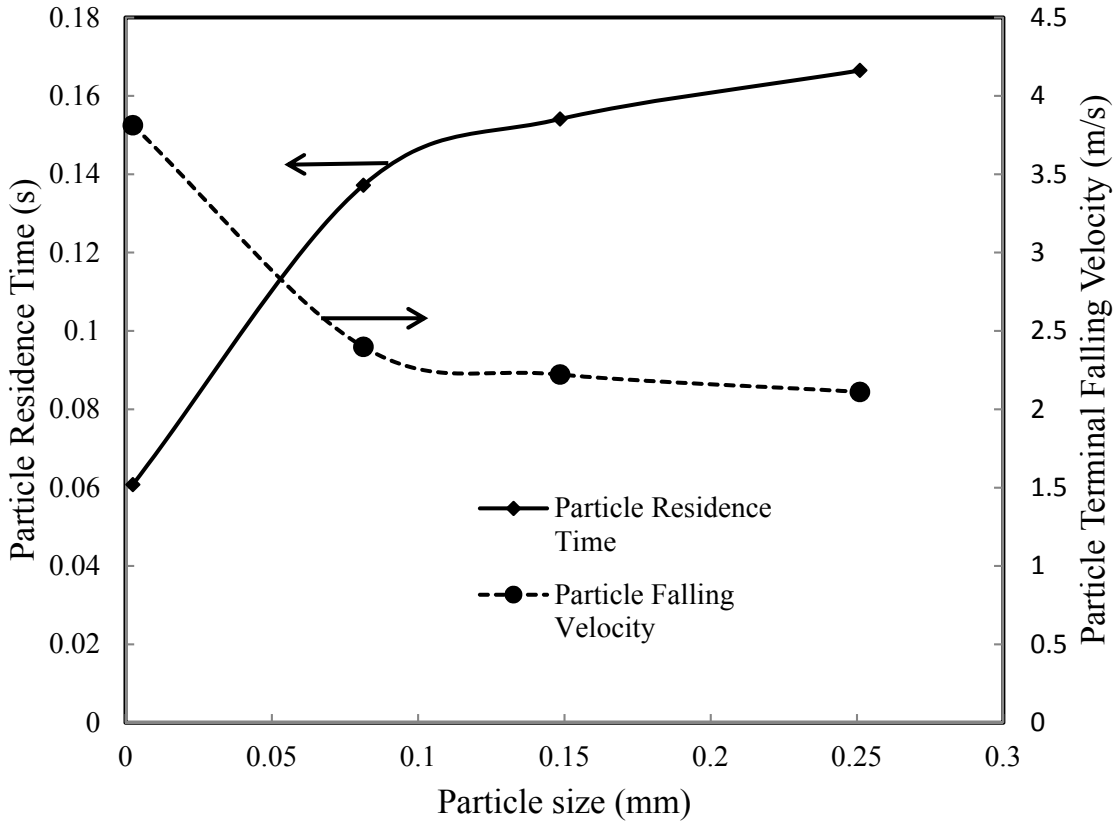

Figure 4.7. Particle residence time and terminal falling velocity in the separation chamber as a function of particle size.

After determining the particle residence time relative to particle size, quantifying horizontal displacement could be achieved. Though the air streams were in a downward direction, the turbulence inside the separation chamber and the particle crossing those air stream lines did cause horizontal drag force on the particles that resisted its horizontal movement. The angle θ was determined by the turbulent condition in the separation chamber, which resulted from the horizontal disturbance airflow quantity. It can be calculated with the direct measurement of air velocities in horizontal and vertical directions in the separation chamber. A strong electric field (with field strength of E=488 kV/m) in the separation chamber initiated horizontal motivation toward the opposite electrode. The particle surface charge density, σ_i, after the tribocharging process determined the particle electric field force in the separation chamber. Combining the electric field force and the drag force, the total particle horizontal acceleration rate ($a_{2,i}$) corresponding to the particle size was given as:

$$a_{2,i} = \frac{E\sigma_i m_i}{m_i} - \frac{\rho_{air}(usin\theta+v_{2,i})C_d A}{2m_i} \tag{58}$$

The instantaneous particle horizontal velocity, $v_{2,i}$, and the cumulative particle horizontal displacement were determined using the following expressions:

$$v_{2,i} = \int a_{2,i} t\, dt \tag{59}$$

$$x_{2,i} = \int \left(v_{2,i} t + \frac{a_{2,i} t^2}{2}\right) dt \tag{60}$$

Particles are fed into the separation chamber from the top center of the chamber. The total chamber width is 52 mm. As such, the maximum allowance for particle horizontal movement before colliding into the chamber wall is 26 mm. The mathematical calculation results based on the particle geological mean size, particle surface charge density and the air flow conditions are listed in Table 4.6. The particle horizontal movement was positively proportional to the particle charge density, as shown in Figure 4.8. Particles that have a higher surface charge density having a larger horizontal movement and the relationships are nearly linear. For particles having a horizontal displacement greater than the maximum allowance, the particle strikes the chamber wall and incurs a rebound effect. A relative small excess in the horizontal displacement still results in the proper collection into the correct bin. However, the surface charge of the particle could be partially neutralized or even reversed after the collision, which could impact the selectivity of the RTS separation process.

The horizontal movement accelerations rates were not the same for all the particle sizes, which as shown in Figure 4.9. Large particles obtain horizontal acceleration rates larger than the small particle thereby adding to the additional effect on residence time. For the smallest the particles, the most significant negative effect on horizontal acceleration was from air drag.

Empirical expressions relating the particle horizontal displacement with the particle surface charge density for different particle size ranges can be derived as:

$$x_{2,i} = \begin{cases} -0.562\sigma_i - 0.4691, & 0\ mm < d_i \leq 0.063\ mm \\ -4.3462\sigma_i - 0.0204, & 0.063\ mm < d_i \leq\ 0.105\ mm \\ -5.5793\sigma_i + 0.0064, & 0.105mm < d_i \leq 0.21\ mm \\ -6.5875\sigma_i + 0.0669, & 0.21\ mm < d_i \leq 0.3\ mm \end{cases} \quad (61)$$

The previously derived semi-empirical expressions for the particle charge distribution from the RTS particle charging test (Table 4.2) are presented as:

$$f(\sigma_i) = \begin{cases} 0.0729e^{-\frac{(\sigma_i+2.09)^2}{59.8418}}, & 0\ mm < d_i \leq 0.063\ mm \\ 0.1262e^{-\frac{(\sigma_i+2.43)^2}{19.97}}, & 0.063\ mm < d_i \leq 0.105\ mm \\ 0.2015e^{-\frac{(\sigma_i+1.01)^2}{7.8408}}, & 0.105\ mm < d_i \leq 0.21\ mm \\ 0.3499e^{-\frac{(\sigma_i-0.29)^2}{2.5992}}, & 0.21\ mm < d_i \leq 0.3\ mm \end{cases} \quad (62)$$

Therefore, the semi-empirical expressions representing the particle displacement distribution (probability) were derived for each particle fraction, e.g.:

$$P(x_{2,i}) = \begin{cases} 0.0729e^{-\frac{\left(-\frac{x_{2,i}+0.4691}{0.562}+2.09\right)^2}{59.8418}}, & 0\ mm < d_i \leq 0.063\ mm \\ 0.1262e^{-\frac{\left(-\frac{x_{2,i}+0.0204}{4.3462}+2.43\right)^2}{19.97}}, & 0.063\ mm < d_i \leq 0.105\ mm \\ 0.2015e^{-\frac{\left(-\frac{x_{2,i}-0.0064}{5.5793}+1.01\right)^2}{7.8408}}, & 0.105\ mm < d_i \leq 0.21\ mm \\ 0.3499e^{-\frac{\left(-\frac{x_{2,i}-0.0669}{6.5875}-0.29\right)^2}{2.5992}}, & 0.21\ mm < d_i \leq 0.3\ mm \end{cases} \quad (63)$$

The above expression can be used to quantify the probability of particle horizontal displacements of particles within a specific size range. The particle horizontal displacement probabilities based on this study were plotted in Figure 4.10. This result reflected the probability of a particle (with specific size range) that can finally achieve the horizontal displacement after the RTS separation based on the specific experimental conditions of this study. In other words, the probability value represents the weight percentage of particles within a specific size range collected in the concentrate (or tailing) given the splitter position measured as a specific distance from the center line. The expression can be used to study the effect of changing operating conditions, feed samples, or even experiment rig configuration. It is of great value in practice to establish the benchmark under any desired experimental conditions.

Table 4.6. Mathematical calculation of particle horizontal movement.

Average Particle Size, mm	Particle Charge density, nC/g	Residence Time, s	Horizontal Velocity, m/s	C_d	Reynolds Number	Displacement, mm
0.0025	-6	0.0608	0.0758	4.2	1000	2.9
	-5	0.0608	0.0621	4.2	1000	2.4
	-4	0.0608	0.0475	4.2	1000	1.8
	-3	0.0608	0.0319	4.2	1000	1.2
	-2	0.0608	0.015	4.2	1000	0.5
	-1	0.0608	0	4.2	1000	0
	-0.5	0.0608	0	4.2	1000	0
0.0813	-6	0.1372	0.363	4.2	1000	26
	-5	0.1372	0.3051	4.2	1000	21.7
	-4	0.1372	0.2461	4.2	1000	17.4
	-3	0.1372	0.1859	4.2	1000	13.1
	-2	0.1372	0.1245	4.2	1000	8.7
	-1	0.1372	0.0617	4.2	1000	4.3
	-0.5	0.1372	0.0299	4.2	1000	2.1
0.1485	-6	0.1541	0.4216	4.2	1000	33.4
	-5	0.1541	0.3536	4.2	1000	27.9
	-4	0.1541	0.2846	4.2	1000	22.4
	-3	0.1541	0.2147	4.2	1000	16.8
	-2	0.1541	0.1437	4.2	1000	11.2
	-1	0.1541	0.0716	4.2	1000	5.6
	-0.5	0.1541	0.0352	4.2	1000	2.7
0.251	-6	0.1665	0.4656	4.2	1000	39.5
	-5	0.1665	0.3898	4.2	1000	33
	-4	0.1665	0.3132	4.2	1000	26.5
	-3	0.1665	0.2359	4.2	1000	19.9
	-2	0.1665	0.1578	4.2	1000	13.3
	-1	0.1665	0.0788	4.2	1000	6.6
	-0.5	0.1665	0.039	4.2	1000	3.3

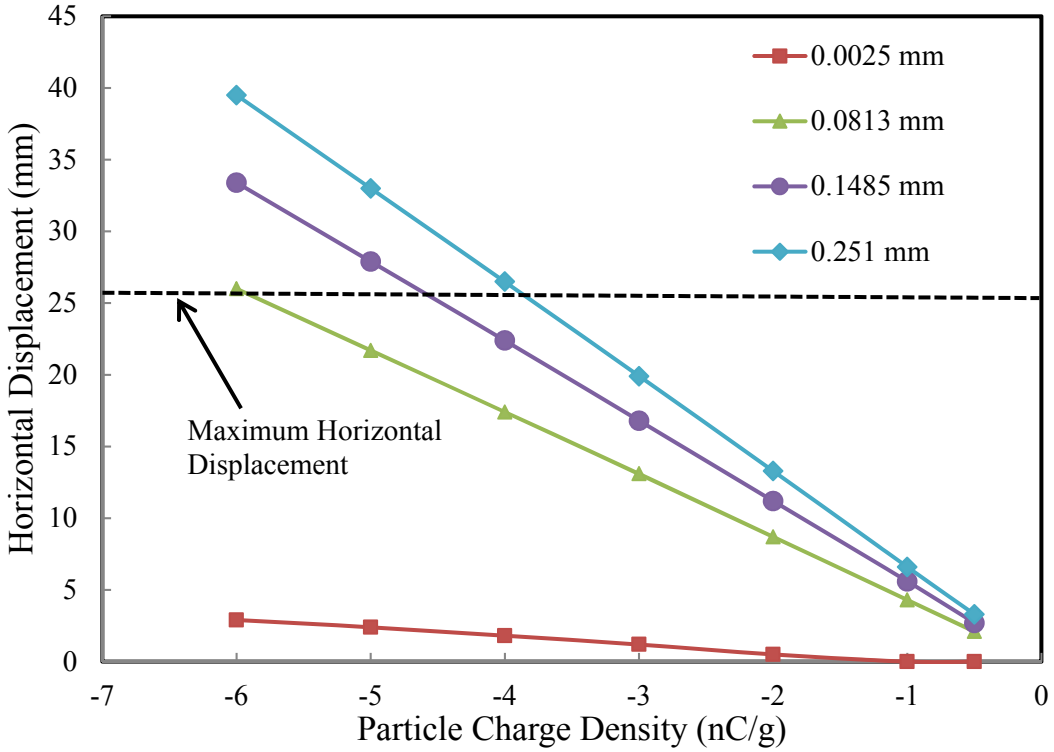

Figure 4.8. Particle horizontal movement displacement corresponding to particle surface charge.

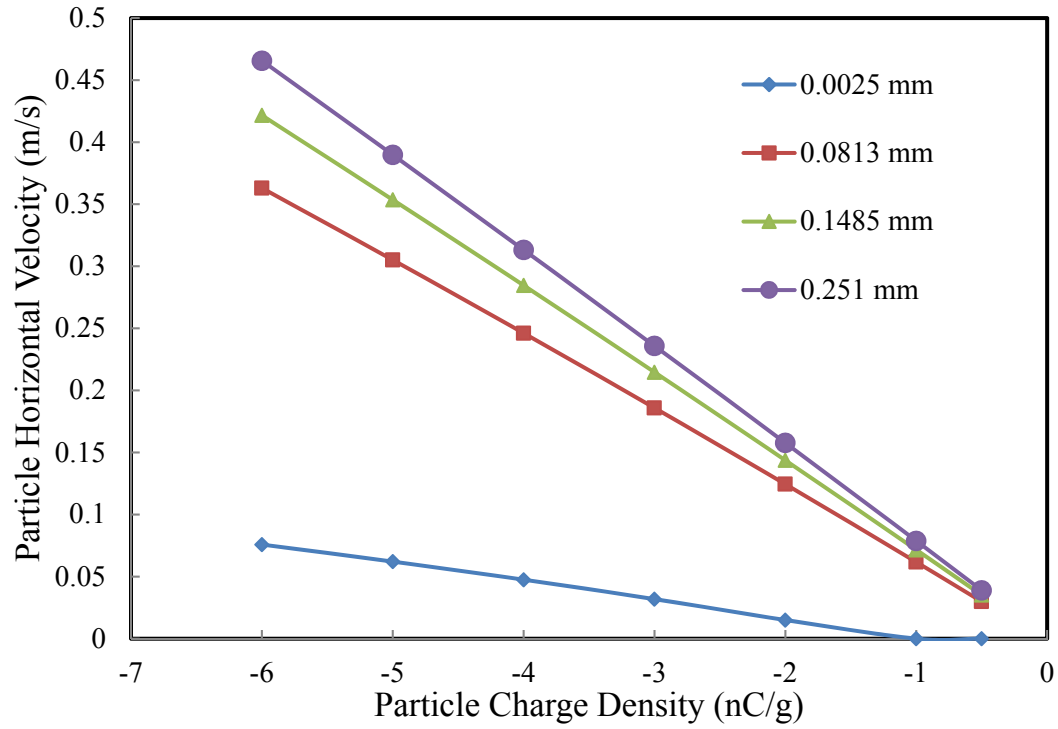

Figure 4.9. Particle horizontal velocities after the specific residence times.

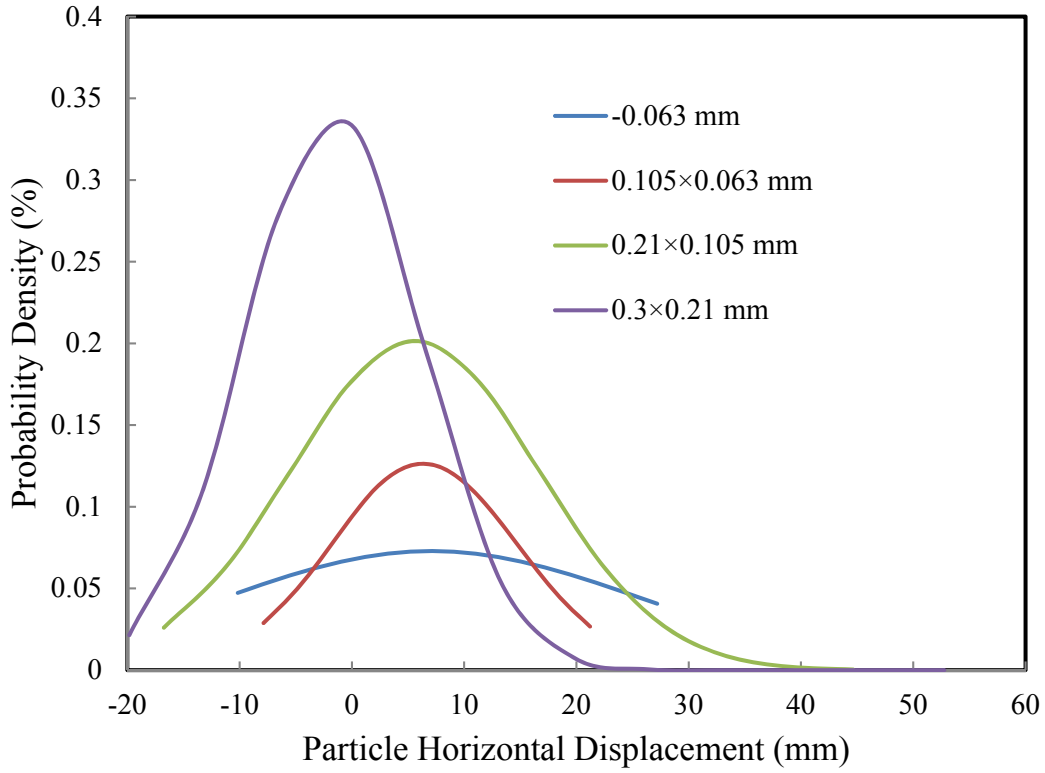

Figure 4.10. The probability of horizontal displacement after RST separation for a particle with specific size.

Previous analysis shows that the particle size influences both the particle charging condition in the charging chamber and the particle movement in the separation chamber. Particle charging was proportional to its surface area. Smaller particles have a larger total surface area to mass ratio, which provides more sites for the charge exchange in the tribocharging process. Additionally, since the individual particle mass is proportional to its mass, smaller mass favors the generation of larger particle charge density. A decrease in particle size reduces the particle inertia that deteriorates its interaction with the rotary charger. The total surface charge density was greatly negatively impacted to a significant degree by particle size reduction especially at the ultrafine particle size.

In the separation process, the particle size effect on separation performance is a direct result of a change in vertical movement and horizontal displacement. Vertically, the particle travels within separation chamber over finite definite distance, which determined its residence time in the separation process. The particle residence time was found to almost exponentially increase with the particle size due to air drag force on small particles was much larger than the gravitational force which quickly transports the particles out of the separation chamber. Horizontally, the particle movement is impacted by the particle surface charge density and the turbulent conditions inside the chamber. The electric field force drives the charged particle moving towards the opposite electrode. Turbulence associated with the air inside the chamber resists particle moving. The residence time controls the particle total horizontal acceleration time and hence its total horizontal displacement. The total particle displacement difference was desired to be maximized corresponding to the particle surface electronic properties, which provided the highest probability of separation. Any collision between the charged particle and the chamber wall should be minimized to avoid the negative effects on particle charge and thus separation efficiency.

Because the basic components of RTS separation consist of particle tribocharging and particle separation, the particle size was correlated with both the particle tribocharging process and the particle separation process. Particle surface area, surface electronic properties and particle mass play important roles in the particle RTS separation. Mathematical expression developed based on the experiment results and governing fundamental force balances provide a practical method for analyzing the RTS separation fundamentals and RTS separation efficiency.

4.5. Summary

In this study, particle size was studied as a parameter impacting the RTS separation efficiency. The particle size proved to influence both the particle tribocharging process and the particle separation process. As such, the particle separation conditions should be controlled based on the desirable conditions needed to maximize tribocharging efficiency for a given particle size fraction.

Particle size influenced the tribocharging in two ways – (1) the total surface area available for tribocharging and (2) the particle-charger interactive effect. Experiment results show that the particle surface area was significant in impacting the particles surface charge. Smaller particles had higher total surface area for charge exchange. However, decreasing particle size reduced the particle-charger interactive effect, which negatively influenced the particle surface charge. A Gaussian distribution model was used to simulate the particle charge density distribution after the RTS tribocharging process. The simulation results indicated that the mean charge changed from 0.29 to -2.43 nC/g with the decreasing feed coal size. However, if the particle size was too small, continuously shank the particle size could deteriorate the particle-charger tribocharging efficiency, which was reflected by the charge density reduction back to -2.09 nC/g for the smallest feed coal sample. The experiment result also shows the smaller the feed coal size, the wider the particle surface charge density distribution. It indicates that the pure and the impure coal particles were charged differently. The charge density standard deviation increased from 1.14 to 5.47 nC/g with a decrease in feed particle size. Wider particle charge density distribution provided the basis for improved RTS separation. According to the RTS separation results, the best range of standard deviation of charge density distribution was derived according to the specified concentrate reduction index requirement.

Particle size defined the sensitivity of particle movement corresponding to the ambient environmental hydrodynamic conditions. Smaller particles had limited inertia which makes it easier to be affected by the air flow. The air flow condition inside the separation chamber controlled the particle residence time in affecting the vertical movement and the extent of separation created by horizontal displacement. Mathematical predictions and statistical analysis based on the particle charging results and experimental conditions were conducted to analyze the particle separation process. Smaller particle had a limited residence time in the separation chamber that allowed quick exciting by the air stream. Though large particles with high mass were less influenced by the airflow, it did not favor the generation of high particle charge density. If a large particle was strongly charged, collision with chamber walls prior to collection causes particle misplacement and a reduction in separation efficiency. A particle charge analysis and separation analysis were integrated to derive the particle RTS separation fundamentals. The air flow conditions need to be controlled according to the particle charging condition to maximize the RTS separation efficiency. Based on the experimental conditions and feed materials used in this study, the optimum particle size range for the coal RTS separation was found to be 0.063-0.105 mm.

5. Coal-Silica Particle Rotary Triboelectrostatic Separation Test

5.1. Introduction

Silica mineral is a major contaminant in most run-of-mine coals. Silica deteriorates coal quality and produces environmental pollution after coal burning. Conventional wet processing methods (dense media separation and flotation) are generally used to remove the silica and upgrade the coal. However, large quantities of water and the use of chemicals both increase operating cost and complicate downstream water treatment processes. As such, if a low-cost and simple dry processing method could supplant the conventional wet processing techniques, the overall production can be more cost-efficient and environmental-friendly.

Triboelectrostatic separation is a dry separation technology. The process has a potential application in coal beneficiation due to surface electronic property differences between coal and silica particles as well as other mineral matter types. No water and chemicals are required during the separation process. Simpler separation procedure and lower operating cost make it more competitive against the wet processing technology (Zhang and Honaker, 2015; Zhang et al., 2016). The patented rotary triboelectrostatic separator (RTS) has an innovative design for particle tribocharging and a good control of the particle separation process to achieve a range of clean coal quantities. It has been successfully tested for the beneficiation of coal (Bada et al., 2010; Tao et al., 2011), phosphate (Bada et al., 2013; Sobhy and Tao, 2014), unburned carbon from fly ash (Tao et al., 2009) and so on. Larger surface charge density difference between the coal and minerals is the basis for improving the electrostatic separation process. The non-contact design of particle separation chamber could assist in maintaining the particle surface charge during the separation process. The controllable hydrodynamics of the air inside the separation chamber has potential to impact the charged particles trajectories, which could benefit particle separation.

In this study, a model system comprised of coal and silica particles was tested used to study the separation achieved by the RTS process. The rotating charger in the RTS unit was covered with pure copper, which provided a positive assistance to charge the coal component and the silica differently based on their relative work functions. The operating conditions of the RTS were studied about their effect on the coal-silica mixture beneficiation, which then determined the optimum operating conditions. The best achievable coal-silica mixture RTS separation characteristic was depicted. The particle-particle tribocharging effect was derived using an indirect method according to the pure materials charging distributions and the RTS separation result.

5.2. Experimental

5.2.1. Materials

The coal-silica mixture sample was made of pure silica (ASTM purity>99%) and pure coal (bituminous coal, Sp.Gr.<1.35) in a weight ratio of 1:1. Both the pure coal and the pure silica had a particle size range of 1×0.15 mm. The pure coal (ash content: 4.3%±0.05%) and the pure silica was blended in an empty rotating ball mill for fifteen minutes at 15 rpm. The coal-silica mixture had a composite ash content of 54.4%. The mixture sample was placed in a drying oven for over 12 hours to reduce the surface moisture content below 2% and then stored in sealed sample bags. All the experiments were carried out at a room temperature of 71 °F and relative humidity of 40%.

5.2.2. Rotary triboelectrostatic separation

In each test, 150 grams of coal-silica mixture sample was used as feed material. There was a vibrating feeder mounted on the top of the RTS that sends the feed sample to the separator. Before the particles enter the charging chamber, there is about 0.4 m distance for the particle to accelerate downward. All the particles moved with a downward flowing injection air, which resulted in a high terminal velocity prior to impacting the rotating charger. In the charging chamber, the rotating charger interacted with the particles causing a charge differential in polarity and total charge between the coal and silica particles. Particles exiting the tribocharging process enter a separation chamber from the top center. One chamber wall was connected to a DC power supplier while the other wall was ground. During the separation process, a strong electric field was generated within the separation chamber that applied an electric field force on the charged particles. Particles with surface charges were attracted by the opposite electrode.

Because the coal and the silica have different surface electronic properties, they obtained an opposite surface charge in quantity and/or polarity after tribocharging with the copper rotating charger. Differently charged particles had distinguishable horizontal displacements after passing through the separation chamber. Finally, two splitters at the bottom of the separation chamber separated the coal-silica mixture into three products. After the test, all the products were weighted and sent to the ash analysis (ASTM D 3174-12).

The charging chamber of the RTS has an innovative octagonal design. The particles are transported by the air flow and impacted with the variable speed rotating charger. A strong electric field between the charger and the chamber wall facilitates an electron transfer at the interface. As such, the action combines tribocharging and inductive charging mechanisms to enhance the particle overall tribocharging efficiency. Particle-particle tribocharging also occurred in the charging chamber due to turbulent conditions produced by the rotating charger. However, the amount of charge exchanged by particle-particle tribocharging is difficult to quantify.

A single factor experimental design method was used to investigate the influences of operating parameters on the coal-silica mixture RTS separation efficiency. Five operating parameters (feed rate, charger rotating speed, rotary charger voltage, injection air rate, and co-flow rate) were studied within their typical operational ranges to evaluate their effects on separation performance. The standard operating conditions for the test were set as a rotary charger speed of 5000 rpm, feed rate of 9.1 kg/h, injection air rate of 1.9 m/s, co-flow rate of 1.5 m/s and the applied rotary charger voltage of 5 kV unless otherwise specified. The optimum operating conditions were determined from the single factor designed experiment results.

Afterwards, another test was conducted under the optimum operating conditions using five cleaning stages. The charge distributions on the pure silica and the pure coal under the optimum operating conditions were measured to assist in analyzing the coal-silica mixture triboelectrostatic separation process. Particle net charges of all the separated products were obtained using three modified Faraday Cages. The electrometer (Keithley 6514) measured the product charge individually and then transferred the measured data to a PC. Particle charge quantity was measured in units of nC.

5.3. Effects of operating parameters on triboelectrostatic separation performance

The mixture was separated into three products after every RTS separation test. The three products were labeled as concentrate, middling and tailing based on their ash content. The parametric values used in the single factor experiment design are provided in Table 5.1. The experimental results obtained from the RTS separation tests are shown in Table 5.2. The ash contents and the

corresponding combustible recovery values for all products were used to identify the RTS separation efficiency.

Table 5.1. Single factor experiment design of coal-silica mixture RTS separation test.

Experiment Number	Feed Rate, kg/h	Charger Rotation Speed, rpm	Applied Charger Voltage, kV	Injection Air Rate, m/s	Co-flow Air Rate, m/s
1	0.9	5000	5	1.9	1.5
2	2.3	5000	5	1.9	1.5
3	4.5	5000	5	1.9	1.5
4	9.1	5000	5	1.9	1.5
5	13.6	5000	5	1.9	1.5
6	9.1	2000	5	1.9	1.5
7	9.1	3000	5	1.9	1.5
8	9.1	4000	5	1.9	1.5
9	9.1	5000	3	1.9	1.5
10	9.1	5000	1	1.9	1.5
11	9.1	5000	0	1.9	1.5
12	9.1	5000	-1	1.9	1.5
13	9.1	5000	-3	1.9	1.5
14	9.1	5000	-5	1.9	1.5
15	9.1	5000	5	0.6	1.5
16	9.1	5000	5	3.1	1.5
17	9.1	5000	5	4.3	1.5
18	9.1	5000	5	1.9	1.8
19	9.1	5000	5	1.9	2.1
20	9.1	5000	5	1.9	2.4

Table 5.2. Experiment result of coal-silica mixture RTS separation test.

Test Number	Concentrate		Middling		Tailing	
	Recovery, %	Ash, %	Recovery, %	Ash, %	Recovery, %	Ash, %
1	7.4	49.64	17.5	55.62	75.0	56.33
2	5.8	49.07	15.0	50.89	79.2	55.35
3	8.4	37.81	18.0	48.23	73.6	56.97
4	10.0	31.16	17.7	48.26	72.3	57.61
5	9.0	34.46	16.3	49.36	74.7	56.91
6	4.5	36.97	21.4	42.06	74.2	57.70
7	3.5	35.50	20.0	41.91	76.5	57.36
8	8.3	24.66	13.9	53.62	77.9	56.36
9	10.3	38.72	20.0	49.64	69.7	57.18
10	12.9	43.42	26.2	54.33	61.0	56.22
11	14.6	42.89	27.6	50.97	57.8	57.94
12	31.9	50.00	43.8	50.77	24.3	63.48
13	28.9	48.65	45.4	52.01	25.7	62.44
14	34.1	40.96	38.0	59.98	28.0	58.08
15	12.7	26.88	12.7	52.66	74.7	57.39
16	7.7	31.96	18.1	41.04	74.3	58.14
17	10.4	43.24	26.4	54.61	63.3	55.74
18	11.6	30.57	14.6	49.85	73.8	57.46
19	10.0	24.41	11.6	53.35	78.5	56.73
20	10.1	29.37	15.3	46.71	74.6	57.68

5.3.1. Feed rate

The feed rate was varied from 0.9 kg/h to 13.6 kg/h to study its influence on the RTS separation efficiency. The product ash distribution and recovery distribution were shown in Figure 5.1. The experiment result showed when the feed rate increased from 0.9 kg/h to 9.1 kg/h, the concentrate ash content continuously decreased from 49.64% to 31.16%. This is because a higher feed rate provides a larger particle population inside the charging chamber during the particle tribocharging process. Increasing the number of coal-silica collisions elevated the charge exchange between the particles. As such, the clean coal particle and the silica particle were more differently charged thereby making the clean coal particles more easily recovered. When the feed rate was continuously increased to 13.6 kg/h, the clean coal ash content reversed back a little to 34.46%. It might be caused by the less clean coal particles collected in the concentrate. This result infers that the coal-silica tribocharging effect was too high due to a high probability of coal-silica contact. Some clean coal particles gained too much surface charge and rebounded after hitting the chamber wall, which resulted in their collection into other product bins.

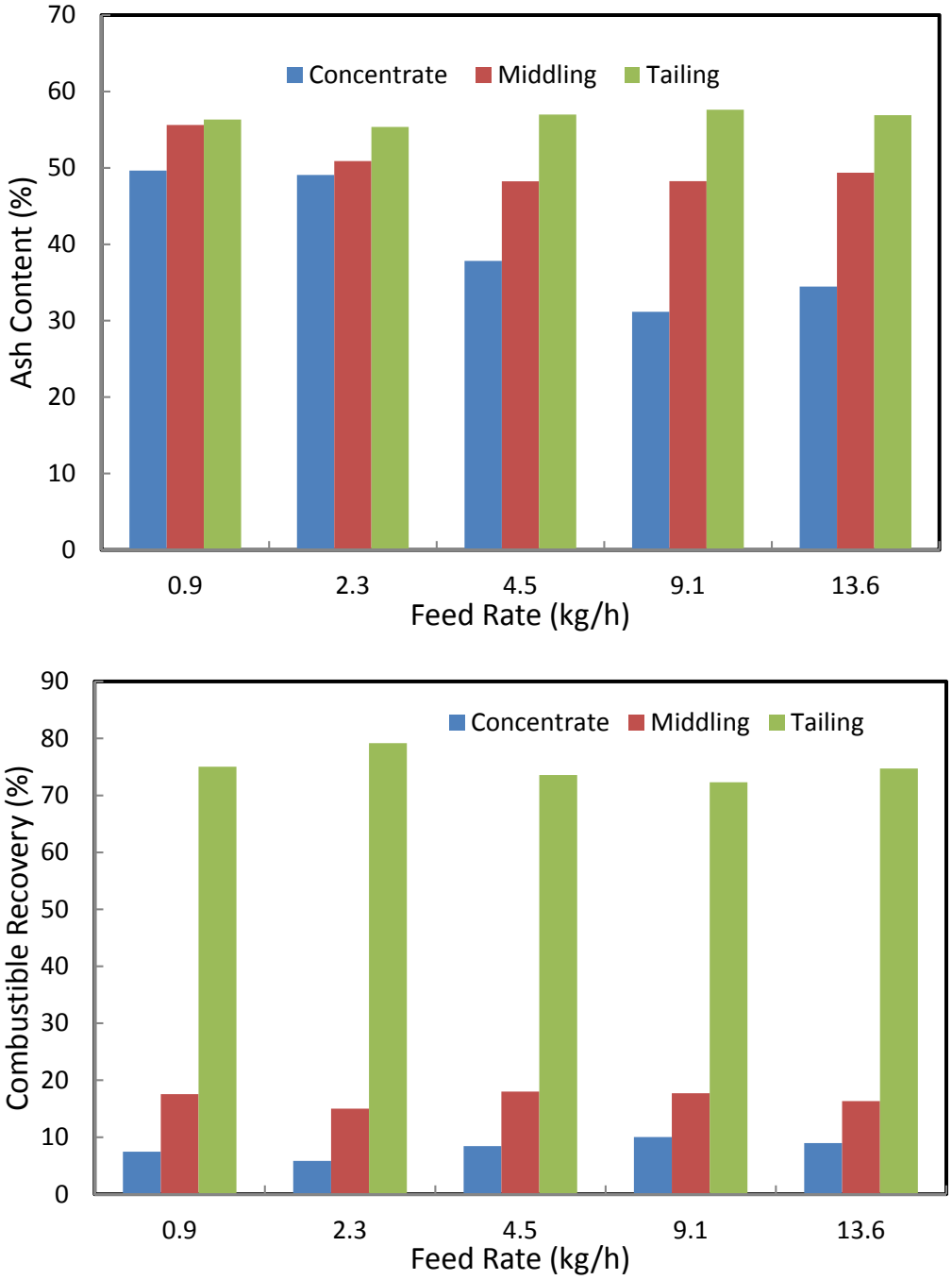

Figure 5.1. Effect of feed rate on the coal-silica mixture RTS separation: (a) product ash distribution and (b) product recovery distribution.

5.3.2. Charger rotation speed

The purpose of the rotating charger is to enhance the particle charger interaction, which directly increases the particle tribocharging efficiency. The magnitude of the normal interactive force resulting from the collision between the falling particles contacted and the rotating charger directly determines the charge on the particle surface. The contribution of the friction component is also correlated with the charger-particle relative velocity. Previously reported findings indicate that the friction effect is positively correlated with the particle tribocharging efficiency (Burgo et al., 2013; Nakayama, 1996). Additionally, with an increase in the rotary charger speed, the turbulent condition inside the charging chamber was also elevated. The maximum charger rotating speed was set at 5000 rpm to prevent the surface covered copper from excessive wear. As shown in Figure 5.2, when the charger was rotating at 2000 and 3000 rpm, the concentrate ash contents were similar (35.5%-36.97%). The clean coal ash content dropped to 24.66% when the rotating speed was elevated to 4000 rpm. This finding seems to indicate that the charging efficiency in the mineral matter is significantly improved at the higher rotation speed which provides improved rejection to the tailing stream. However, when the charger rotating speed continuously increased to 5000 rpm, the clean coal ash content rose back to 31.16% which may be due to the rebound effects from the clean coal particles striking the chamber walls thereby reporting to middling and tailing bins. As such, the optimum charger rotating speed was estimated to be 4000 rpm.

5.3.3. Rotary charger voltage

The rotary charger was connected to a DC power supplier, which provided a strong electric field between the charger and the grounded chamber. When a particle touched the charger, there was inductive charge effect on this particle. The electric field provides driving force on the free charges to transfer across the interface. This unique design could significantly enhance particle tribocharging efficiency. The applied charger voltage was adjusted from -5 kV to 5 kV to evaluate its influence on the mixture RTS separation efficiency. The experiment result was shown in Figure 5.3. When the charger voltage was positive, it assisted in producing low ash concentrate. However, when the applied charger voltage was switched to negative, it produced high ash clean coal with high recovery. It indicates that the applied charger voltage was a significant factor influencing the particle RTS tribocharging and thus separation. The applied charger voltage modified the magnitude and direction of the generated electric field between the charger and chamber wall. As such, the free electrons experienced different electric field force when they were transferring across the contacting interface. The applied charger voltage finally affected particle surface charge. The clean coal ash content decreased from 43.42% to 31.16% when the applied charger voltage rose from 0 kV to 5 kV. When the applied charger voltage changed from -1 kV to -5 kV, the recovery of concentrate increased from 28.90% to 34.05% combined with the ash content reduction from 50.00% to 40.96%. As a result, the positive applied charger voltage was preferred for producing a better quality concentrate. The lowest ash concentrate can be produced if the applied charger voltage is 5 kV.

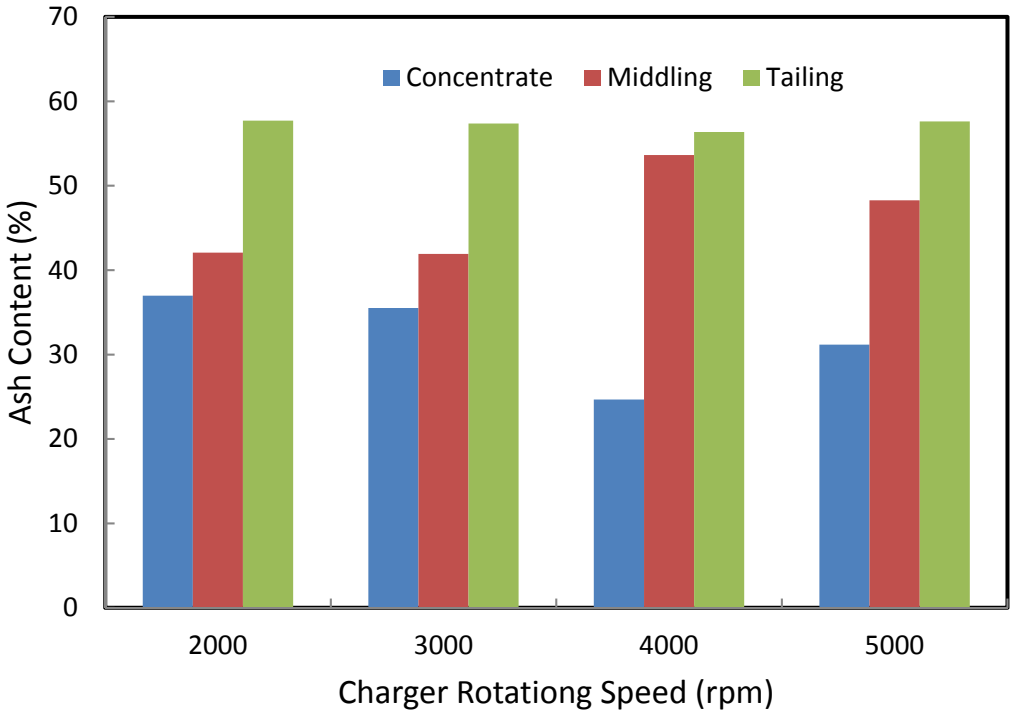

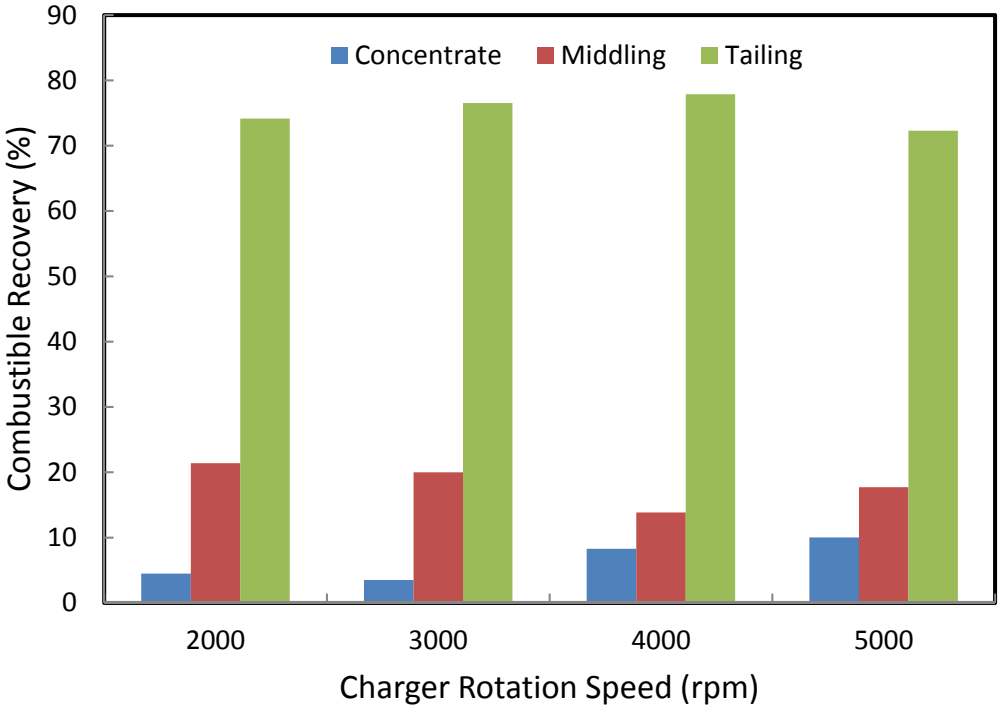

Figure 5.2. Influence of charger rotation speed on the coal-silica mixture RTS separation: (a) product ash distribution and (b) product recovery distribution.

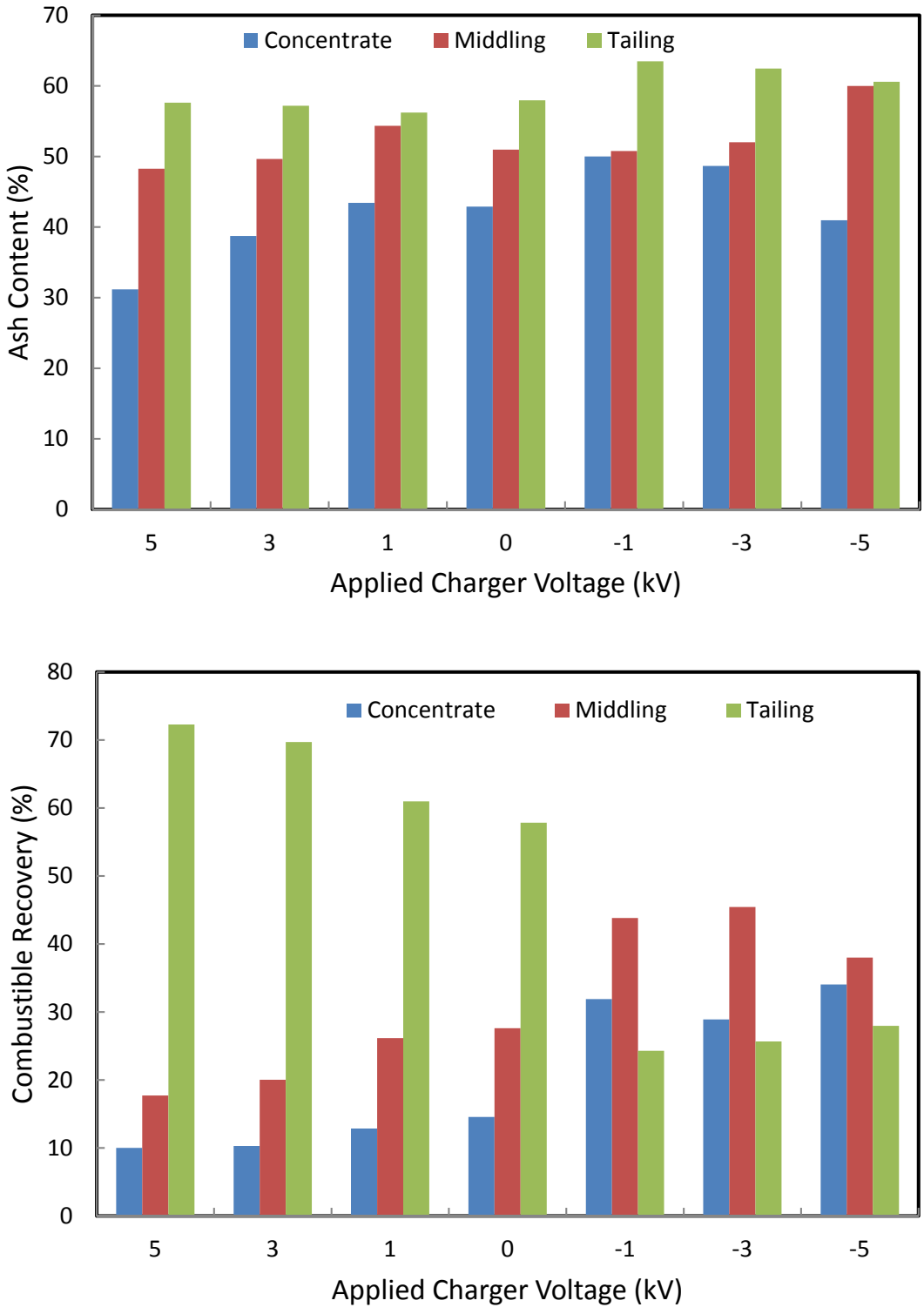

Figure 5.3. Influence of the applied charger voltage on the coal-silica mixture RTS separation: (a) product ash distribution and (b) product recovery distribution.

5.3.4. Injection air rate

The injection air was a compressed air that introduced downward from the top of the RTS. The purpose of introducing the injection air is to speed up the falling particles when they started falling. The injection air velocity was higher than the initial particle velocity (which was approximately 0 m/s). Thus the air drag on the particle provided an extra downward acceleration. With the effect of the injection air, particle terminal velocity when hitting the rotating charger increased. As such, the particle-charger tribocharging efficiency can be elevated. In this series of tests, the injection air rate was varied from 0.6 m/s to 4.3 m/s to study its effect on the particle tribocharging and then the separation efficiency. The experiment result was given in Figure 5.4. It showed when the injection air rate increased from 0.6 m/s to 4.5 m/s, the concentrate ash content was continuously elevated from 26.88% to 43.24%. It infers that the clean coal particle content in the concentrate under high injection air rate was reduced. It is because the clean coal particles were overcharged under high injection air rate. The clean coal particles rebounded after colliding with the chamber wall and then be wrongly collected in other products. As a result, the coal-silica mixture RTS separation efficiency was deteriorated due to the overcharged clean coal particle caused by high injection air rate. Therefore, lower injection air rate was preferred for producing a better quality concentrate. The optimum injection air rate was found to be 0.6 m/s.

5.3.5. Co-flow air

The co-flow air was introduced downward from the top of the separation chamber. The purpose of introducing the co-flow air was to alleviate turbulent air condition and control particle residence time in the separation chamber. Because the charged particles enter the separation chamber from the center with zero velocity, the downward flowing co-flow air can apply air drag on them that facilitates their vertical acceleration. In this series of tests, the co-flow air rate was adjusted from 1.5 m/s to 2.4 m/s to study its effect on the mixture RTS separation. The experiment result is shown in Figure 5.5. The best quality concentrate was obtained when the co-flow air rate was set at 2.1 m/s. When the co-flow air rate increased to 2.4 m/s, the concentrate ash content was elevated to 29.37%. While when the co-flow air rate dropped to 1.8 m/s or 1.5 m/s, the clean coal ash content increased to 30.57% or 31.16%. The experiment result indicates that too low or too high the co-flow rate was not beneficial for the mixture RTS separation. Because the air flow applied a drag force on the falling particles that influenced their trajectories in the separation chamber, maximize the difference of silica and coal particles horizontal displacements could provide the highest clean coal content in the concentrate. Based on the conclusions from previous studies, too long or too short particle residence time resulted from too low or too high co-flow air rate negatively influences the charged particles separation using the RTS. In the present study, the optimum co-flow air rate was found to be 2.1 m/s to produce the best quality concentrate.

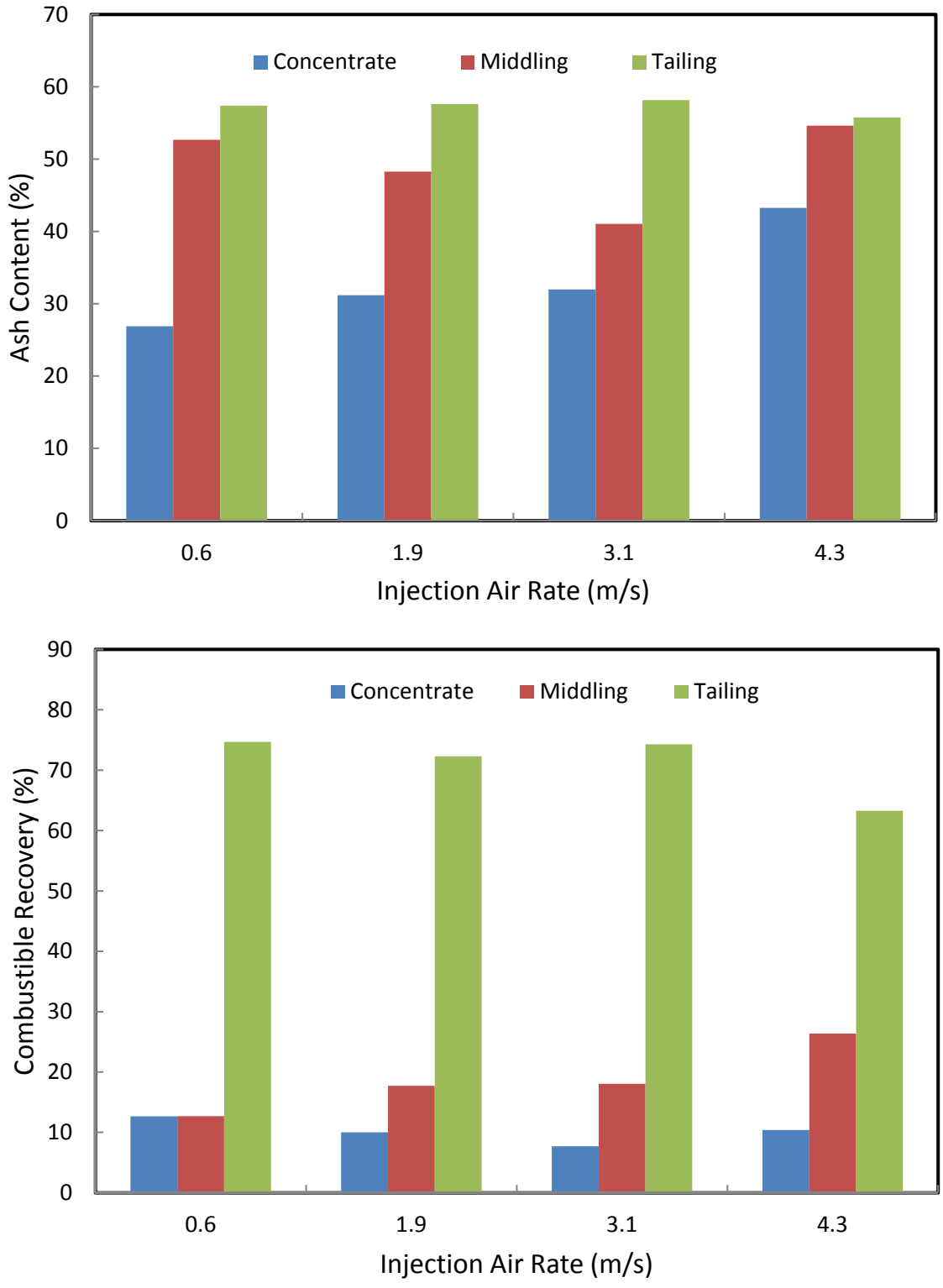

Figure 5.4. Effect of injection air rate on the coal-silica mixture RTS separation: (a) product ash distribution and (b) product recovery distribution.

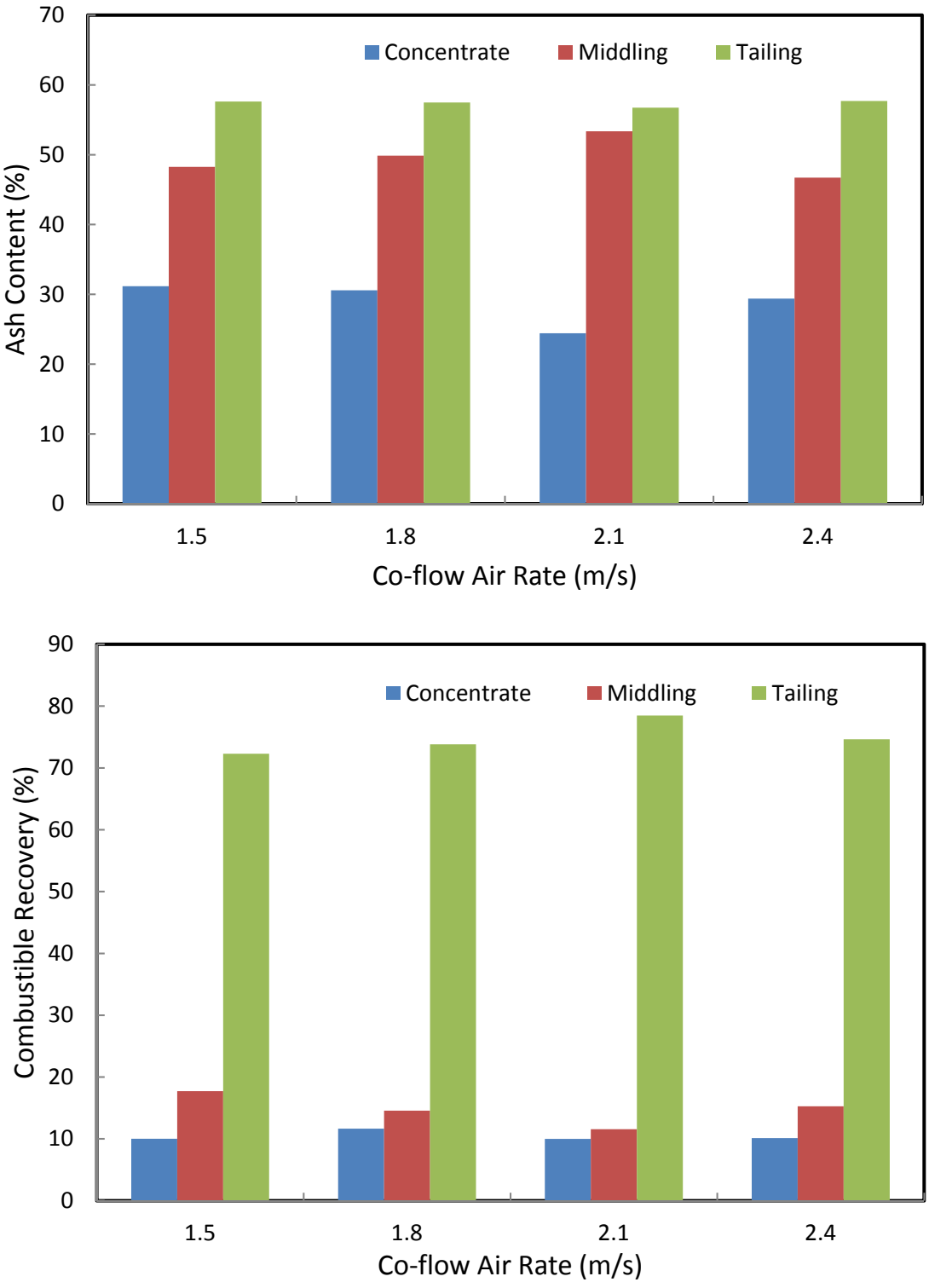

Figure 5.5. Influence of co-flow air rate on the coal-silica mixture RTS separation: (a) product ash distribution and (b) product recovery distribution.

5.4. Multistep treatment stages

From the single factor designed experiment results, the optimum operating conditions using the RTS to produce the best quality concentrate were found as feed rate of 9.1 kg/h, charger rotation speed of 4000 rpm, charger applied voltage of 5 kV, injection air rate of 0.6 m/s, and co-flow air rate of 2.1 m/s. However, the recovery of the concentrate from one stage separation was not high enough. In this series of test, five stages of RTS separation test was conducted on the coal-silica mixture under the optimum separating conditions by retreating the middling and tailing in stages 2-4. It aimed to determine the ideal RTS separation characteristics on the silica-coal mixture. It functions as the release analysis in froth flotation that is used to detect the sample ideal flotation characteristics (Zhang et al., 2017).

In this five stages RTS separation test, one concentrate sample was collected from every separation stage. One middling and one tailing products were obtained in the final separation stage. The experimental flowsheet was shown in Figure 5.6. Totally five concentrates (concentrate 1-5), one middling and one tailing products were obtained in this series of test. The experiment result of this series test was shown in Table 5.3. Figure 5.7 shows the cumulative ash versus the cumulative recovery, which accumulates the products in the order of concentrates (from concentrate 1 to concentrate 5), middling and tailing.

The experiment result shows that the concentrate 1 has the lowest ash content. With the increasing number of retreatment on middling and tailing, the ash content was elevated from concentrate 1 to concentrate 5. Total coal recovery of all the five concentrate products adds up to 39.07%, and the cumulative ash reaches 48.15%. Therefore, the increasing ash content of the clean coal with the continuing retreatment of middling and tailing could be caused by the alternation of coal to silica weight ratio in the feed that affected the particle-particle tribocharging efficiency. The components weight ratio in the feed affected the probability of coal-silica particle collision in the charging chamber thus impacted the charge exchange between them. The prevalence of any single component in the feed reduced its tribocharging efficiency with other particles thus reduced its surface charge density. This conclusion is in consistent with previous contact charging studies related to insulator mixtures (Saeki, 2006; Calin et al., 2008; Miloudi et al., 2013). As such, the variation of feed components weight ratio was related to the particle tribocharging efficiency that finally influenced the RTS separation performance. Since only concentrate 1 and 2 has ash content below 30%. To improve the overall recovery with good concentrate quality, two-stages of RTS separation was suggested.

Table 5.3. Example result of multi-step stages coal-silica mixture RTS separation test.

Product	Individual		Cumulative	
	Ash, %	Yield, %	Ash, %	Recovery, %
Concentrate 1	23.91	6.7	23.91	11.1
Concentrate 2	34.16	5.0	28.33	18.4
Concentrate 3	38.99	4.1	31.09	23.8
Concentrate 4	43.97	3.8	33.60	28.5
Concentrate 5	47.92	3.8	35.90	32.8
Middling	74.07	11.0	48.15	39.1
Tailing	57.67	65.6	54.40	100.0

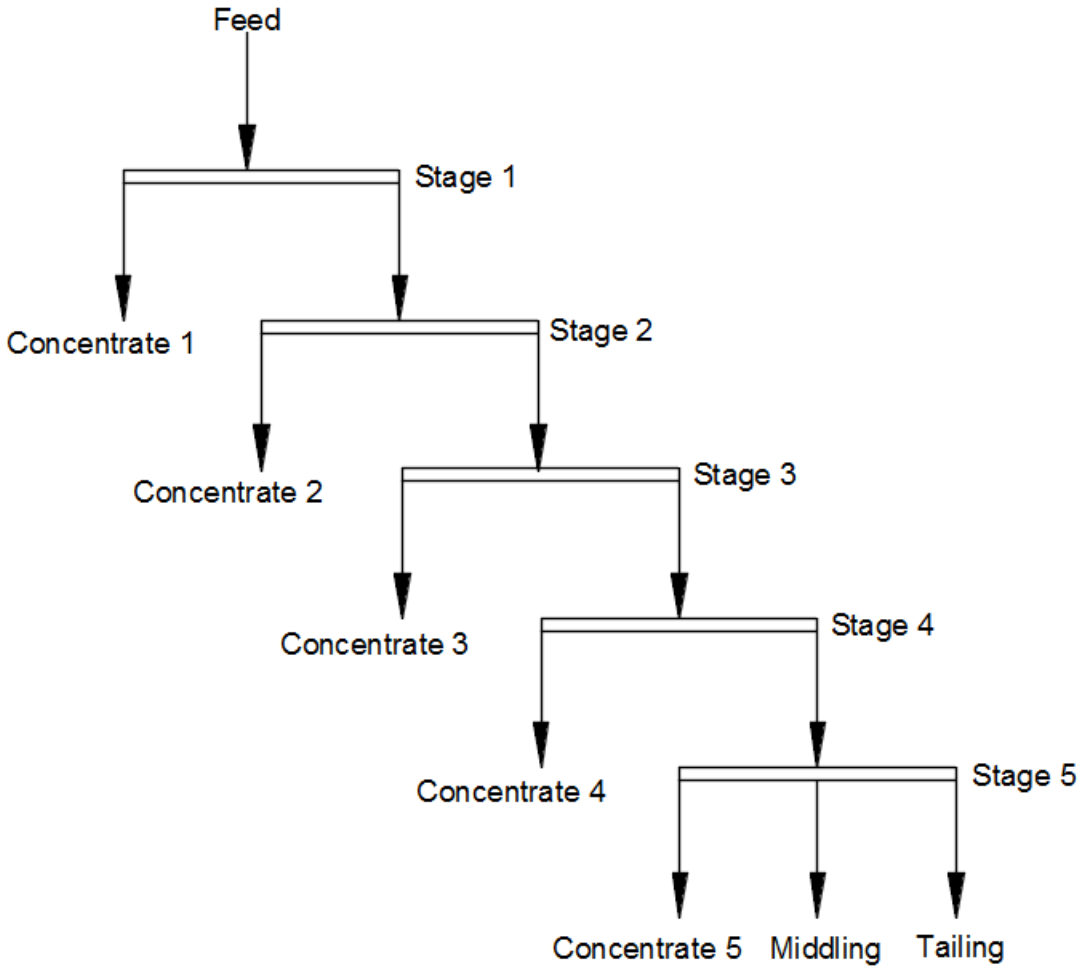

Figure 5.6. Schematic diagram of multi-step stages coal-silica mixture RTS separation test.

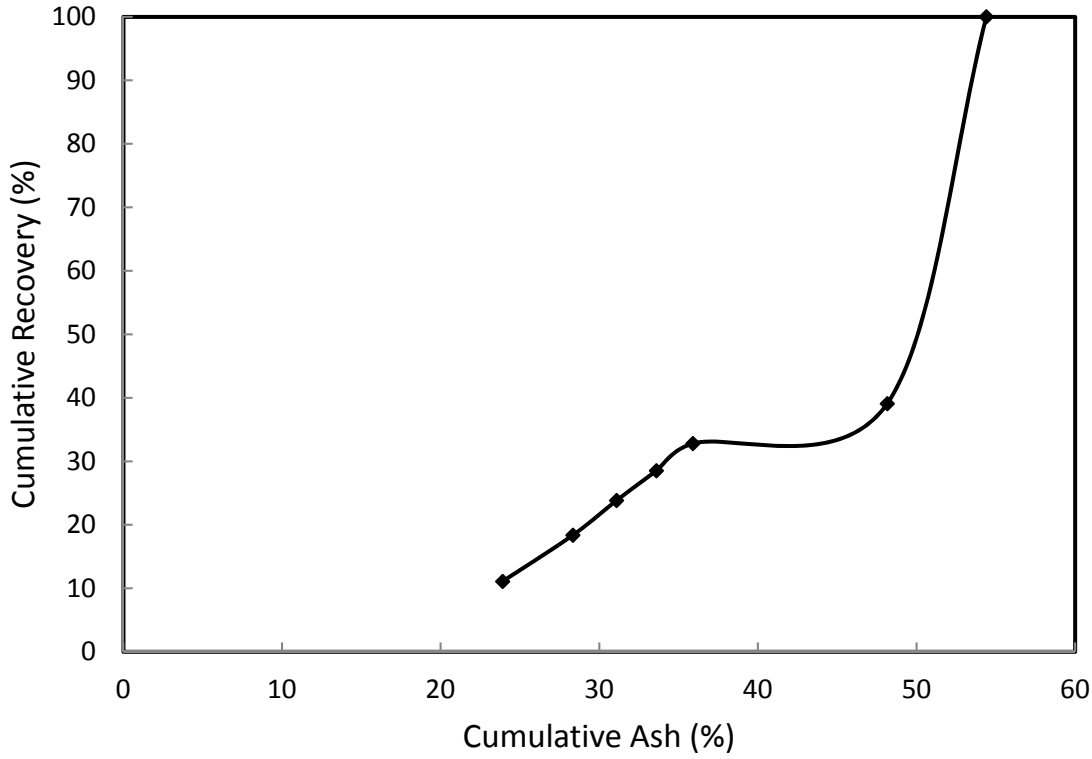

Figure 5.7. Five stages coal-silica mixture RTS separation test.

5.5. Particle charge evaluation

The coal-silica mixture RTS separation test result shows the great potential to remove concomitant silica-based minerals from ROM coal through triboelectrostatic separation. However, the concentrate was found to have high ash content. To further study why the coal-silica mixture could not produce very low ash concentrate, the RTS particle charging test was tried for the answer. One stage RTS particle charging test on the pure silica and the pure coal were conducted to study the charge density distributions of the pure silica and the pure coal. Three products (positively charged particles, weakly charged particles, and negatively charged particles) were obtained in each test.

Because the work functions of copper, coal, and silica have been tested by previous researchers to be 4.65 eV, 5.4 eV and 4.6 eV respectively, the silica was supposed to be charged positively while the coal to be charged negatively after tribocharging with the copper charger. This test discovered how the pure silica and the pure coal particles charged under the optimum operating conditions directly. However, the particle-particle tribocharging effect was still not known. Fundamental analysis on the pure material RTS tribocharging result and the mixture RTS separation result was conducted to derive the silica-coal particle tribocharging effect.

The experiment result of the pure material tribocharging test is shown in Table 5.4. Figure 5.8 shows that under the optimum operating conditions, a majority of the pure silica and pure coal achieved positive charge and a small portion of them obtained a negative charge. This is because when the particles touched the chamber wall, the retained surface charge could be facilitated to

lose to the ground under the effect of the electric field effect in the charging chamber. In this case, this inductive charge effect may even reverse the particle surface charge. Thus practically both the coal and the silica could have positively, weakly and negatively charged particles. The coal and silica particles with similar surface charge densities were probably to be collected in the same product. It could be the reason for the high ash content of the concentrate. The experiment result shown in Figure 5.9 indicates that the RTS could obviously enhance particle tribocharging efficiency compared with the other electronic separator (Dwari and Rao, 2008; Kwetkus, 1998). The experiment result shows the positively charged silica product has higher charge density than positively charged coal product, while the negatively charged coal product has higher charge density than negatively charged silica product. It indicates the silica was more probable to be charged positively while the coal was more probable to be charged negatively. This result obeys the principle that material with higher work function value is easier to be charged negatively. As such, the pure silica and the pure coal were possible to be separated through the RTS separation.

Table 5.4. RTS particle tribocharging test using pure silica and pure coal samples.

Product	Pure Silica		Pure Coal	
	Charge Density, nC/g	Weight, %	Charge Density, nC/g	Weight, %
Concentrate	-1.10	12.6	-3.31	10.9
Middling	-0.12	19.4	-0.67	16.6
Tailing	1.54	68.0	1.26	72.6

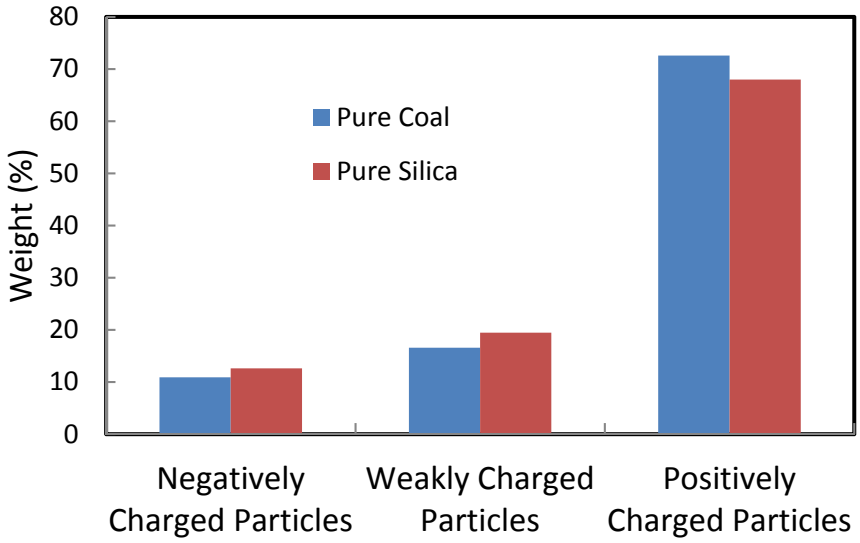

Figure 5.8. Weight distribution based on particle charge density level.

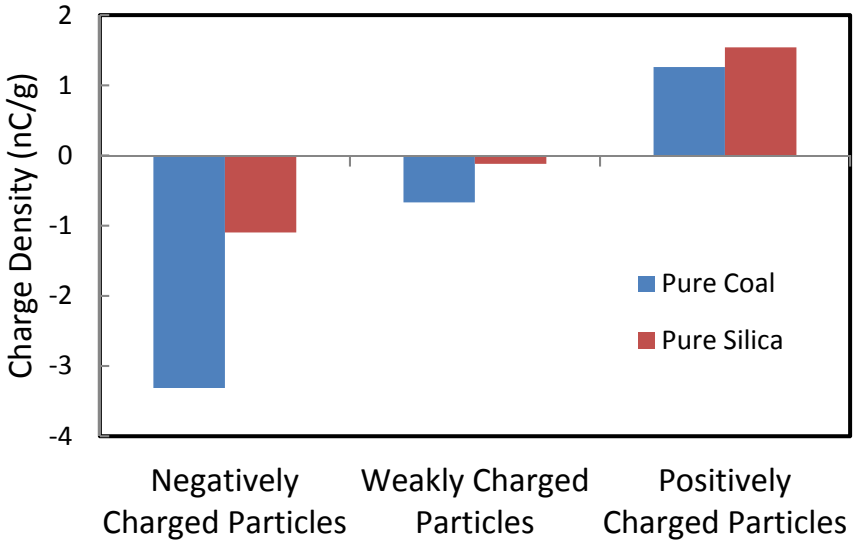

Figure 5.9. Charge distribution based on particle charge density level.

To better understand how the particle-particle interaction influences the particle charge and the separation performance, the particle RTS charging test and the RTS separation result were investigated in combination. Previous developed mathematical speculations were employed based on current experimental conditions. Because the pure coal used in the coal-silica mixture has a composite ash content of 4.3%, the calculated clean coal percentage in the concentrate 1 with a total ash content of 23.91% is 79.51%. Considering the total weight percentage of concentrate 1 is 6.65%, the weight percentages of pure coal and pure silica respect to their weights in the feed were 10.58% and 2.72% respectively. The geological average diameter of pure coal and pure silica was 0.387 mm. The residence time of the pure coal and the pure silica in the separation chamber were 0.1891 s and 0.1920 s, which was calculated according to the experiment rig configuration and operating parameters. The calculated horizontal displacements of pure coal and pure silica corresponding to the surface charge densities are shown in Table 5.5. The particle horizontal displacement versus the surface charge density is shown in Figure 5.10. The calculation result showed when the particle geological mean size was 0.387 mm, the horizontal displacement difference between pure coal and pure silica with the same surface charge densities was negligible. As a result, the difference of the pure coal and the pure silica weight percentages in concentrate 1 was mainly caused by their surface charge density differences.

Table 5.5. Calculated particle horizontal displacement corresponding to particle surface charge density.

Material	Particle Charge density, nC/g	Total Time, s	C_d	Reynold Number	Displacement, mm
Pure Coal	-6	0.1891	4.2	1000	51.3
	-5	0.1891	4.2	1000	42.9
	-4	0.1891	4.2	1000	34.4
	-3	0.1891	4.2	1000	25.9
	-2	0.1891	4.2	1000	17.3
	-1	0.1891	4.2	1000	8.6
	-0.5	0.1891	4.2	1000	4.3
Pure Silica	-6	0.1920	4.2	1000	53.5
	-5	0.1920	4.2	1000	44.6
	-4	0.1920	4.2	1000	35.7
	-3	0.1920	4.2	1000	26.8
	-2	0.1920	4.2	1000	17.9
	-1	0.1920	4.2	1000	9.0
	-0.5	0.1920	4.2	1000	4.5

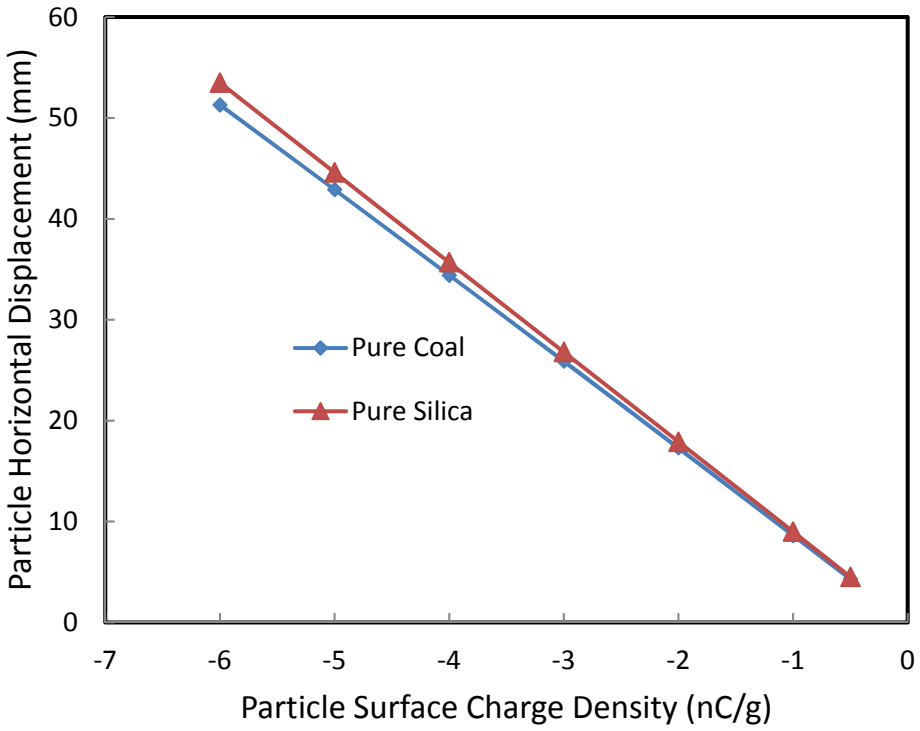

Figure 5.10. Pure coal and pure silica particle horizontal displacement corresponding to surface charge densities.

Since the splitters position below the separation chamber was fixed, the negatively charged particles are collected in the concentrate if its horizontal displacement was larger than 7.7 mm. From the relationship between the particle surface charge density and the horizontal displacement, the critical surface charge densities for the pure coal and the pure silica to be collected in the concentrate are -0.8867 nC/g and -0.8560 nC/g respectively. According to the charging chamber design, the particle-charger tribocharging effect is the primary charging mechanism while the particle-particle contact is minor. It is appropriate to assume that the mean charges of the total particle population of the pure materials and the pure material in the mixture were identical. The mean charge of the pure coal and the pure silica were 0.4433 nC/g and 0.8853 nC/g. As such, the only variable need to be determined was the standard deviation. The method to derive the standard deviations for the pure coal and the pure silica in the mixture was to make full use of the concentrate 1 components mass concentrations and the particle horizontal displacement. Based on an algorithm that has been developed from the previous section, the particle population horizontal displacement probability can be calculated using the particle population charge distribution. Because the splitter was placed at 7.7 mm away from the center, the particle has displacement larger than 7.7 mm was collected in the concentrate. The threshold surface charge density to reach 7.7 mm horizontal displacement for the pure coal particle was -0.8867 nC/g and for the pure silica particle is -0.8560 nC/g. Thus the integration of the particle charge density distribution from negative infinity to -0.8867 nC/g must equal the mass component in the concentrate 1 (10.58% for coal and 2.72% for silica). To compare the pure coal and the pure silica particle charge distributions as a pure material and as a component of the coal-silica mixture after the tribocharging process, the calculated standard deviations are shown in Table 5.6.

Table 5.6. Calculation result of particle population charge distribution parameters according to RTS particle separation result.

Parameter	Pure Material Tribocharging		Coal-Silica Mixture Tribocharging	
	Pure Coal	Pure Silica	Pure Coal	Pure Silica
Mean Charge, nC/g	0.4433	0.8853	0.4433	0.8853
Standard Deviation, nC/g	2.2472	1.0059	0.8853	1.1591

The significant information gained from this comparison is the coal-silica particle tribocharing effect, which is almost impossible to be directly measured and quantified. Among these three tests, the only variable was the feed material. A reasonable assumption that the silica-silica interaction and coal-coal interaction did not cause the charge exchange between them; in the other word, only the coal-silica interaction caused a charge transfer. This is the intrinsic reason for the experiment result that was different from the prediction derived from the pure material tests. The particle-particle tribocharging effect could be estimated by measuring the coal and the silica particle population distributions change between using as a pure material and using as a component in the mixture. The pure coal and the pure silica particle population charge distributions using individual pure materials and a mixture of components are shown in Figure 5.11.

From the influence of coal-silica interaction on the pure coal particles charge distribution, the particle-particle contact greatly reduced the particle charge distribution. Since the shape of the particle charge distribution approaches the center, it infers that the coal-silica interactive effect results in a less charged coal. The finding may be due to the charge leakage or the neutralization of coal particle surface charge, especially the highly charged coal particles after the coal-charger contact. According to their relative positions in the electrostatic series, the contact between the coal and silica could lead to an electron transfer from silica to coal. In this case, the coal would be more negatively charged. However, the experiment result shows an opposite trend. This is because the coal-silica contacting interface had big potential difference caused by accumulated static charge before contact, but the interactive effect was not strong enough. As a result, the contacting surface potential difference decreased. It means the coal particle lost some surface charge at the coal-silica interactive incident, especially the highly charged coal particles. Particle discharge phenomenon has been reported to be a key factor controlling particle final surface charge (Duke and Fabish, 1976; Matsuyama and Yamamoto, 1995). Therefore, during the RTS particle tribocharging process, the coal particle charge distribution was negatively impacted by the coal-silica tribocharging that harmed RTS separation efficiency. Less pure coal particles had enough horizontal displacement and then collected in the concentrate, which raised the concentrate ash content. It partially explained why the concentrate 1 had high ash content.

As to the pure silica particle charge distributions change, the result shows the coal-silica interactive effect was opposite compared with the pure coal. The pure silica particle charge distribution becomes wider as a component in the coal-silica mixture. It infers that the coal-silica particle collision tribocharging assisted the pure silica in generating more negatively and positively charged particles. The appearance of more negatively charged silica particles resulted from the electrons transfer from the highly negatively charged coal particles to the silica particles. When the voltage potential difference between the contacting surfaces was larger than their Fermi level difference, the electron transfer direction was reversed. It resulted in the charge reduction on coal particle surface and the charge accumulation, negative charge, on silica particle surface. The more positively charged silica particles should come from the contact between weakly charged coal and silica particles. The reason for this phenomenon lies in the surface states difference

causing charge transfer, which was related to material surface electronic properties (Bardeen, 1947; Fabish and Duke, 1977). The surface states available for charge transfer in coal-silica contact should be larger than the copper-silica contact that the electron transfer efficiency from silica to coal could be higher than the efficiency from silica to copper under the same Fermi level difference. As such, some silica particles preferred to lose more electrons through the coal-silica contact. Therefore, the coal-silica contact expanded the pure silica particle charge distribution, which led to more silica particles collected in concentrate 1. This is the other reason to explain the high ash content of concentrate 1.

To evaluate the coal-silica particle tribocharging effect more precisely, the calculations of the loss of electrons on the highly negatively charged pure coal particles and the gain of electrons on the highly negatively charged pure silica particles were performed. Because they indicate that the portion of the coal particles failed to be collected and the portion of silica particles wrongly collected in concentrate 1, it shows the effect of the coal-silica contact charging. The calculation results showing the thresholds for initiating particle-particle charge exchange and the quantities of charge loss/gain are shown in Table 5.7.

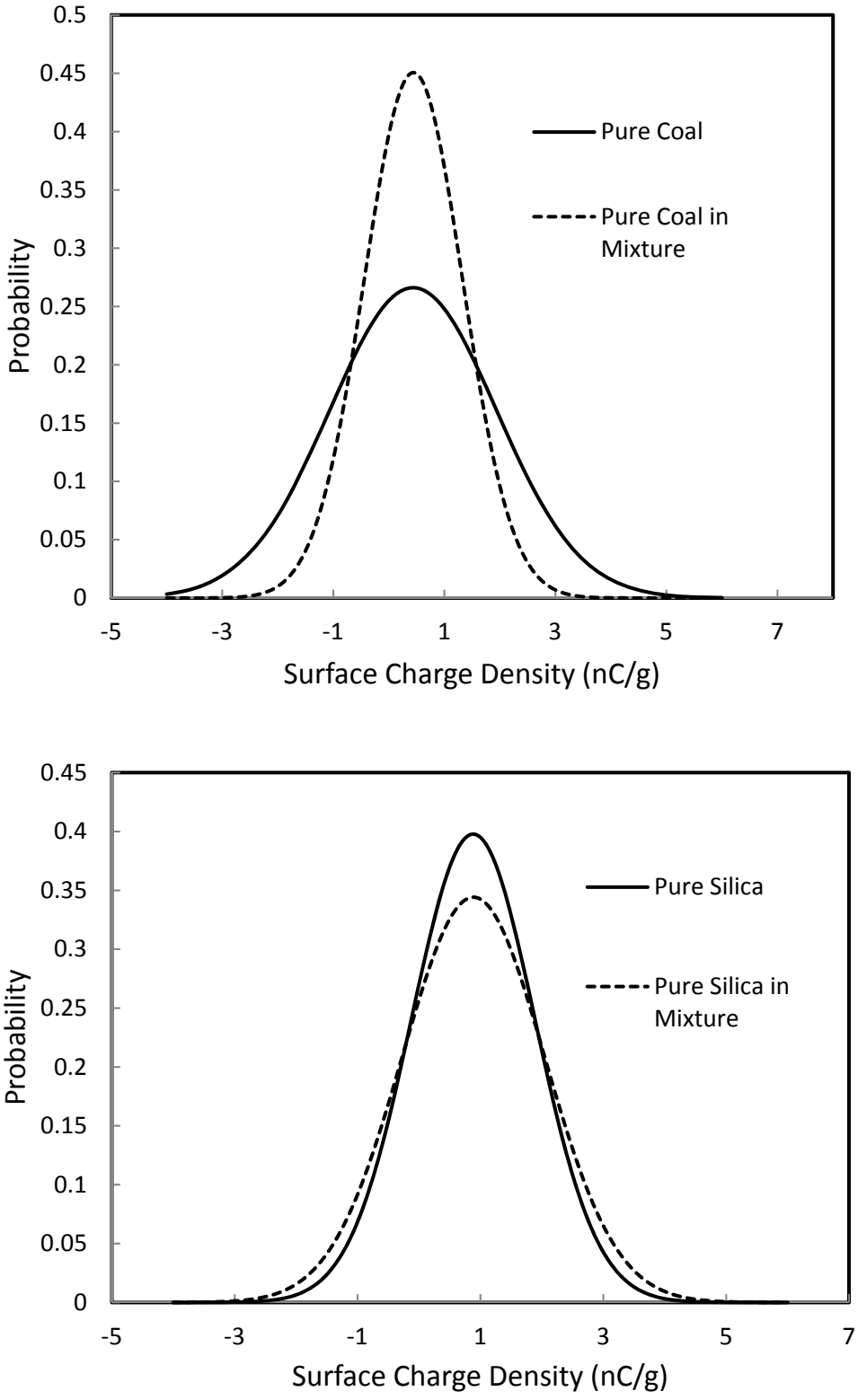

Figure 5.11. Particle population charge distribution comparison between the pure material and the pure material in the mixture: (a) pure coal and (b) pure silica.

Table 5.7. Mathematical calculation for the particle population charge change.

Material	Negatively Charged Particles		Positively Charged Particles	
	Threshold for Charge Change, nC/g	Total Charge Density Change, nC/g	Threshold for Charge Change, nC/g	Total Charge Density Change, nC/g
Pure Coal	-0.8710	0.5449	1.7600	-0.7315
Pure Silica	-0.1920	-0.0438	1.9640	0.1044

The calculation result shows in the region of strongly negatively charged particles, the pure coal particles with charge density larger than -0.8710 nC/g lost electrons and the total electron density loss was 0.5449 nC/g. Additionally, the pure silica particles with particle charge density larger than -0.1920 nC/g started to gain a negative charge, and the total charge density gain was 0.0438 nC/g. In the region of strongly positively charged particles, the pure coal particles with charge density larger than 1.7600 nC/g gained electrons with the cumulative charge density change of 0.7315 nC/g. The pure silica particles with surface charge density larger than 1.9640 nC/g accumulated positive charge with a total density gain of 0.1044 nC/g. This calculation shows when using the mixture feed, there were less pure coal particles and more pure silica particles collected in the concentrate 1, which caused the deterioration of concentrate quality. However, less pure coal particles and more pure silica particles were collected in the tailing, which was beneficial for removing the silica minerals from the feed coal. As such, the RTS separation could be a very good option for the silica-rich coal ash rejection.

5.6. Summary

In this study, the RTS was tried to beneficiate the coal-silica mixture, which is a model study for RTS separation of silica-rich coal. It provided a new option for the dry processing of silica-rich coal within 0.15 - 1 mm. Different charged particles were separated into three products based on their surface charge quantity and/or polarity.

Five operating parameters (feed rate, charger rotating speed, applied charger voltage, injection air rate, and co-flow rate) were selected to study their influences on the coal-silica mixture RTS separation efficiency individually. Single factor experiment design was used to pursue the optimum operating condition. The best quality concentrate can be produced when using the feed rate of 9.1 kg/t, charger rotating speed of 4000 rpm, applied charger voltage of 5 kV, injection air rate of 0.6 m/s and co-flow rate of 2.1 m/s.

A five-stage RTS separation under optimum operating conditions by retreating the combined middling and tailing from the previous stage was studied to depict the ideal RTS separation characteristics on coal-silica mixture. Two-stage triboelectrostatic separation was preferred to enhance the total combustible recovery (18.37%) with acceptable combined concentrate ash content (28.33%).

RTS particle tribocharging test was conducted on the pure coal and the pure silica particles respectively to search the answer why the concentrate ash content cannot reach a low value from the fundamental perspective. The pure coal and the pure silica charge density after RTS separation was measured to estimate their individual particle charge density distribution. Combining the pure material tribocharging test result and the mixture particles RTS separation result, the effect of coal-silica contact was indirectly derived. The comparison of charge density distributions between using as a pure material and using as a mixture component for coal and silica shows that the pure coal particles charge distribution shrunk while the pure silica particles charge distribution expanded. The charge transfer between the coal and silica particles during their contact was responsible for this phenomenon. Additionally, due to the physical properties (particle size, density) of the silica and the coal used in this study, they have similar horizontal displacement after separation if they were similarly charged. It indicates that the surface charge distribution dominates the RTS separation efficiency. The thresholds for the particle-particle charge exchange and the charge exchange density quantities can be evaluated based on the particle charge density distributions change, which is caused by the coal-silica contact. As a result, less pure coal and more pure silica particles were collected in the concentrate, which deteriorated the concentrate quality. However, less pure coal and more pure silica particles were collected in the tailing product, which was beneficial for removing the ash content. Therefore, the RTS can be a good alternative for the silica-rich coal ash rejection.

6. RTS upgrading of low ash coal

6.1. Introduction

Coal is an important fossil fuel that supports the social development. It provides the raw material and the energy that powers the production of many industries. Coal can be classified as coking coal for use in steel production or thermal coal for electricity generation. With the depletion of petroleum, coal is becoming more important for the global economic expansion especially in developing countries. The coal advantages include a heating value, relatively low production costs, long term storage capabilities and vast worldwide reservation. However, its natural occurrence in the form of a solid limits its application as a fuel. The non-aqueous state of coal increases its transportation cost and prohibits its use in automobiles. Though gasification (Kopyscinski et al., 2010; Irfan et al., 2011; Emami et al., 2012) and liquefaction (Derbyshire, 1989; Vasireddy et al., 2011; Mochida et al., 2013) of coal have been studied for many years. High operating costs and environmental concerns restrict their wide application. Other alternatives of liquified coal have been investigated including coal-water slurries (Mishra and Kanungo, 2000; Ma et al., 2013) and coal-oil mixture (Miyazaki et al., 1982; Kumar Majumder et al., 2006). However, using coal directly in a liquid phase has a critical problem related to the ash-forming mineral matter. The noncombustible material builds up inside the engine and causes an eventual engine failure. As such, an ultra-clean coal having a super low ash content is necessary for successful application as a liquid phase fuel (Cui et al., 2008). Ultra-clean coal with ash content lower than 1% cannot be produced from run-of-mine coal directly. Generally, it can be obtained by demineralizing the low ash coal (<4% ash content) with hydrofluoric acid to remove the mineral contents like the silica base minerals and the metal/nonmetal oxides which are not liberated and separated through conventional mineral processing methods (Steel and Patrick, 2001; Wijaya et al., 2011; Zhang et al., 2014). The ability to produce low ash coal using physical cleaning methods has been previously investigated. Technologies included as selective flocculation (Song and Valdivieso, 1998), selective agglomeration, and column flotation (Tao et al., 2000; Li et al., 2003).

Based on the data presented in the previous sections, the RTS separator has the potential to produce an ultra low ash content coal concentrate based on surface electronic property differences between the coal and the associated mineral matter. After impact with a rotary charger coated with copper, the coal and mineral matter particles retain different surface charge densities (in quantity and polarity). Next, the differently charged particles are separated in a chamber in the presence of a strong electric field. In this study, the RTS was evaluated for the potential to produce qualified low ash coal (<4% ash content) from an Illinois #5 coal sample consisting of 5.5%±0.1% ash. The evaluation was conducted in two stages designed to identify the optimum operating conditions needed to meet the ash content objective while maximizing coal recovery. In the first stage, a two-factorial design was employed to identify the significant operating parameters and their values. Then, the experiments in the second stage were based on a three-factorial Box-Behnken design which provided the data needed to create surface response profiles and empirical models describing the response variables (i.e., product as content and combustible recovery) as a function of the operating parameters the RTS was tested to assess the ability to continuously produce low ash coal. A fundamental analysis was conducted to explain the influence of the operating parameters on RTS separation efficiency.

6.2. Experimental

The feed material used in this study was low density (sp.gr. <1.50) Illinois #5 Seam coal with an ash content of 5.5%±0.1%. The particle size was finer than 1 mm and coarser than 0.15. Prior to the tests, the coal sample was stored in a drying oven for over 12 hours to ensure a particle surface moisture content less than 2%. The experiments were carried out at a room temperature of 73°F and an atmospheric relative humidity of 40%.

The RTS was modified for the particle charge test by placing three modified Faraday Cages below the separation chamber to directly collect the solid particles after separation. An electrometer was used to measure the surface charge quantity of each product. The configuration of the modified RTS is present in Figure 6.1.

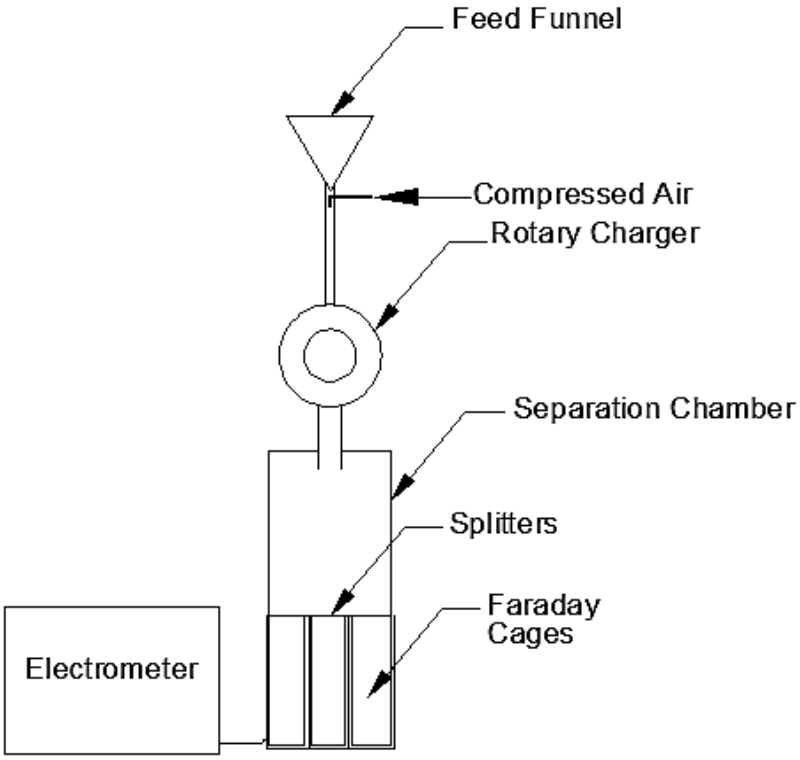

Figure 6.1. The configuration of the RTS using in the test.

Five operating parameters (feed rate, rotary charger rotating speed, applied charger voltage, injection air rate, and co-flow rate) were chosen to study their effects on the RTS separation efficiency. A low-density feed coal sample was fed into the RTS from the top funnel and then accelerated downward into the charging chamber by the injection of air. The particles were statically charged in the chamber due to contact with a rotating charger located inside the charging chamber. An additional charging mechanism was inductive charging under the effect of a strong electric field between the charger and the chamber wall. Afterward, the charged particles entered a separation chamber from the top center and then deviated toward the electrode of opposite charge. The separated particles were collected into three Faraday Cages.

The product charge was measured individually using an electrometer after each test. The product charge density was expressed in the unit of nC/g. The separated products were classified as positively charged particles (*P*), weakly charged particles (*W*) and negatively charged particles (*N*). The maximum absolute particle charge density difference was calculated as $MD=|P-N|$ in nC/g, which was adopted as a new standard to judge the RTS separation efficiency. Since the theoretical basis of the triboelectrostatic separation is the materials' surface electronic properties differences, it is reasonable to regard the product charge density difference as an indication of RTS separation efficiency. Based on the conclusions from the previous study, the higher *MD* indicates larger surface charge density difference between the pure and the impure coal particles, which means better RTS separation efficiency. The purpose of this study was to identify the optimum operating condition that can generate maximum *MD,* where the best RTS separation efficiency can be obtained.

Two stages of experiments were designed for pursuing the optimum operating conditions. The first stage of experiments used a two-factorial design to screen the five operating factors based on their relative levels of significance measured by the *MD* value. The results from the first stage were used to identify three parameters having the greatest influence on the *MD*. Next, the significant factors were more thoroughly evaluated in the second stage of experiments using a three-factorial Box-Behnken design with narrowed parameter value ranges to locate the optimum operating conditions. After determining the optimum operating conditions, three repeat tests were conducted to confirm the optimum results and experiment error. A fundamental analysis was performed to explain the detailed effect of each operating parameter.

6.3. Experiment results and discussion

6.3.1. Two-level parametric screening

In the two-level test program, upper and lower values for each operating parameter were selected based on the findings from the previous test. The operating ranges for every parameter were set as feed rate of 1 to 14 kg/h, charger rotating speed of 2000 to 5000 rpm, charger applied charger voltage of -5 kV to 5 kV, injection air rate of 0.6 to 4.3 m/s and co-flow air rate of 1.5 to 2.4 m/s. A total of eight experiments were required to meet the objectives for the first stage of experiments. The test design and results obtained from the first stage of experiments are shown in Table 6.1 and a statistical analysis of the data provided in Table 6.2. A linear statistical model was employed to correlate the *MD* values with the operating parameters.

Table 6.1. Two-level factorials design and experiment result.

Test Number	Feed Rate, kg/h	Charger Rotating Speed, rpm	Applied Charger Voltage, kV	Injection Air Rate, m/s	Co-flow Rate, m/s	*MD* , nC/g
1	14	5000	-5	4.3	2.4	3.46
2	1	2000	-5	4.3	1.5	6.00
3	1	2000	5	0.6	2.4	4.47
4	1	5000	5	4.3	2.4	4.40
5	14	5000	5	0.6	1.5	5.38
6	14	2000	-5	0.6	1.5	4.73
7	1	5000	-5	0.6	2.4	4.29
8	14	2000	5	4.3	1.5	4.77

Table 6.2. ANOVA and effect test result of the two levels screening design experiment.

Source	DF	Sum of Squares	Mean Square	F Ratio	Prob>F
Feed Rate	1	1.5194	1.5194	19.23	0.0483
Charger Rotating Speed	1	0.0850	0.0850	1.08	0.4086
Applied Charger Voltage	1	0.0365	0.0365	0.46	0.5671
Injection Air Rate	1	0.0072	0.0072	0.09	0.7912
Co-flow Rate	1	2.9756	2.9756	37.66	0.0255
Model	5	3.8475	0.7695	9.73	0.0957
Error	2	0.1580	0.0790		
C. Total	7	4.0006			
R^2	0.9605		Adj R^2	0.8619	

A single-tailed *F*-test was selected to evaluate the robustness of the model, and the significance of the operating parameters based on the significance level of 0.05, the hypothesis for the *F*-test is:

H_0: *The variation*(s) *of the five operating factor*(s) *have no influence on the test observations*;

H_1: *The variation*(s) *of the five operating factor*(s) *have influence on the test observations*;

The *F* test on the individual factors shows the feed rate and the co-flow rate were significant individual operating parameters influencing the maximum product charge density difference. They have Prob>F values smaller than 0.05, which fall into the rejection area. The injection air rate was the most insignificant factor due to its highest Prob>F value, which falls in the acceptance area. The influences of the factors can be ranked according to their Prob>F values based on an ascending order. This ranking derived from statistical quantities provides the indication about which parameter exerted more effect (low Prob>F value) on the experiment result. The statistical analysis shows the operating parameters included in the model can be well correlated with the experiment result, the *MD* value, with an R^2 value of 0.9605. It indicates that the variation of the operating parameters can significantly influence the maximum product charge density differences. However, the adjusted R^2 value of 0.8619 is much smaller than the R^2 value, which means there were some insignificant factors included in this statistical model. The Prob>F

value of 0.05 was used as the threshold for a factor to be significant in the *F* test. As to the model used in this analysis, it was not good enough under the significance level of 5% since its Prob>F value is 0.0957. It shows the statistical model needs modification to elevate the model significance level and shrink the difference between the R^2 and the adjusted R^2. As such, the forward stepwise method with the standard stopping rule of minimum BIC (Bayesian information criterion) was adopted to adjust the original statistical model. Only the most significant factors impacting the *MD* value were included in the modified model. The ANOVA of the modified model is shown in Table 6.3.

Table 6.3. ANOVA and effect test result of the modified model based on the two levels screening designed experiment result.

Source	DF	Sum of Squares	Mean Square	F Ratio	Prob>F
Feed Rate	1	1.5194	1.5194	30.14	0.0005
Charger Rotating Speed	1	0.0850	0.0850	1.69	0.2639
Co-flow Air Rate	1	2.9756	2.9756	59.02	0.0002
Model	3	3.8039	1.2680	25.15	0.0047
Error	4	0.2017	0.0504		
C.Total	7	4.0006			
R^2	0.9497		Adj R^2	0.9119	

The modified model included the comparatively significant factors (feed rate, charger rotating speed, and co-flow air rate) affecting the maximum product charge density difference. After obviating the two insignificant factors, the R^2 of the model drops a little from 0. 9605 to 0.9497. It shows the operating parameters variation still have strong correlations with the *DM* variation. The adjusted R^2 rises from 0.8619 to 0.9119. The convergence between R^2 and the adjusted R^2 infers that the model did not include too much redundant input in the model, which can more accurately correlate the included parameters with the experiment response. The reason for the elimination of injection air rate could due to the high particle-charger tribocharging basis provided by the rotating charger. In other words, the increased particle-charger interactive effect caused by a higher injection air did not significantly improve the particle tribocharging efficiency. The weak effect of applied charger voltage indicates the limit effect of the direction of the electric field between the charger and the chamber wall in maximizing the product charge density difference. It infers that the net charges transfer caused by inductive charging from the external electric field in both directions were similar.

After the modification of the statistical model, the co-flow air rate still has the most significant effect with the Prob>F value of 0.0002. The effect of feed rate follows up with Prob>F value of 0.0005. The charger rotation speed was not proved to be a significant individual effect according to its *F* test result. However, the modified model containing this parameter indicates that its effect cannot be forgone to keep the statistical model significant. Additionally, it is very probable to have some significant interactive effect with other operating parameters in influencing the *MD* values. As a result, the operating parameters of feed rate, charger rotating speed and co-flow rate were disclosed to most significantly influence the maximum product charge density difference from the parameter screening test, which were studied further in detail in the second stage experiments. Their operating ranges were narrowed and nearer to the levels which lead to a larger *MD* value. The insignificant factors were fixed at the applied charger voltage of -5 kV and the injection air rate of 0.6 m/s, which produced higher *MD* value.

6.3.2. Three-level factorial Box-Behnken design

In the three factors three levels Box-Behnken experiment design, the charger rotating speed, co-flow rate and feed rate were used as variables. Their operating ranges were shrunk compared with the operating ranges used in the screening test and approached the levels that favor maximizing the *MD* value. The selected testing points for the charger rotating speed were 3000, 4000, 5000 rpm, for the co-flow rate were 1.5, 1.8, 2.1 m/s, and for the feed rate were 4.5, 9.0, 13.6 kg/h. The other two insignificant factors omitted from the screening test were fixed as described before. This experiment design was aimed to locate the optimum operating condition that can maximize the product charge density difference. There were three repeated tests on the center point for experiment error evaluation. The experiment design and the experiment result are shown in Table 6.4.

Table 6.4. Three factors three levels Box-Behnken experiment design and experiment result.

Experiment No.	Charger Rotating Speed, rpm	Co-flow Air Rate, m/s	Feed Rate, kg/h	Maximum Charge Density Difference, nC/g
1	4000	1.5	13.6	6.07
2	5000	2.1	9.0	6.35
3	4000	1.8	9.0	5.47
4	5000	1.5	9.0	4.97
5	4000	2.1	13.6	4.05
6	4000	1.5	4.5	4.06
7	4000	2.1	4.5	4.23
8	4000	1.8	9.0	5.38
9	3000	1.8	4.5	4.20
10	3000	1.5	9.0	4.84
11	5000	1.8	13.6	5.66
12	5000	1.8	4.5	4.16
13	3000	2.1	9.0	5.57
14	3000	1.8	13.6	4.25
15	4000	1.8	9.0	5.31

The average *MD* value from the Box-Behnken design experiments was larger than the one from the screening designed tests. It indicates the strategy of the operating factors and the operating ranges selections was a success. The repeated tests on the center point show that the *MD* values standard deviation was 0.08 nC/g. The experiment error was less than 5%, which approved good experiment stability. As a result, the variation of the *MD* across all the tests can be considered to be insulated from non-operating factors. The *F*-test was used to validate the robustness of the model and the significance of the operating parameters at the significance level of 0.05. The hypothesis of the statistical test was stated as below:

H_0: *The variation*(s) *of the three operating factor*(s) *have no influence on the test observations*;

H_1: *The variation*(s)*of the three operating factor*(s) *have influence on the test observations*;

A quadratic model was used for the statistical analysis. The ANOVA and the effect test considering the parameters individual effect and the interactive effects were shown in Table 6.5. In this table, letters A, B, C represent the charger rotation speed, co-flow air rate, and feed rate respectively. The combination of the letters denotes the interactive effect between parameters. The square of a letter signifies the quadratic effect of parameters.

Table 6.5. ANOVA and effect test results of the Box-Behnken design experiment.

Source	DF	Sum of Squares	Mean Square	F Ratio	Prob>F
A	1	0.6600	0.6600	1.6600	0.2539
B	1	0.0070	0.0070	0.0180	0.8999
C	1	1.4300	1.4300	3.6000	0.1163
AB	1	0.1100	0.1100	0.2700	0.6279
AC	1	0.5300	0.5300	1.3300	0.3010
BC	1	1.2200	1.2200	3.0800	0.1395
A^2	1	0.0001	0.0001	0.0003	0.9875
B^2	1	0.0060	0.0060	0.0150	0.9067
C^2	1	2.5400	2.5400	6.4000	0.0526
Model	9	6.5100	0.7233	1.8200	0.2635
Error	5	1.9800	0.3960		
C. Total	14	8.4900			
R^2	0.7664		Adj R^2	0.3458	

The statistical model has an R^2 value of 0.7664, which implies the quadratic model in use is not perfect enough. This is because to ensure the efficiency and practicability of the statistical model, in which high-level parametric effects were not included in the model as a compromise. The adjusted R^2 is 0.2458, which is much smaller than the R^2. It infers that some insignificant variables are included in the model that brings disturbing noises. The *F* test on the model shows the *Prob>F* value is 0.2539, which is insignificant according to the test assumptions. As such, a forward stepwise method using the standard stopping rule of minimum BIC was applied on the initial model to elevate the model significance. The statistical analysis of the modified model is shown in Table 6.6.

Table 6.6. ANOVA and effect test result of the modified model of the Box-Behnken Design Experiment.

Source	DF	Sum of Squares	Mean Square	F Ratio	Prob>F
B	1	1.07	1.07	3.28	0.1004
C	1	2.03	2.03	6.21	0.0318
BC	1	1.22	1.22	3.74	0.0820
C^2	1	2.59	2.59	7.91	0.0184
Model	4	5.22	1.31	3.99	0.0346
Error	10	3.27	0.33		
C. Total	14	8.49			
R^2	0.6146		Adj R^2	0.4604	

The modified model is significant at a significance level of 5% that has *Prob>F* value of 0.0346, which has a big improvement compared with the initial model. It shows the variables contained in the modified model have a direct connection with the *MD* value. The difference between the R^2 and the adjusted R^2 shrinks to 0.1542, which indicates that the noise influence from insignificant factors has been effectively suppressed. The individual effect of feed rate (*C*) and the square of the individual effect of feed rate (C^2) were the most significant factors in the modified model. It infers that within the operating ranges of the listed factors, the feed rate could exert the hugest impact on the *MD* values. A logical explanation for this result is that the particle-particle tribocharging effect more effectively impacted particle final charge density distribution. It is because the feed rate controlled the particle population density inside the charging chamber that affected the particle-particle contact charge. Though the particle-charger contact had established a highly efficient particle charging basis, the particle-particle contact caused the electron transfer between the organic component and the concomitant minerals leading to more significant impact on the *MD* value. The elimination of the effects of charger rotation speed (*A* and A^2) and its associated interactive effects (*AB* and *AC*) in reaching the modified model shows that varying charger rotating speed has limited effect on particle tribocharging efficiency change. It infers that the minimum charger rotating speed has already provided a high efficient particle-charger contact charging effect. Continuously improving the charger rotation speed did not incur corresponding particle tribocharging efficiency improvement that limited its effect on the *MD* values. Its removal illustrated that the variation of the *MD* values resulted from the particle-charger tribocharging effect was not primary. It underpinned the fact that the *MD* variation was more integrated with the particle-particle tribocharging effect.

Although the parametric individual effect of co-flow air rate (*B* and B^2) on the *MD* variation was not significant, the interactive effect between the co-flow air rate (*B*) and the feed rate (*C*) showed significance. Because the feed rate affected the particle tribocharging process while the co-flow air rate impacted the particle separation process, their interactive effect was significant for the RTS separation. Too high co-flow velocity led to an insufficient residence time of the charged particles in the separation process that caused insufficient separation, while too low co-flow velocity resulted in the excessive horizontal displacement of coal particles that escalated the misplacement phenomenon. It is in accordance with a previous finding from the particle RTS separation hydrodynamic analysis; the particles surface charge density distribution should be accompanied by an appropriate separation residence time to achieve the best RTS separation efficiency. The detailed interaction between the co-flow rate and the feed rate is presented in Figure 6.2.

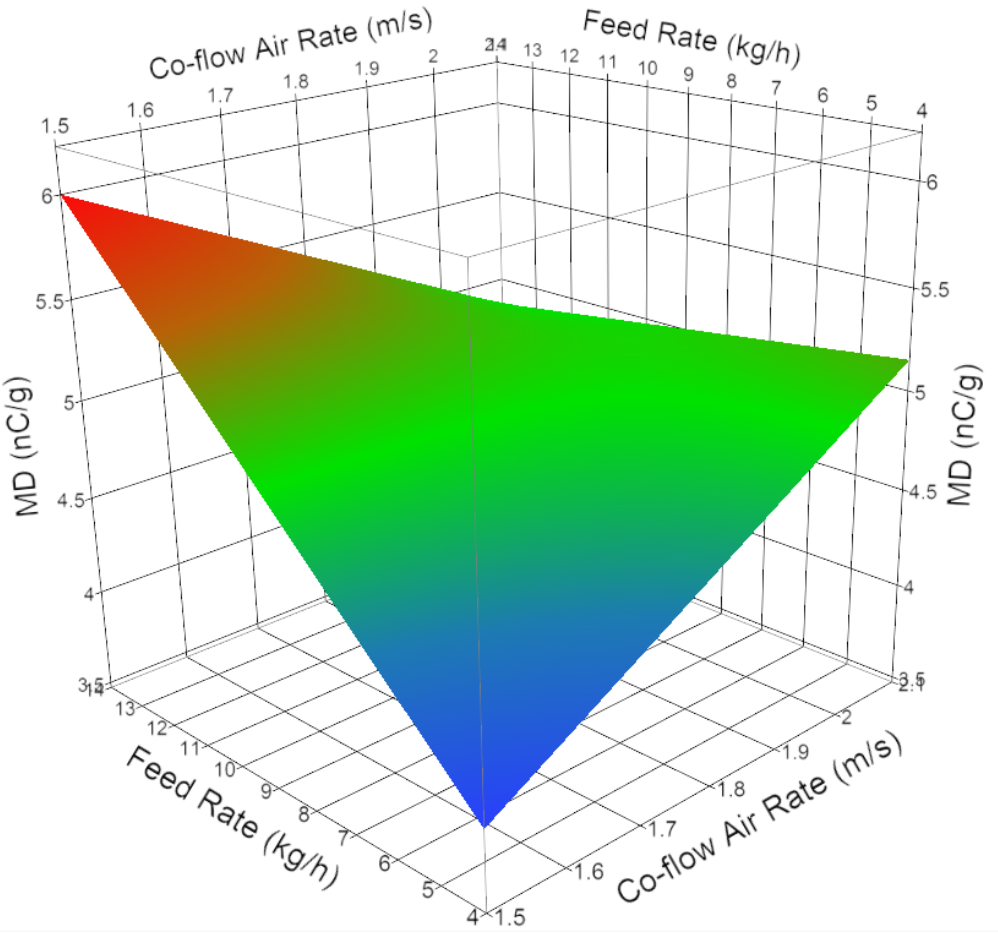

Figure 6.2. The 3D plot of the interactive effect between the co-flow rate (*B*) and the feed rate (*C*).

Previous discussed mathematical speculation about the product charge density distribution and the separation environmental hydrodynamics was applied to analyze the detailed interactive effect between the co-flow air rate (*B*) and the feed rate (*C*). When the feed rate was low, a higher co-flow rate resulted in a larger *MD* value. It infers that there must be some strongly charged particles striking the chamber wall before collection, which is combined with the particle surface charge neutralization or even reversion. Then the *MD* value increasing with the co-flow air rate indicates that strongly charged particles quickly passed through the separation chamber and then be collected.

When the feed rate was high, the trend of the *MD* value influenced by the co-flow rate was opposite compared with when the feed rate was low. Lower co-flow air rate resulted in higher *MD* value, which indicates that the particles need more residence time to achieve a better separation. As such, the particle charge density distribution should be compressed when the feed rate was rising. It provides the evidence that the particle-particle tribocharging effect has a negative impact on the coal particles surface charge density distribution. This result was produced through the neutralization of oppositely charged contacting surfaces (charged mineral patch and organic patch). It is because the particle-particle interactive force was not strong enough to

sustain the separating status of contacting opposite charges. The followed charge relaxation phenomenon constrains the total particle tribocharging efficiency.

With the integration of the previous mathematical analysis into the statistical analysis of experiment result, it becomes clearer about the operating factors in influencing the particle charge and separation. The most significant factor in influencing the particle final charge density is the feed rate. However, it is a negative effect that assists in the particle surface charge neutralization. Because the charger rotation speed provided a high efficient particle-charger tribocharging basis, its variation did not cause a significant impact on the particle charge density distribution hence the *MD* values. The co-flow rate was a critical factor influencing the particle separation process. The environmental hydrodynamic condition should correspond with a particle charge density distribution to achieve optimum separation. Too large or too small of the particle horizontal displacements could deteriorate the RTS separation efficiency.

An empirical model was derived from the statistical analysis of the pure coal RTS separation experiment result to predict the *MD* value base on the operating conditions of co-flow rate (B) and feed rate (C and C^2) and their interactive effect (BC), which is shown below:

$$MD = 3.764 \times B + 1.550 \times C - 0.405 \times B \times C - 0.040 \times C^2 - 5.492 \qquad (64)$$

Combining the Screening test and the Box-Behnken designed test results, the *MD* value could be maximized when the operating conditions were set as the applied charger voltage of -5 kV, injection air rate of 0.6 m/s, charger rotation speed of 4000 rpm, co-flow rate of 1.5 m/s and the feed rate of 11.72 kg/h. Under this condition, the *MD* has an average value of 6.50 nC/g with a standard deviation of 0.17 nC/g. Theoretically, the maximum pure coal RTS separation efficiency could be obtained under this operating condition, and three repeated tests were conducted to evaluate the separation stability. The experiment result, Table 6.7, shows the concentrate ash contents have a mean value of 3.85% with a standard deviation of 0.08%. The recovery of concentrate is 62.97% with a standard deviation of 1.11%. The concentrate quality satisfies the target of producing maximum 4% ash content coal product. It indicates that the RTS could stably produce low ash coal with an acceptable level of experiment error.

Table 6.7. Repeated pure coal RTS separation test based on the optimum operating conditions.

Test Number	Concentrate			Middling			Tailing			*MD*, nC/g
	Wt, %	Charge Density, nC/g	Ash, %	Wt, %	Charge Density, nC/g	Ash, %	Wt, %	Charge Density, nC/g	Ash, %	
1	60.7	6.26	3.83	17.5	3.65	6.74	21.9	-0.44	9.23	6.7
2	62.2	7.20	3.79	16.7	7.04	6.64	21.1	0.79	9.28	6.41
3	62.9	6.95	3.94	17.0	5.14	6.72	20.1	0.56	9.21	6.39

6.4. Summary

The operating parameters of the RTS have different influences on particle tribocharging and/or particle separation processes. *MD* value was selected as a new standard for judging the particle RTS separation efficiency. Better separation of the pure coal particles from the impure coal particles can be reflected by a larger *MD* value, which indicates a better RTS separation efficiency.

The screening test based on the five operating parameters was designed to sort out the comparatively significant factors. The statistical analysis result shows the injection air rate and the applied charger voltage were the two most insignificant factors in influencing the RTS separation efficiency. Hence, they were fixed at 0.6 m/s and -5 kV respectively in the later experiments, which favored generating a higher *MD* value.

The Box-Behnken experiment design was employed to study more comprehensive parametric effects on RTS separation. The charger rotation speed was found to be the most insignificant factor. It signals that the variation of the charger rotation speed could not cause an obvious change in the particle RTS tribocharging efficiency. The minimum charger rotation speed should have already supplied a high efficient particle-charger tribocharging basis, continuing increase in the charger rotation speed could not significantly elevate the RTS separation efficiency.

The feed rate was found to be the most significant factor impacting the *MD* values, both in the first-order and second-order forms. The feed rate determined particle population density inside the charging chamber, which controlled the particle-particle tribocharging efficiency that connected to the particle final surface charge. The interactive effect between the co-flow rate and the feed rate has a significant influence on the *MD* values if the level of significance is relaxed a little to 0.1. This finding is in agreement with the previous mathematical prediction about the particle RTS separation process. The residence time of the charged particles inside the separation chamber was controlled by the ambient air hydrodynamics, which should be adjusted according to the particles charge density distribution for an optimum RTS separation efficiency.

Previously discussed the mathematical analysis of the separation process was incorporated into the statistical analysis of the coal RTS separation experiment data. It aimed to illustrate the precise parametric effect on the RTS separation process. The interactive effect of the feed rate and the co-flow rate explains that a high feed rate was detrimental to maximize the product charge density difference. Though high feed rate causes high coal-silica collision probability, coal-silica interactive effect was not strong enough to sustain the separating status of the original opposite charges on the contacting surfaces. As a result, charge relaxation happened, and the particle final tribocharging efficiency declined.

After finishing two sets of statistically designed experiments, the optimum operating conditions were determined to be as the applied charger voltage of -5 kV, injection air rate of 0.6 m/s, charger rotation speed of 4000 rpm, co-flow rate of 1.5 m/s and feed rate of 11.72 kg/h. Under this condition, the *MD* has an average value of 6.5 nC/g with a standard deviation of 0.17 nC/g. The concentrate has the ash content of $3.85 \pm 0.08\%$ with the recovery of $62.97 \pm 1.11\%$. The RTS can stably produce the low ash coal (<4% ash) with an acceptable experiment error.

7. Conclusion

In this study, the fundamental research on the particle tribocharging dynamics was first conducted. A ceramic cylinder was used to contact charge with a copper plate using rolling and sliding contacts. An oscilloscope was used to record the whole tribocharging process and gauge the signals when charge transfer occurred. The charge transfer between contacting surfaces made of different materials started when the relative interaction began. According to the surfaces electronic properties, exchanged charge stayed on the shallow surface of a ceramic cylinder while injected much deeper inside the copper plate. The exchanged charges on the shallow contacting surfaces were considered neutralized. The net "residual" charge at the interface created an electric field that penetrated into the copper plate and captured the exchanged charges inside the copper bulk. Some exchanged charges inside the copper bulk were not captured that became free charge and escaped away. This conclusion provides a potential quantification method for measuring the charge penetration depth into the conductor during the tribocharging process. In the separation process of the contacting surfaces, the exchanged charges on the separating surfaces attracted each other that made the whole system resemble a capacitor. Molecules in the gap could be ionized that facilitated the charge relaxation. All these characteristics can be reflected by the pulsing signals recorded by an oscilloscope. The last pulsing signal was qualitatively directly related to the particle surface residual charge. A new method for particle surface charge measurement was proposed based on pulsing signal integrated area, which is of extreme use for weak charge measurement.

Particle-copper plate tribocharging parametric study was accomplished in an environmental chamber. The relative humidity, normal force, friction force, and the relative displacement effects on the particle tribocharging were investigated. The normal force, friction force and relative displacement were disclosed to have a positive correlation with particle charge, which indicated that the energy consumption at the interface favored charge transfer. The humidity level has a dual effect on particle charge. When the humidity was extremely low, elevating the relative humidity assisted in forming a thin water layer on the particle surface, which increased the dielectric constant at the gap between contacting surfaces. The thin water film functioned that both facilitated the charge transfer and resisted the exchanged charge leakage. However, when the humidity level was beyond a critical value, continuous enhancing the humidity level formed a thick water film on the contacting surfaces that assisted in dissipating the exchanged charge or even forbidding the charge transfer. A semi-empirical model was developed from the compression model incorporating the experiment data of the parametric study. It provides a more accurate method to estimate particle surface charge corresponding to exact operating conditions.

The surface electronic property influencing particle surface charge was studied using coal and silica chunks. The surface sites available for charge exchange was the material idiosyncrasy, which was found to be more significant than surface area in affecting particle surface charge. Silica can easily achieve a high quantity of charge relative to the coal, even though the total surface area of silica involved in tribocharging was much smaller than the coal. The estimated static surface chargeable sites of silica were about 69 times more than that the coal, which provides the logical foundation for the electrostatic separation of silica-rich coal. Though there is only small coverage of the concomitant minerals (e.g., silica) on a coal particle surface, it can exert an enormous effect in determining the particle final charge.

The influences of particle size on particle charging and particle RTS separation efficiencies were studied using a representative coal sample, which was then sieved into four different size fractions. The total charge of every product after RTS separation was measured directly, which was used in evaluating the particle charge density distribution with the Gaussian distribution assumption. The average charges of different size coal samples show that smaller particles

exposed more surface area for charge exchange that improved the tribocharging efficiency. However, too small particles have a limit particle-charger interactive effect that restricted particle tribocharging efficiency. Smaller particle size results in a wider particle charge density distribution. Mathematical calculation of the particle separation process was implemented according to the separation chamber environmental hydrodynamics. The particle residence time in the separation process was positively correlated with the particle size. The residence time in the separation should coordinate the particle charge density distribution to pursue an optimum RTS separation efficiency. Too short residence time did not allow enough particle horizontal displacement, while too long residence time could cause the strongly charged particles collide the chamber wall before collection. As a result, the optimum RTS separation efficiency is only possible when the separation chamber environment is controlled to fit the particle charge distribution conditions best.

The pure coal and pure silica mixture model sample was used in a model study for the RTS beneficiating silica-rich coal. The effects of operating conditions on the RTS separation of the model feed sample were studied. Single factor experiment design was used to pursue the optimum operating condition. Under the determined optimum condition, a five-stage RTS separation test by retreating the middling and tailing from the previous stage separation was conducted to portray the optimum separation curve obtainable using the RTS. A series of products with ash contents vary from 23.91% to 57.67% were obtained. Two-stage RTS separation on the mixture sample was preferred to achieve a good quality concentrate with acceptable recovery. The influence of the particle-particle tribocharging effect between the pure coal and the pure silica was indirectly derived. It shows that with coal-silica contact, the coal charge distribution shrunk while the silica charge distribution extended. As a result, the RTS is not a perfect alternative to obtain a high purity concentrate, but it can be a highly efficient tool for the silica-rich coal gangue rejection.

In the pure coal RTS separation test, the low-density coal with 5.5±0.1% ash content was used as a raw material to produce low ash coal (ash content $\leq$ 4%). The *MD* value was used as the standard to judge the RTS separation efficiency. A higher *MD* value indicates a better RTS separation efficiency. The five factors screening test shows that the feed rate, charger rotation speed, and co-flow rate were the three relative significant factors in influencing the RTS separation efficiency. Then the Box-Behnken experiment design method was used based on the comparatively significant factors to investigate their individual and interactive effects, hence seeking the optimum operating conditions. The feed rate was found to be the most significant individual factor, and the feed rate-co-flow rate was the most significant interactive effect in impacting the *MD* value. Incorporating the previously discovered relations into the statistical analysis of the interactive effect, the high feed rate was proved to deteriorate particle tribocharging efficiency. Then the optimum operating conditions were locked according to the two sets of experiments. The best concentrate produced has an ash content of 3.85±0.08% with recovery of 62.97±1.11%. It shows that the coal RTS beneficiation can effectively produce the low ash coal with good recovery.

8. Recommendation for Future Work

In the present study, the particle tribocharging dynamics and the particle surface charge modeling have been investigated to deepen the understanding of fundamentals involved in tribocharging. The applications of the tribocharging in the research case study proved the potential application of RTS in upgrading coal. Some further studies are recommended to progress the triboelectrostatic separation technology.

(1) The quantification of charge injection into conductor bulk could be further studied and quantified using the oscilloscope or other similar more sensitive apparatus. The resistance of the conductor on the free movement of electrons inside a bulk needs to be measured to solve this problem. This study could further disclose material physically electronic properties.
(2) The developed tribocharging model that fits other material pairs needs to be examined to verify the robustness of this model, as well as the mathematical analysis procedure. More case studies about the contact charge of other material pairs could help pursuing the common law underlying it, which will be of great value for particle surface charge prediction and control.
(3) The particle separation control needs to be improved to better fit the separation of more minerals and wider size ranges. It can be realized by restricting the environmental hydrodynamics inside a separation chamber. The air flow conditions need to be more accurately adjusted based on the particle charge conditions for an optimum separation.
(4) More minerals with different size fractions are suggested to be tested using the RTS. The RTS beneficiation efficiency of those mineral samples could specify which minerals with what size fractions are most favorable for applying the RTS beneficiation. A successful bench test will be the key for the commercialization of the rotary triboelectrostatic separator.

References

Ali, F., Sharmene, M., Adnan Ali, R. Ayesha Ali. And Ion I. Inculet., 1998. Minority charge separation in falling particles with bipolar charge. *Journal of Electrostatics*, 45(2), pp. 139-155.

ASTM D 3174-12, 1989. Standard test method for ash in the analysis sample of coal and coke from coal, 05, 302.

Bada, S., Gcanga, S., Falcon, L., Falcon, R. and Makhula, M., 2013. Electrostatic concentration of phosphate flotation concentrate. *International Journal of Mineral Science and Technology*, 23(3), pp. 403-406.

Bada, S.O., Tao, D., Honaker, R.Q., Falcon, L.M. and Falcon, R.M.S., 2010. A study of rotary tribo-electrostatic separation of South African fine coal. *International Journal of Coal Preparation and Utilization*, 30(2-5), pp. 157-172.

Bardeen, J., 1947. Surface states and rectification at a metal semi-conductor contact. *Physical Review*, 71(10), p. 717.

Baytekin, H.T., Patashinski, A.Z., Branicki, M., Baytekin, B., Soh, S. and Grzybowski, B.A., 2011. The mosaic of surface charge in contact electrification. *Science*, 333 (6040), pp. 308-312.

Baytekin, H.T., Baytekin, B., Incorvati, J.T. and Grzybowski, B.A., 2012. Material transfer and polarity reversal in contact charging. *Angewandte Chemie*, 124(20), pp. 4927-4931.

Brennan, W.J., Lowell, J., O'Neill, M.C. and Wilson, M.P.W., 1992. Contact electrification: the charge penetration depth. *Journal of Physics D: Applied Physics*, 25(10), pp. 1513.

Buda, G., Bilici, M., Dascalescu, L. and Samuila, A., 2013. Influence of material moisture on the tribocharging process of plastic granules. *Particulate Science and Technology*, 31(2), pp. 162-167.

Bunchatheeravate, P., Curtis, J., Fujii, Y. and Matsusaka, S., 2013. Prediction of particle charging in a dilute pneumatic conveying system. *AlChE Journal*, 59(7), pp. 2308-2316.

Bunker, M.J., Davies, M.C., James, M.B. and Roberts, C.J., 2007. Direct observation of single particle electrostatic charging by atomic force microscopy. *Pharmaceutical Research*, 24(6), pp. 1165-1169.

Burgo, T.A., Silva, C.A., Balestrin, L.B. and Galembeck, F., 2013. Friction coefficient dependence on electrostatic tribocharging. *Scientific Report*, 3, pp. 1-8.

Calin, L., Caliap, L., Neamtu, V., Morar, R., Iuga, A., Samuila, A. and Dascalescu, L., 2008. Tribocharging of granular plastic mixtures in view of electrostatic separation. *IEEE Transactions on Industry Applications*, 44(4), pp. 1045-1051.

Cangialosi, F., Liberti, L., Notarnicola, M. and Stencel, J., 2006. Monte Carlo simulation of pneumatic tribocharging in two-phase flow for high-inertia particles. *Powder Technology*, 165(1), pp. 39-51.

Chang, Y.P., Chu, H.M. and Chou, H.M., 2007. Effects of mechanical properties on the tribo-electrification mechanisms of iron rubbing with carbon steel. *Wear*, 262(1), pp. 112-120.

Cheng, Y.C., 1973. Effect of charge inhomogeneities on silicon surface mobility. *Journal of Applied Physics*, 44(5), pp. 2425-2427.

Choi, K., Taghavivand, M. and Zhang, L., 2017. Experimental studies on the effect of moisture content and volume resistivity on electrostatic behavior of pharmaceutical powders. *International Journal of Pharmaceutics*.

Chowdry, A. and Westgate, C.R., 1974. The role of bulk traps in metal-insulator contact charging. *Journal of Physics D: Applied Physics*, 7(5), p. 713.

Ciccu, R., Ghiani, M. and Ferrara, G., 1993. Selective tribocharging of particles for separation. *KONA Powder and Particle Journal*, 11(0), pp. 5-16.

Coste, J. and Pechery, P., 1981. Influence of surface profile in polymer-metal contact charging. *Journal of Electrostatics*, 10, pp. 129-136.

Cui, L., An, L. and Jiang, H., 2008. A novel process for preparation of an ultra-clean superfine coal-oil slurry. *Fuel*, 87, pp. 2296-2303.

Cunningham, R.G. and Hood, H.P., 1970. The relation between contact charging and surface potential differences. *Journal of Colloid and Interface Science*, 32(3), pp. 373-376.

Das-Gupta, D.K., 1988. Surface charge decay on insulating films. In Electrical Insulation. *Conference Record of the 1988 IEEE International Symposium on* (pp. 296-299). IEEE.

Davies, D.K., 1969. Charge generation of dielectric surfaces. *Journal of Physics D: Applied Physics*, 2(11), p. 1533.

Derbyshire, F., 1989. Role of catalysis in coal liquefaction research and development. *Energy & Fuels*, 3, pp. 273-277.

Diaz, A.F. and Fenzel-Alexander, D., 1993. An ion transfer model for contct charging. *Langmuir*, 9(4), pp. 1009-1015.

Domansky, K., Leng, Y., Williams, C.C., Janata, J. and Petelenz, D., 1993. Mapping of mobile charges on insulator surfaces with the electrostatic force microscope. *Applied Physics Letters*, 63(11), pp. 1513-1515.

Dragan, C., Fati, O., Radu, M., Calin, L., Samuila, A. and Dascalescu, L., 2011. Tribocharging of mixed granular plastics in a fluidized-bed device. *IEEE Transactions on Industry Applications*, 47(4), pp. 1922-1928.

Duke, C.B. and Fabish, T.J., 1976. Charge-induced relaxation in polymers. *Physical Review Letters*, 37(16), p. 1075.

Dwari, R.K. and Rao, K.H., 2006. Tribo-electrostatic behavior of high ash non-coking Indian thermal coal. *International Journal of Mineral Processing*, 81(2), pp. 93-104.

Dwari, R.K. and Rao, K.H., 2007. Dry beneficiation of coal – a review. *Mineral Processing and Extractive Metallurgy Review*, 28(3), pp. 177-234.

Dwari, R.K. and Rao K.H., 2008. Non-coking coal preparation by novel tribo-electrostatic method. *Fuel*, 87, pp. 3562-3571.

Eilbeck, J., Rowley, G., Carter, P.A. and Fletcher, E.J., 2000. Effect of contamination of pharmaceutical equipment on powder triboelectrification. *International Journal of Pharmaceutics*, 195(1), pp. 7-11.

Emami Taba, L., Irfan, M.F., Wan Daud, W.A.M. and Chakrabarti, M.H., 2012. The effect of temperature on various parameters in coal, biomass and CO-gasification: A review. *Renewable and Sustainable Energy Reviews*,16, pp. 5584-5596.

Fabish, T.J., Saltsburg, H.M. and Hair, M.L., 1976. Charge transfer in metal/atactic polystyrene contacts. *Journal of Applied Physics*, 47(3), pp. 930-939.

Fabish, T.J. and Duke, C.B., 1977. Molecular charge states and contact charge exchange in polymers. *Journal of Applied Physics*, 48(10), pp. 4256-4266.

Fishchuk, I.I., Kadashchuk, A.K., Genoe, J., Ulah, M., Sitter, H., Singh, T.B., Sariciftci, N.S. and Bassler, H., 2010. Temperature dependence of the charge carrier mobility in disordered organic semiconductors at large carrier concentrations. *Physical Review B*, 81(4), p. 045202.

Forward, K.M., Lacks, D.J. and Sankaran, R.M., 2009. Particle-size dependent bipolar charging of Martian regolith simulant. *Geophysical Research Letters*, 36(130).

Homewood, K.P., 1984. An experimental investigation of the depth of penetration of charge into insulators contacted by a metal. *Journal of Physics D: Applied Physics*, 17(6), p. 1255.

Horn, R.G. and Smith, D.T., 1992. Contact electrification and adhesion between dissimilar materials. *Science*, 256(5055), p. 362.

Hu, W., Xie, L. and Zheng, X., 2012. Contact charging of silica glass particles in a single collision. *Applied Physics Letters*, 101(11), p. 114107.

Inculet, I.I., Castle, G.S.P. and Brown, J.D., 1998. Electrostatic separation of plastic for recycling. *Particulate Science and Technology*, 16(1), pp. 91-100.

Iuga, A., Morar, R., Samuila, A. and Dascalescu, L., 2001. Electrostatic separation of metals and plastics from granular industrial wastes. *IEE Proceedings-Science, Measurement and Technology*, 148(2), pp. 47-54.

Iuga, A., Cuglesan, I., Samuila, A., Blajan, M., Vadan, D. and Dascalescu, L., 2004. Electrostatic separation of muscovite mica from feldspathic pegmatites. *IEEE Transactions on Industry Applications*, 40(2), pp. 422-429.

Ireland, P.M., 2007. The role of charging contact in sliding triboelectrification. *Journal of Physics D: Applied Physics*, 41(2), p. 025305.

Ireland, P.M., 2010. Triboelectrification of particulate flows on surfaces: Part I – Experiments. *Powder Technology*, 198(2), pp. 189-198.

Ireland, P.M., 2010. Triboelectrification of particulate flows on surfaces: Part II – Mechanisms and models. *Powder Technology*, 198(2), pp. 199-210.

Ireland, P.M., 2012. Dymanic particle-surface tribocharging: The role of shape and contact mode. *Journal of Electrostatics*, 70(6), pp. 524-531.

Irfan, M.F., Usman, M.R. and Kusakabe, K., 2011. Coal gasification in CO₂ atmosphere and its kinetics since 1948: A brief review. *Energy*, 36, pp. 12-40.

Ishigaki, H., Kawaguchi, I. and Mizuta, S., 1979. A simple estimation of the elastic-plastic deformation of contacting asperities. Wear, 54(1), pp. 157-164.

Jing, Q., Zhu, G., Bai, P., Xie, Y., Chen, J., Han, R.P. and Wang, Z.L., 2014. Case-encapsulated triboelectric nanogenerator for harvesting energy from reciprocating sliding motion. *Acs Nano*, 8(4), pp. 3836-3842.

Kepler, R., 1960. Charge carrier production and mobility in anthracene crystals. *Physical Review*, 119(4), p. 1226.

Kiely, J.D. and Hsia, Y.T., 2002. Tribocharging of the magnetic hard disk drive head-disk interface. *Journal of Applied Physics*, 91(7), pp. 4631-4636.

Kopyscinski, J., Schidhauer, T.J. and Biollaz, S., 2010. Production of synthetic natural gas (SNG) from coal and dry biomass - A technology review from 1950-2009, *Fuel*, 89, pp. 1763-1783.

Korevaar, M.W., Padding, J.T., Van der Hoef, M.A. and Kuipers, J.A.M., 2013. Modeling of tribo-electrification of a pneumatically conveyed powder in a squared duct using DEM-CFD. *In Proc. ESA Annual Meeting on Electrostatics (p.2)*.

Kumar Majumder, S., Chandna, K., Sankar De, D. and Kundu, G., 2006. Studies on flow characteristics of coal-oil-water slurry system. *International Journal of Mineral Processing*, 79, pp. 217-224.

Kusano, Y., Singh, S.V. and Michelsen, P., 2009, January. Plasma generation induced by triboelectrification. *In XXX International Conference on Phenomena in Ionized Gases*.

Kwetkus, B.A., 1998. Particle electrification of coal and minerals. *Journal of Electrostatics*, 32, pp. 271-276.

Lacks, d.J. and Sankaran, R.M., 2011. Contact electrification of insulating materials. *Journal of Physics D: Applied Physics*, 44(45), p. 453001.

Law, K.Y., Tarnawskyj, I.W., Salamida, D. and Debies, T., 1995. Investigation of the contact charging mechanism between an organic salt doped polymer surface and polymer-coated metal beads. *Chemistry of Materials*, 7(11), pp. 2090-2095.

Law, K.Y., Tarnawskyj, I.W. and Salamida, D., 1998. Investigation of the mechanism of humidity effect on toner charging: A morel toner study. *Journal of Imaging Science and Technology*, 42(6), pp. 584-587.

Li, B. Tao, D. Ou, Z. and Liu, J., 2003. Cyclo-microbubble column flotation of fine coal, *Separation Science and Technology*, 38, pp. 1125-1140.

Lungu, M., 2004. Electrical separation of plastic materials using the triboelectric effect. *Minerals Engineering*, 17(1), pp. 69-75.

Lowell, J., 1976. The electrification of polymers by metals. *Journal of Physics D: Applied Physics*, 9(11), p. 1571.

Lowell, J. and Truscott, W.S., 1986. Triboelectrification of identical insulators. II. Theory and further experiments. *Journal of Physics D: Applied Physics*, 19(7), p. 1281.

Ma, S., Zhao, P., Guo, Y., Zhong, L. and Wang, Y., 2013. Synthesis, characterization and application of polycarboxylate additive for coal water slurry. *Fuel*, 111, pp. 648-652.

Masuda, H. and Iinoya, K., 1978. Electrification of particles by impact on inclined metal plates. *AlChE Journal*, 24(6), pp. 950-6.

Masuda, S., Toraguchi, M., Takahashi, T. and Haga, K., 1983. Electrostatic beneficiation of coal using a cyclone-tribocharger. *IEEE Transactions on Industry Applications*, (5), pp. 789-793.

Masuda, H., Yasuda, D., Ema, A. and Tanoue, K.I., 2004. Effects of oxidization and adsorbed moisture on time charge in Tribo-electrification of powder particles [Translated]. *KONA Powder and Particle Journal*, 22, pp. 168-176.

Matsusaka, S. and Masuda, H., 2003. Electrostatics of particles. *Advanced Powder Technology*, 14(2), pp. 143-166.

Matsusaka, S., Maruyama, H., Matsuyama, T. and Ghadiri, M., 2010. Triboelectric charging of powders: A review. *Chemical Engineering Science*, 65(22), pp. 5781-5807.

Matsusaka, S., 2011. Control of particle tribocharging. *KONA Powder and Particle Journal*, 29, pp. 27-38.

Matsuyama, T. and Yamamoto, H., 1995. Charge relaxation process dominates contact charging of a particle in atmospheric conditions. *Journal of Physics D: Applied Physics*, 28(12), p. 2418.

Matsuyama, T. and Yamamoto, H., 1997. Charge-relaxation process dominates contact charging of a particle in atmospheric condition: II. The general model. *Journal of Physics D: Applied Physics*, 30(15), p. 2170.

Matsusyama, T. and Yamamoto, H., 2006. Impact charging of particulate materials. *Chemical Engineering Science*, 61(7), pp. 2230-2238.

Mazumder, M.K., Banerjee, S., Ware, R.E., Mu, C., Kaya, N. and Huang, C.C., 1994. Characterization of tribocharging properties of powder paint. *IEEE Transactions on Industry Applications*, 30(2), pp. 365-369.

Mead, C.A., Snow, E.H. and Deal, B.E., 1966. Barrier lowering and field penetration at metal-dielectric interfaces. *Applied Physics Letters*, 9(1), pp. 53-55.

McCarty, L.S., Winkleman, A. and Whitesides, G.M., 2007. Ionic electrets: electrostatic charging of surfaces by transferring mobile ions upon contact. *Journal of the American Chemical Society*, 129(13), pp. 4057-4088.

McCarty, L.S. and Whitesides, G.M., 2008. Electrostatic charging due to separation of ions at interfaces: contact electrification of ionic electrets. *Angewandte Chemie International Edition*, 47(12), pp. 2188-2207.

Michaelson, H.B., 1977. The work function of the elements and its periodicity. *Journal of Applied Physics*, 48(11), pp. 4729-2733.(6), pp. 631-637.

Miloudi, M., Medles, K., Tilmatine, a., Brahami, M. and Dascalescu, L., 2011. Modeling and optimization of a propeller-type tribocharger for granular materials. *Journal of Electrostatics*, 69.

Miloudi, M., Medles, K., Tilmatine, A., Bendaoud, A. and Dascalescu, L., 2013. Optimization of belt-type electrostatic separation of tribo-aerodynamically charged granular plastic mixtures. *IEEE Transactions on Industry Applications*, 49(4), pp. 1781-1786.

Mishra, S.K. and Kanungo, S.B., 2000. Factor affecting the preparation of highly concentrated coal-water slurry (Hccws). *Journal of Scientific and Industrial Research*, 59, pp. 765-790.

Miyazaki, T., Shoji, Y., Kamei, Y. and Iba, T., 1982. Utilization of COM (coal oil mixture) for injection to blast furnaces. *Transactions of the Iron and Steel Institute of Japan*, 22, pp. 207-213.

Mizes, H.A., Conwell, E.M. and Salamida, D.P., 1990. Direct observation of ion transfer in contact charging between a metal and a polymer. *Applied Physics Letters*, 56(16), pp. 1597-1599.

Mukherjee, R., Gupta, V., Naik, S., Sarkar, S., Sharma, V., Peri, P. and Chaudhuri, B., 2016. Effects of particle size on the triboelectrification phenomenon in pharmaceutical excipients: Experiments and multi-scale modeling. *Asian Journal of Pharmaceutical Sciences*, 11(5), pp. 603-617.

Mochida, I., Okuma, O. and Yoon, S.H., 2013. Chemicals from direct coal liquefaction, *Chemical Reviews*, 114, pp. 1637-1672.

Mozer, A.J. and Sariciftci, N.S., 2004. Negative electric field dependence of charge carrier drift mobility in conjugated, semiconducting polymers. *Chemical Physics Letters*, 389(4), pp. 438-442.

Nakayama, K., 1996. Triboelectrification and friction in insulators in ambient air. *Wear*, 194, pp. 185-189.

Newaz, A.K.M., Puzyrev, Y.S., Wang, B., Pantelides, s.T. and Bolotin, K.I., 2012. Probing charge scattering mechanisms in suspended graphene by varying its dielectric environment. *arXiv preprint arXiv*: 1203.1547.

Nicolai, H.T., Mandoc, M.M. and Blom, P.W.M., 2011. Electron traps in semiconducting polymers: exponential versus Gaussian trap distribution. *Physical Review B*, 83 (19), p. 195204.

Ning, L., Jian, L., Yang, S., Wang, J., Ren, J. and Wang, J., 2010. Effect of carbon black on triboelectrification electrostatic potential of MC nylon composites. *Tribology International*, 43(3), pp. 568-576.

Novoselov, K.S., Geim, A.K., Morozov, S.V., Jiang, D., Zhang, Y., Dubonos, S.V., Grigorieva, I.V. and Firsov, A.A., 2003. Electric field effect in atomically thin carbon films. *Science*, 306(5696), pp. 666-669.

Park, H.S., Hwang, J. and Choa, S.H., 2004. Tribocharge build-up and decay at a slider-disk interface. *Microsystem Technologies*, 10(2), pp. 109-114.

Park, C.H., Park, J.K., Jeon, H.S. and Chun, B.C., 2008. Triboelectric series and charging properties of plastics using the designed vertical-reciprocation charger. *Journal of Electrostatics*, 66(11), pp. 578-583.

Pei, C., Wu, C.Y., England, D., Byard, S., Berchtold, H. and Adams, M., 2013. Numerical analysis of contact electrification using DEM-CFD. *Powder Technology*, 248, pp. 34-43.

Pei, C., Wu, C.Y., Adams, M., England, D., Byard, S. and Berchtold, H., 2015. Contact electrification and charge distribution on elongated particles in a vibrating container. *Chemical Engineering Science*, 125, pp. 238-247.

Pence, S., Novotny, V.J. and Diaz, A.F., 1994. Effect of surface moisture on contact charge of polymers containing ions. *Langmuir*, 10(2), pp. 592-596.

Peterson, J.W., 1954. Contact charging between nonconductors and metal. *Journal of Applied Physics*, 25(7), pp. 907-915.

Pham, R., Virnelson, R.C., Sankaran, R.M. and Lacks, D.J., 2011. Contact charging between surfaces of identical insulating materials in asymmetric geometries. *Journal of Electrostatics*, 69(5), pp. 456-460.

Podzorov, V., Menard, E., Borissov, A., Kiryukhin, V., Rogers, J.A. and Gershenson, M.E., 2004. Intrinsic charge transport on the surface of organic semiconductors. *Physical Review Letters*, 93(8), p. 086602.

Poppe, T. and Schrapler, R., 2005. Further experiments on collisional tribocharging of cosmic grains. *Astronomy & Astrophysics*, 438(1), pp. 1-9.

Reishl, G.P., Makela, J.M., Karch, R. and Necid, J., 1996. Bipolar charging of ultrafine particles in the size range below 10 nm. Journal of Aerosol Science, 27(6), pp. 931-949.

Rowley, G. and Mackin, L.A., 2003. The effect of moisture sorption on electrostatic charging of selected pharmaceutical excipient powders. *Powder Technology*, 135, pp. 50-58.

Saeki, M., 2006. Vibratory separation of plastic mixtures using triboelectric charging. *Particulate Science and Technology*, 24, pp. 153-164.

Saunders, V.R., Freyria-Fava, C., Dovesi, R., Salasco, L. and Roetti, C., 1992. On the electrostatic potential in crystalline systems where the charge density is expanded in Gaussian functions. *Molecular Physics*, 77(4), pp. 629-665.

Schella, A., Herminghaus, S. and Schroter, M., 2017. Influence of humidity on tribo-electric charging and segregation in shaken granular media. *Soft Matter*, 13(2), pp. 394-401.

Shaw, P.E., 1917. Experiments on tribo-electricity. I. The tribo-electric series. Proceedings of the Royal Society of London. *Series A, Containing Papers of a Mathematical and Physical Character*, 94(656), pp. 16-33.

Shinbrot, T., Komatsu, T.A. and Zhao, Q., 2008. *Spontaneous tribocharging of similar materials. EPL (Europhysics Letters)*, 83(2), p. 24004.

Shinjo, Y., Nishizawa, H., Tsunemi, K., Saitoh, M. and Hosoya, M., 1999. Effect of additive induced discharge on tribocharging process between toner and carrier. *Journal of Imaging Science and Technology*, 43(5), pp. 467-471.

Singh, S.V., Kusano, Y., Morgen, P. and Michelsen, P.K., 2012. Surface charging, discharging and chemical modification at a sliding contact. *Journal of Applied Physics*, 111(8), p. 083501.

Sobhy, A. and Tao, D., 2014. Innovative RTS technology for dry beneficiation of phosphate. Procedia Engineering, 83, pp. 111-121. Tao, D., Fan, M.M. and Jiang, X.K., 2009. Dry coal fly ash cleaning using rotary triboelectrostatic separator. *Mining Science and Technology (China)*, 19(5), pp. 642-647.

Soh, S., Liu, H., Cademartiri, R., Yoon, H.J. and Whitesides, G.M., 2014. Charging of multiple interacting particles by contact electrification. *Journal of the American Chemical Society*, 136(38), pp.13348-13354.

Soon, S. and Valdivieso, A.L., 1998. Hydrophobic flocculation flotation for beneficiating fine coal and minerals, *Separation Science and Technology*, 33, pp. 1195-1212.

Soong, Y., Schoffstall, M.R. and Link, T.A., 2001. Triboelectrostatic beneficiation of fly ash. *Fuel*, 80(6), pp.879-884.

Steel, K.M. and Patrick, J.W., 2001. The production of ultra clean coal by chemical demineralization, *Fuel*, 80, pp. 2019-2023.

Sternovsky, Z., Robertson, S., Sickafoose, A., Colwell, J. and Horanyi, M., 2002. Contact charging of lunar and Martian dust simulants. *Journal of Geophysical Research: Planets*, 107(E11).

Tanoue, K.I., Tanaka, H., Kitano, H. and Masuda, H., 2001. Numerical simulation of tribo-electrification of particles in a gas-solids two-phase flow. *Powder Technology*, 118(1), pp. 121-129.

Tao, D. Luttrell, G.H. and Yoon, R.H., 2000. A parametric study of froth stability and its effect on column flotation of fine particles, *International Journal of Mineral Processing*, 59, pp. 25-43.

Tao, D., Sobhy, A., Li, Q., Honaker, R. and Zhao, Y., 2011. Dry cleaning of pulverized coal using a novel rotary triboelectrostatic separator (RTS). *International Journal of Coal Preparation and Utilization*, 31(3-4), pp. 187-202.

Terris, B.D., Stern, J.E., Rugar, D. and Mamin,H.J., 1989. Contact electrification using force microscopy. *Physical Review Letters*, 63 (24), p. 2669.

Thomas, A., Saleh, K., Guigon, P. and Czechowski, C., 2008. Tribocharging behavior of automotive powder coatings. In Journal of Physics: *Conference Series* (Vol. 142, No. 1, p. 012031). IOP Publishing.

Thornton, C., 1997. Coefficient of restitution for collinear collisions of elastic-perfectly plastic spheres. *Journal of Applied Mechanics*, 64(2), pp. 383-386.

Tilmatine, A., Medles, K., Bendimerad, S.E., Boukholda, F. and Dascalescu, L., 2009. Electrostatic separators of particles: Application to plastic/metal, metal/metal and plastic/plastic mixtures. *Waste Management*, 29(1), pp. 228-232.

Tinsley, B.A., Rohrbaugh, R.P., Hei, M. and Beard, K.V., 2000. Effects of image charges on the scavenging of aerosol particles by cloud droplets and on droplet charging and possible ice nucleation processes. *Journal of the Atmospheric Sciences*, 57(13), pp. 2118-2134.

Tokeshi, T., Hiratsuka, K.I., Sasaki, A., Uchiyama, S. and Kajdas, C., 2009. Triboelectrification in sliding/rolling contacts using twin-ring tribometer. *Tribology Transactions*, 52(6), pp. 759-767.

Trigwell, S., Mazumder, M.K. and Pellissier, R., 2001. Tribocharging in electrostatic beneficiation of coal: Effects of surface composition on work function as measured by x-ray photoelectron spectroscopy and ultraviolet photoelectron spectroscopy in air. *Journal of Vacuum Science & Technology A: Vacuum, Surfaces, and Films*, 19(4), pp. 1454-1459.

Trigwell, S., Grable, N., Yurteri, C.U., Sharma, R. and Mazumder, M.K., 2003. Effects of surface properties on the tribocharging characteristics of polymer powder as applied to industrial processes. *IEEE Transactions on Industry Applications*, 39(1), pp. 79-86.

Trigwell, S., Captain, J.G., Arens, E.E., Quinn, J.W. and Calle, C.I., 2009. The use of tribocharging in the electrostatic beneficiation of lunar simulant. *IEEE Transaction on Industry Applications*, 45(3), pp. 1060-1067.

Vasireddy, S., Morreal, B., Cugini, A., Song, C. and Spivey, J.J., 2011. Clean liquid fuels from direct coal liquefaction: chemistry, catalysis, technological status and challenges. *Energy & Environmental Science*, 4, pp. 311-345.

Wahlin, A. and Backstrom, G., 1974. Sliding electrification of Teflon by metals. *Journal of Applied Physics*, 45(5), pp. 2058-2064.

Wang, S., Lin, L., Xie, Y., Jing, Q., Niu, S. and Wang, Z.L., 2013. Sliding triboelectric nanogenerators based on in-plane charge-separation mechanism. *Nano Letters*, 13(5), pp. 2226-2233.

Watanabe, H., Ghadiri, M., Matsuyama, T., Ding, Y.L., Pitt, K.G., Maruyama, H., Matsusaka, S. and Masuda, H., 2007. Triboelectrification of pharmaceutical powders by particle impact. *International Journal of Pharmaceutics*, 334(1), pp. 149-155.

Wijaya, N., Choo, T.K. and Zhang, L., 2011. Generation of ultra-clean coal from Victorian brown coal – Sequential and single leaching at room temperature to elucidate the elution of individual inorganic elements, *Fuel Processing Technology*, 92, pp. 2127-2137.

Wiles, J.A., Fialkowski, M., Radowski, M.R., Whitesides, G.M. and Grzybowski, B.A., 2004. Effects of surface modification and moisture on the rates of charge transfer between metals and organic materials. *The Journal of Physical Chemistry B*, 108(52), pp. 20296-20302.

Wintle, H.J., 1972. Surface-charge decay in insulators with nonconstant mobility and with deep trapping. *Journal of Applied Physics*, 43(7), pp. 2927-2930.

Wu, J., Li, J. and Xu, Z., 2008. Electrostatic separation for multi-size granule of crushed printed circuit board waste using two-toll separator. *Journal of Hazardous Materials*, 159(2), pp. 230-234.

Wu. G., Li, J. and Xu, Z., 2013. Triboelectrostatic separation for granular plastic waste recycling: A review. *Waste Management*, 33(3), pp. 585-597.

Xie, L., Li, G., Bao, N. and Zhou, J., 2013. Contact electrification by collision of homogeneous particles. *Journal of Applied Physics*, 113(18), p. 184908.

Yang, X., Wang, L., Wang, C., Long, W. and Shuai, Z., 2008. Influences of crystal structures and molecular sizes on the charge mobility of organic semiconductors: oligothiophenes. *Chemistry of Materials*, 20(9), pp. 3205-3211.

Zelmat, M.E.M., Tilmatine, A., Rizouga, M., Gouri, R., Medles, K. and Dascalescu, L., 2013. Experimental analysis of a cyclone tribocharging device for free-fall triboelectric separation of plastic particles. *IEEE Transactions on Dielectrics and Electrical Insulation*, 20(5), pp. 1584-1589.

Zhang, W., Honaker, R., Li, Y. and Chen, J., 2014. The importance of mechanical scrubbing in magnetite-concentrate reverse-flotation. *Minerals Engineering*, 69, pp. 133-136.

Zhang, W. and Honaker, R., 2015. Studies on carbon flotation from fly ash. *Fuel Processing Technology*, 139, pp. 236-241.

Zhang, W., Honaker, R. and Groppo, J., 2016. Fundamental study of the monazite-calcite flotation separation. In *XXVIII International Mineral Processing Congress, Sep. 11-15, Quebec, Canada*.

Zhang, W., Honaker, R. and Groppo, J., 2017. Concentration of rare earth minerals from coal by froth flotation. *Minerals & Metallurgical Processing*, 34(3).

Zhao, H., Castle, G.S.P. Inculet, I.I. and Bailey, A.G., 2000. Bipolar charging in polydisperse polymer powders in industrial processes. In Industry Applications Conference, 2000. *Conference Record of the 2000 IEEE* (Vol. 2, pp. 835-841). IEEE.

Zhao, H., Castle, G.P., Inculet, I.I. and Bailey, A.G., 2003. Bipolar charging of poly-disperse polymer powders in fluidized beds. *IEEE Transactions on Industry Applications*, 39(3), pp. 612-618.

Zhao, T. and Comber, M.G., 2000. Calculation of electric field and potential distribution along nonceramic insulators considering the effects of conductors and transmissions towers. *IEEE Transactions on Power Delivery*, 15(1), pp. 313-318.

Zhou, Y.S., Liu, Y., Zhu, G., Lin, Z.H., Pan, C., Jing, Q. and Wang, Z.L., 2013. In situ quantitative study of nanoscale triboelectrification and patterning. *Nano Letters*, 13(6), pp. 2771-2776.

Zhu, W., Perebeinos, V., Freitag, M. and Avouris, P., 2009. Carrier scattering, mobilities, and electrostatic potential in monolayer, bilayer, and trilayer graphene, *Physical Review B*, 80(23), p. 235402.

VITA

Education

09/07-07/11 **B.Sc.** (Mineral Processing Engineering), China University of Mining and Technology (Beijing).

09/11-08/13 **M.Sc.** (Mining Engineering), West Virginia University.

Professional Licensure

10/2016 Professional Engineer (**PE**), Exam Pass

Selected Research Experience

10/11-05/13 **Column flotation using pico-nano bubbles to beneficiate low rank coal.** The ultra-small size air bubble impacting the column flotation performance was studied. Pico-nano bubbles produced by a static mixer-venturi tube system could increase bubble-particle collision probability and selective attachment. Pico-nano bubbles attached on the coal surface could also act as a secondary collector that has a bridging effect, which enhances the coal hydrophobicity.

05/14-Present **Fundamental improvement in the tribocharging separation progress for upgrading coal.** Tribocharging is an ancient method to impose static charges on material surface through mechanical interaction. In this study, the material surface electronic property, and operating parameters in influencing particle tribocharging were studied. A semi-empirical model was established to predict particle surface charge. The tribocharging kinetic characteristics were investigated to better understand the tribocharging mechanism. The rotary triboelectrostatic separator (RTS) was used to upgrade coal. Particle size effect and operating parameters were studied to improve the RTS separation efficiency.

Internship and Working Experience

06/16-07/16 **Ibercoal, LDA, Sines, Portugal**. Perform the consulting job in solving the technical problems from the coal preparation plant. Test the plant operation performance through sample collection, lab experimental test and data analysis. Troubleshooting in some equipment, provide solutions to enhance the overall plant operation efficiency.

Publications

1. Chen, Jinxiang, and Rick Honaker. “Dry separation on coal-silica mixture using rotary triboelectrostatic separator.” Fuel Processing Technology 131 (2015): 317-324.
2. Zhang, Lei, Ricky Honaker, Wenli Liu, Dongpo Men and Jinxiang Chen. “Calculation of terminal velocity in transitional flow for spherical particle.” International Journal of Mining Science and Technology 25, no. 2 (2015): 311-317.
3. Zhang, Wencai, Rick Honaker, Yonggai Li, and Jinxiang Chen. “The importance of mechanical scrubbing in magnetite-concentrate reverse-flotation.” Minerals Engineering 69 (2014): 133-13.